THE UNIVERSITY OF
WARWICK

Library Declaration and Deposit Agreement

1. STUDENT DETAILS

Please complete the following:

Full name: Matthew Stuart Brewer

University ID number: 0621713

2. THESIS DEPOSIT

2.1 I understand that under my registration at the University, I am required to deposit my thesis with the University in BOTH hard copy and in digital format. The digital version should normally be saved as a single pdf file.

2.2 The hard copy will be housed in the University Library. The digital version will be deposited in the University's Institutional Repository (WRAP). Unless otherwise indicated (see 2.3 below) this will be made openly accessible on the Internet and will be supplied to the British Library to be made available online via its Electronic Theses Online Service (EThOS) service.
[At present, theses submitted for a Master's degree by Research (MA, MSc, LLM, MS or MMedSci) are not being deposited in WRAP and not being made available via EthOS. This may change in future.]

2.3 In exceptional circumstances, the Chair of the Board of Graduate Studies may grant permission for an embargo to be placed on public access to the hard copy thesis for a limited period. It is also possible to apply separately for an embargo on the digital version. (Further information is available in the *Guide to Examinations for Higher Degrees by Research*.)

2.4 *If you are depositing a thesis for a Master's degree by Research, please complete section (a) below. For all other research degrees, please complete both sections (a) and (b) below:*

(a) Hard Copy

I hereby deposit a hard copy of my thesis in the University Library to be made publicly available to readers ~~(please delete as appropriate) EITHER~~ immediately ~~OR after an embargo period of~~ ..... ~~months/years as agreed by the Chair of the Board of Graduate Studies~~.

I agree that my thesis may be photocopied. YES / ~~NO (Please delete as appropriate)~~

(b) Digital Copy

I hereby deposit a digital copy of my thesis to be held in WRAP and made available via EThOS.

Please choose one of the following options:

EITHER My thesis can be made publicly available online. YES / ~~NO (Please delete as appropriate)~~

~~OR My thesis can be made publicly available only after.....[date]~~ ~~(Please give date)~~
~~YES / NO (Please delete as appropriate)~~

~~OR My full thesis cannot be made publicly available online but I am submitting a separately identified additional, abridged version that can be made available online.~~
~~YES / NO (Please delete as appropriate)~~

~~OR My thesis cannot be made publicly available online. YES / NO (Please delete as appropriate)~~

3. GRANTING OF NON-EXCLUSIVE RIGHTS

Whether I deposit my Work personally or through an assistant or other agent, I agree to the following:

Rights granted to the University of Warwick and the British Library and the user of the thesis through this agreement are non-exclusive. I retain all rights in the thesis in its present version or future versions. I agree that the institutional repository administrators and the British Library or their agents may, without changing content, digitise and migrate the thesis to any medium or format for the purpose of future preservation and accessibility.

4. DECLARATIONS

(a) I DECLARE THAT:

- I am the author and owner of the copyright in the thesis and/or I have the authority of the authors and owners of the copyright in the thesis to make this agreement. Reproduction of any part of this thesis for teaching or in academic or other forms of publication is subject to the normal limitations on the use of copyrighted materials and to the proper and full acknowledgement of its source.
- The digital version of the thesis I am supplying is the same version as the final, hard-bound copy submitted in completion of my degree, once any minor corrections have been completed.
- I have exercised reasonable care to ensure that the thesis is original, and does not to the best of my knowledge break any UK law or other Intellectual Property Right, or contain any confidential material.
- I understand that, through the medium of the Internet, files will be available to automated agents, and may be searched and copied by, for example, text mining and plagiarism detection software.

(b) IF I HAVE AGREED (in Section 2 above) TO MAKE MY THESIS PUBLICLY AVAILABLE DIGITALLY, I ALSO DECLARE THAT:

- I grant the University of Warwick and the British Library a licence to make available on the Internet the thesis in digitised format through the Institutional Repository and through the British Library via the EThOS service.
- If my thesis does include any substantial subsidiary material owned by third-party copyright holders, I have sought and obtained permission to include it in any version of my thesis available in digital format and that this permission encompasses the rights that I have granted to the University of Warwick and to the British Library.

5. LEGAL INFRINGEMENTS

I understand that neither the University of Warwick nor the British Library have any obligation to take legal action on behalf of myself, or other rights holders, in the event of infringement of intellectual property rights, breach of contract or of any other right, in the thesis.

Please sign this agreement and return it to the Graduate School Office when you submit your thesis.

Student's signature:  Date: 13/3/2014

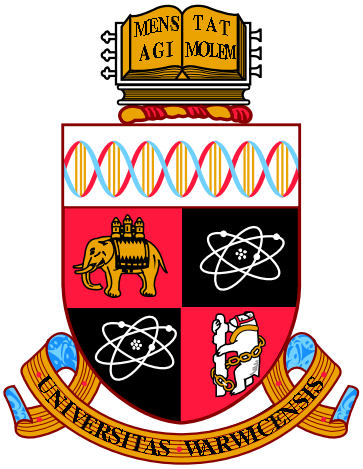

Magnetic Interactions in Systems with Reduced Dimensionality

by

Matthew Stuart Brewer

Thesis

Submitted to the University of Warwick

for the degree of

Doctor of Philosophy

Department of Physics

March 2014

THE UNIVERSITY OF WARWICK

Contents

List of Tables

List of Figures

Acknowledgments

I must first express my gratitude to my supervisor, Dr Thomas Hase. Not only for providing me with the excellent opportunity to continue my studies, but for providing me with help and support throughout the years we have worked together. I would also like to extend this gratitude to the wider physics department at the University of Warwick for providing a friendly and engaging work environment where I have spent many happy years. I would like to thank the members of the materials physics department at the University of Uppsala. In particular I would like to thank Martina Ahlberg, Dr Unnar Arnalds, Dr Matts Björck and Prof. Björgvin Hjörvarsson with whom I had the great pleasure of working closely.

This work would not have been possible without the help from the instrument scientists at the various facilities visited throughout the course of my doctoral studies. This includes, but is not limited to, Dr Laurence Bouchenoire and Dr Paul Thompson at XMaS, Dr Daniel Haskel, Dr Yongseong Choi and Dr Jonathan Lang at 4-ID-D, Dr Cecilia Sánchez-Hanke at X13A and Dr Christy Kinane at CRISP. Their generosity with time, knowledge and expertise not only ensured the success of our many experiments, but was invaluable to my overall development and understanding of the field. I would also like to gratefully acknowledge the financial support of the EPSRC.

Finally, I would like to express my ultimate thanks to my family, and in particular my loving wife Emily, for their unending support and encouragement.

Declarations

This thesis is submitted to the University of Warwick in support of my application for the degree of Doctor of Philosophy. It has been composed by myself and has not been submitted in any previous application for any degree.

Unless otherwise stated, the responsibilities for the data presented are as follows:

The measurements in chapter 5 were performed at the X13A beamline at the NSLS by the author, Dr Thomas Hase and Dr Matts Björck. The temperature dependent reflectivity data in figures 5.4 and 5.6 were collected by Martina Ahlberg and collaborators at the University of Uppsala. All data analysis and fitting in this chapter was performed by the author under the supervision of Dr Thomas Hase. The measurements in chapter 6 were performed at the 4-ID-D beamline at the APS by the author, Dr Thomas Hase, Dr Laurence Bouchenoire and Dr Paul Thompson, and using the CRISP instrument at the ISIS facility by the author and Dr Thomas Hase. The Fe edge data in figure 6.18 were collected at U4B at the NSLS by Dr Thomas Hase. All data analysis and fitting in this chapter was performed by the author under the supervision of Dr Thomas Hase. The measurements in chapter 7 were conducted at the XMaS beamline at the ESRF and at the 4-ID-D beamline at the APS by the author, Dr Thomas Hase, Dr Laurence Bouchenoire and Dr Paul Thompson. The SEM images in figure 7.1 and 7.2 were provided by Dr Unnar Arnalds at the University of Uppsala. All data analysis and fitting in this chapter was performed by the author under the supervision of Dr Thomas Hase.

All samples used in this thesis were prepared by Martina Ahlberg, Dr Unnar Arnalds and colleagues at the University of Uppsala.

Publications

Publications based on work presented in this thesis:

The effect of proximity on the magnetic ordering in itinerant Pd/Fe/Pd heterostructures

Thomas P. A. Hase, Matthew S. Brewer, Unnar B. Arnalds, Martina Ahlberg, Vassilios Kapaklis, Matts Björck, Laurence Bouchenoire, Paul Thompson, Daniel Haskel, Yongseong Choi, Jonathan Lang, Cecilia Sánchez-Hanke, and Björgvin Hjörvarsson
Submitted to: Physical Review X

Element resolved magnetization profiles in Pd/Fe/Pd trilayer

M.S. Brewer, U.B. Arnalds, E. Holmström, M. Björck, G. Andersson, M. Ahlberg, V. Kapaklis, L. Bouchenoire, P.B.J. Thompson, D. Haskel, J. Lang, C. Sánchez-Hanke, C.J. Kinane, B. Hjörvarsson and T. P. A. Hase
In Prep for: Journal of Physics: Condensed Matter (Letters)

Reflectivity Studies of Magnetic Heterostructures

Matts Björck, Matthew S. Brewer, Unnar B. Arnalds, Erik Östman, Martina Ahlberg, Vassilios Kapaklis, Evangelos Th. Papaioannou, Gabriella Andersson, Björgvin Hjörvarsson and Thomas P.A. Hase
Accepted in: Journal of Nano Research

Thermal transitions in nano-patterned XY-magnets

Unnar B. Arnalds, Martina Ahlberg, Matthew S. Brewer, Vassilios Kapaklis, Evangelos Th. Papaioannou, Masoud Karimipour, Panagiotis Korelis, Aaron Stein, Sveinn Ólafsson, Thomas P. A. Hase and Björgvin Hjörvarsson

Submitted to: Applied Physics Letters

Other Publications:

Growth and characterisation of NiSb(0001)/GaAs(111)B epitaxial films

James D. Aldous, Christopher W. Burrows, Ian Maskery, Matthew Brewer, David Pickup, Marc Walker, James Mudd, Thomas P. A. Hase, Jon A. Duffy, Stuart Wilkins, Cecilia Sánchez-Hanke and Gavin R. Bell

Journal of Crystal Growth, **357** *1-8* (2012)

DOI: 10.1016/j.jcrysgro.2012.07.010

Depth-dependent magnetism in epitaxial MnSb thin films: effects of surface passivation and cleaning

J.D. Aldous, C.W. Burrows, I. Maskery, M.S. Brewer, T.P.A. Hase, J.A. Duffy, M.R. Lees, C. Sánchez-Hanke, T. Decoster, W. Theis, A. Quesada, A.K. Schmid and G. R. Bell

Journal of Physics - Condensed Matter, **24** 14 *146002* (2012)

DOI: 10.1088/0953-8984/24/14/146002

Abstract

Detailed knowledge of the interaction of magnetic moments is key to developing the next generation of magnetic devices. Systems with induced moments provide an ideal regime in which to study this fundamental behaviour. Resonant x-ray scattering and polarised neutron reflectivity are complementarily used to map induced moment profiles in continuous FeZr/CoZr multilayer films and both continuous and patterned Pd/Fe/Pd trilayer films. Resonant scattering is additionally employed to measure the dimensionality of the magnetic lattice through observations of the magnetic ordering behaviour.

The shape and extent of the induced profiles was resolved with unprecedented accuracy, and was found to conform to the theoretical expectation: all profiles decayed exponentially from the inducing material, with an extent in the nm regime. Adjacent magnetic lattices were found to interact only through the magnitude of their moments, acting through the magnetic susceptibility of the induced material. The dimensionality of adjacent magnetic lattices were therefore found to be independent. Additionally, a significant, and unexpected, observation was made of the thinnest Fe layers studied: the Fe moment was seen to vanish though a pronounced induced moment remained in the neighbouring Pd. The definitive cause of this unusual behaviour has yet to be discovered. In the patterned materials, the interaction between adjacent islands was found to contribute minimally to the overall behaviour in the geometry studied. The energy cost of rotating the moments within an individual island was the dominating contribution to the magnetic ordering behavior.

These results provide new insight into the coupling mechanisms between adjacent moments, while revealing new complexities that provide the foundation for further study.

Chapter 1

Motivation

Technological advancements have historically often been linked with a novel exploitation of artificially created materials, or the modification of material properties to meet the requirements of a novel application. In its simplest and earliest form this might involve increasing the strength and durability of a material, for example adding carbon to iron to produce steel. Centuries later, the same process can now be seen in modern transistors where silicon is doped with, for example, phosphorous or boron to produce the requisite semiconducting properties.

For these advancements, both the understanding of material properties and manufacturing processes must be sufficiently developed. Manufacturing methods have, however, developed to the point of atomic scale precision [1]. The only real barriers remaining are the time and cost of production, and sufficient understanding of fundamental material properties. The latter drives a wealth of diverse research projects at institutions around the world [2–7]. This project concentrates on the magnetic properties of layered materials and the atomic scale magnetic interactions at the interfaces therein. Magnetism is a property which is commonly exploited in computing, most notably in magnetic hard disk drives [8].

Most data storage devices employ locally magnetic areas on a continuous magnetic disc, the appearance or absence of which represents a data bit as a 1 or 0 [9]. In order to increase the storage density, the magnetic areas can be moved closer together. As the distance between adjacent magnetic areas is reduced, however, the likelihood of the amalgamation of adjacent magnetic areas is increased. This is analogous to water droplets on a pane of glass: as the density of droplets increases, the droplets will being to irreversibly coalesce. The amalgamation of magnetic areas means the irrevocable loss of data. Lateral patterning of the magnetic film is seen as a likely candidate for reducing the separation of adjacent magnetic areas without

loss of data [10, 11]. The continuous magnetic film is patterned into islands, each representing an individual data bit, which are physically separated to prevent amalgamation. The interplay between adjacent magnetic islands is, however, governed by a wealth of competing interaction processes which need to be fully understood before such a device can be successfully realised and its limitations quantified.

Another emerging field reliant upon magnetic processes is that of "spintronics" [12]. Spintronic logic devices are a proposed successor to the electronic transistor; a device already reduced in size to a point which approaches the limit of what is practically achievable [13].

The now famous Moore's Law [14], describing the exponential increase in transistor density over time, cannot continue indefinitely using traditional silicon semiconductor devices. Though the hard limit on transistor size may be the atomic scale [15], the practical limit is dictated by power, i.e. the amount of energy required per unit time for the transistor to operate, as electronic devices rely on manipulating packets of charge to perform computational tasks. As the devices reduce in size, the power density increases to unmanageable levels. A new branch of devices, known as "spintronic" devices, are being developed with the aim of overcoming this limitation [12]. Spintronic devices manipulate the electron spin, rather than the traditional method of exploiting the charge, to transmit information. The electron has two convenient spin states (up and down) in which it can exist, which can represent 1 and 0. In theory then, a single electron could carry a individual bit of information throughout a logic process. Creating and controlling a spin-polarised current can only be achieved using magnetic materials [16]. Fundamental magnetism research in this area must pay particular attention to the magnetic properties at material interfaces, as it is the control of the electron spin across such interfaces that is critical to the realisation of a device of this type [12, 17].

The creation of these devices relies on the control of the magnetic properties of a material, which can be achieved in a number of ways. The most direct way is simply to change the material structure, e.g. its size or composition. For a given structure, external factors, such as temperatures and applied fields, can produce additional changes. The ability to dynamically induce changes within a system is often fundamental to the exploitation of such a system in a useful device, for example to result in switching a data bit from a 1 to a 0. As devices get smaller, an almost universally desirable trait, the details of the magnetic properties on an atomic scale become far more important, and the bulk properties less so. This can lead to new possibilities for exploitable properties, but can also lead to unanswered questions. By studying the behavioural changes in systems outside of the bulk regime, these atomic

scale interactions can be investigated [18–20]. Reduced dimensionality systems, i.e. ultrathin systems which can be considered two dimensional, represent an ideal example for study, as by their nature they have properties different to that of their bulk, three dimensional counterparts [21, 22].

To study magnetic interactions within such systems, it is necessary to include interfaces between different regions displaying different magnetic behaviour. A convenient method to enable this is to study polarisable materials. These do not display a natural spontaneous moment, but gain an induced moment when in proximity with a magnetic material [23]. This provides not only an interface across which the magnetic moments are fundamentally coupled, but removes the added influence of a second magnetic layer with potentially independent magnetic bulk properties. The interface between a ferromagnetic and polarisable material then represents the desired interface between regions displaying non-bulk properties, providing an avenue for studying the fundamental, atomic scale, magnetic interactions in a coupled magnetic system.

In these magnetic systems containing polarisable materials, the key properties originate due to the itinerant behavior of the conducting electrons [23]. To conduct studies on materials of this type it is therefore necessary to first understand the electronic origins of magnetism.

Chapter 2

Introduction

2.1 Magnetism

Magnetism has a quantum mechanical origin due to the intrinsic angular momentum of electrons, which is referred to as their *spin*. The spin moment of each electron is dictated by its spin quantum number, which can only take one of two values $\pm 1/2$, which produces angular momenta of $\vec{S} = \pm\hbar/2$ [23]. These are commonly referred to as spin-up and spin-down. The measurable spin moment, along an applied field direction, produced by the angular momentum of a single electron can be calculated using [24]:

$$\mu_S = g\frac{-e}{2m_e}\vec{S}, \tag{2.1}$$

where e is the charge carried by an electron, m_e is the rest mass of an electron, and $g \approx -2$. This produces spin-moments of $\pm\mu B$. However, an electron bound to an atom has an additional moment due to its orbit around the nucleus, analogous to the path of an electric current within a solenoid. These spin and orbital moments are electromagnetically coupled through the spin-orbit interaction [23]. This leads to a subtle energy shift between electrons of opposing spin states within the same electron orbital. In the simplest model, these electron orbitals fill in accordance with Hund's rules [23]. For an isolated atom, these rules are followed to ensure the lowest possible energy state is realised, i.e the orbital half fills with electrons which are in an identical spin state, filling all available spaces for this spin state before the opposite spin state is allowed.

For most elements, these rules would lead to a nett spin moment due to the unpaired electrons in any unfilled shell. However, as atoms form into molecules, they share unpaired electrons through covalent bonding, removing any nett spin

moment. In materials with highly localised outer shells, such as the f-shell, the sharing of electrons with neighbouring atoms is not energetically favourable, leading to a retention of a strong orbital moment. Materials in which this occurs are the "Rare Earths" such as Gd and Ho [25].

There is another class of materials within the periodic table which can show spontaneous magnetic order. These are the transition metals Fe, Co and Ni. Rather than being highly localised, the outer d-bands of these metals overlap [26], allowing them to share electrons in an *itinerant* electron band. To understand the origin of a spontaneous moment in an itinerant system, the energy of electrons within this conduction band must be considered.

2.1.1 Itinerant Magnetism

In an itinerant, delocalised electron band, the orbital moment is minimised as the electrons no longer follow well defined orbital paths. The electrons can be considered *orbitally quenched* [27]. The spin-orbit interaction is subsequently minimised and all electrons can be assumed to have the same energy. The lowest energy state is therefore realised through a population with equal numbers of spin-up and spin-down electrons, as the nett moment is minimised. These populations can be considered as two equally populated electron sub-bands. However, in order for a material to be magnetic, there must be a population difference between these two sub-bands (creating a nett spin moment), which increases the kinetic energy of the electron system making it energetically unfavourable.

One way in which a population imbalance can be stimulated is through the application of an external magnetic field [28]. If a field is applied, a shift in the energy levels of the two spin states at the Fermi energy occurs [23]. This lifts electrons in one sub-band above the Fermi energy while lowering the energy in the other sub-band. This arrangement is energetically unfavourable, and so those electrons above the Fermi energy reverse their spin and swap sub-bands. This creates the desired population imbalance between the number of electrons with each spin, and so a magnetic moment is formed. This effect is Pauli paramagnetism [29]. The magnetic moment, M, induced by applied field, H, in a Pauli paramagnet then follows the relation

$$M = \chi_{\mathrm{P}} \cdot H, \tag{2.2}$$

where the Pauli susceptibility, χ_{P}, is a temperature independent material constant [29]. Paramagnetism can also exist in ferromagnetic materials at sufficiently high

temperatures. Above the magnetic ordering temperature (discussed in section 2.1.2), thermal excitations cause the spontaneous moments carried by the atoms within the lattice to lose alignment with their neighbours resulting in zero nett moment [30]. An applied field exerts a torque on each moment which seeks to align them with the applied field direction and generate a nett moment once more. Paramagnetic systems revert back to the equilibrium state, and lose their gained nett magnetic moment, if the applied field is removed.

The second process which can result in a population imbalance between the two spin-states arises due to a significant, additional contribution to the total energy from the exchange interaction between electrons; the result of the overlap of the electron wavefunctions [31]. In order to obey exchange symmetry, the total wavefunction, comprised of spin and spatial contributions, of two interacting electrons must be antisymmetric [23]. If the spin-states are symmetric (i.e. the spins align) then the spatial state must be antisymmetric which, due to the exchange interaction, allows the electrons to be further apart in real space, reducing the electrostatic potential [31]. This means that if the electron density of states is sufficiently high, the spins will begin to align spontaneously. In order that each band is filled exactly to the Fermi energy, the more populated band shifts to a lower energy while the less populated band shifts to a higher energy. The nett result is the same as that of the Pauli paramagnetic response outlined above. The exchange interaction thus leads to an additional contribution to the magnetic susceptibility, known as the Stoner factor [32]. The total susceptibility becomes [23]

$$\chi_{meas} = \frac{\chi_{\mathrm{P}}}{1 - U \cdot D\left(E_{\mathrm{F}}\right)} = \chi_{\mathrm{P}} S, \tag{2.3}$$

where U is the coulomb energy due to the exchange interaction, $D\left(E_{\mathrm{F}}\right)$ is the electron density of states at the Fermi energy, and S is the Stoner enhancement factor [32], a temperature dependent material property [29]. The onset of ferromagnetic order is then defined as the point at which an infinite susceptibility can first exist [30], and so materials are ferromagnetic if they satisfy the relation:

$$U \cdot D\left(E_{\mathrm{F}}\right) \geq 1. \tag{2.4}$$

This defines the Stoner Criterion [32]. Materials for which this condition is satisfied are ferromagnetic (FM). The only elements to do so are Fe, Co and Ni. The susceptibility is only infinite for systems displaying ferromagnetic order which require an infinitely small field to reverse the magnetisation direction. In reality, a finite coercive field, H_{C}, is required to switch the direction meaning dM/dH is also finite.

This non-zero coercivity causes a magnetic hysteresis effect meaning the magnetic moment is not only dependent on the applied field strength, but the history of the applied field [24]. This will be discussed in more detail in section 2.3.2.

When considering a magnetic material above the atomic scale, it is convenient to ignore the behaviour of individual itinerant electrons in the Stoner Model, and instead consider each atom as an independent magnetic particle coupled to those around it. This forms the basis of the Curie-Weiss Model [24]. In this Model, the magnetisation within a solid permeates the system as a lattice of coupled moments centred at the atomic positions. Each moment is coupled to each neighbouring moment with a strength defined by the moments and the coupling constant, J. Immediately, this simplification ignores long-range interactions. A further simplification can be made by ignoring local variations in J and instead assuming that each neighbouring pair of moments is coupled by the average value of J throughout the lattice. This is the basis of mean-field theory [24], which is sufficient for a basic description of the lattice behaviour. By summing over all interactions, the Hamiltonian for such a system can then be described as

$$\mathcal{H} = -\frac{1}{2}\sum_{i \neq j} J\mathbf{m}_i \cdot \mathbf{m}_j, \tag{2.5}$$

where i and j are the atomic indices and $\mathbf{m}_{i/j}$ are the atomic moments. If $J > 0$, the magnetic potential described by the Hamiltonian is clearly maximised for collinear moments and thus ferromagnetic alignment represents the energetic ground state. Conversely, if $J < 0$, antiferromagnetic alignment is energetically favourable. Thermal energy within the system seeks to misorientate the aligned moments. The energy required to overcome the magnetic potential leads directly to an approximation of the temperature above which spontaneous magnetisation is lost; the Curie Temperature, T_{C}. Investigating the manner in which these magnetic bonds break, through the application of heat, can elucidate the true nature of the coupling between adjacent moments. Thus, measurements of the global magnetic response can indirectly probe the magnetic behaviour on a fundamental scale. This is the basis of magnetic ordering studies.

2.1.2 Magnetic Ordering

The principle of magnetic ordering studies is to add thermal energy to a magnetic system in order to overcome the magnetic order, as the nature of the transition from a magnetic to a non-magnetic state can yield information about the magnetic coupling mechanisms present. Within the mean-field approximation, Landau theory

[33] shows the order disorder transition is governed by a simple power law:

$$M \propto (T_{\mathrm{C}} - T)^{1/2}\,. \tag{2.6}$$

This simple model, however, breaks as T_{C} is approached as it assumes that all regions of the sample remain the same. This is clearly unphysical as certain moments begin to reverse. It also ignored the magnetic correlations associated with long-range order which become critical as T_{C} is approached [34]. To more accurately describe the ordering behaviour, a less simplistic approach is required.

To determine the nature of the coupling within the lattice, the first indicator is the ordering temperature: a higher T_{C} means stronger coupling. However, T_{C} is strongly influenced by, for example, the finite volume of the sample [35, 36]. A more illustrative measure can therefore be how rapidly the magnetisation is lost as T_{C} is approached. In the Landau model, the exponent of 0.5 crudely predicts that all lattices will approach T_{C} similarly. However, the actual behaviour is dictated by the allowed orientations of the moments within the lattice, because a magnetic lattice of coupled moments, with a magnetic potential described by equation 2.5, has an energy cost for reorientating an individual moment.

The impact of this energy cost can be determined by considering the Helmholtz free energy, which for a ferromagnetic system can be described as:

$$E = U - TS, \tag{2.7}$$

where E is the energy in the system, U is the magnetic potential, T is the absolute temperature and S is the entropy [37]. At $T = 0$, there are no thermal excitations, and the free energy is governed only by the magnetic potential described by the Hamiltonian. From the ferromagnetic ground state, full reversal of an individual moment is the action requiring the most energy. In an Ising spin system where d, the number of spin degrees of freedom, is 1, and so the spins are constrained to be parallel or antiparallel to a specific unit vector (i.e. up/down), this reversal is the only excitation possible. As thermal energy is introduced into an Ising system, there is a finite chance that this potential can be overcome, resulting in the reversal of a magnetic moment within the lattice. The simplest case to consider is a 1D lattice within which a single reversed moment has an entropy proportional to N, the number of identical sites within the lattice [37]. The entropy then clearly scales with the extent of the system, whereas the potential which must be overcome to reverse one moment remains constant. For any 1D system, this dominance of the free energy by the entropy results in a lack of long-range order at all finite temperatures.

If an additional spacial dimensionality is included, creating the 2D Ising system, a magnetic defect can extend over both dimensions. The energy cost of creating a defect scales with the defect size. However, the entropy gain can also be shown to scale with the defect size [38]. This creates a regime in which magnetic order can exist, even for an infinite system. In any magnetically ordered lattice, there will be a finite temperature above which TS exceeds U and the magnetic order is lost. This is an alternative description of the Curie Temperature, T_{C}. As a 2D Ising system approaches T_{C}, the high energy cost of reversing an individual moment leads to the preservation of the total magnetic moment until T is very close to T_{C}. At this point, the thermal excitations are sufficient to reverse a significant proportion of individual moments and the magnetisation very rapidly diminishes to zero [30].

The magnetic moments within the lattice can also be allowed additional degrees of freedom. If one additional degree of freedom is introduced, so that moments are constrained to point in any direction within a 2D plane, the XY ($d = 2$) spin system is formed. The final, third degree of freedom allows the moment to point in any direction, forming the Heisenberg, $d = 3$, system.

In both of these cases, the energy required to reorient a moment becomes a function of the degree of reorientation, with the minimum energy tending to zero. This produces regimes in which *magnon modes* can exist. These are the magnetic equivalent of phonon modes and are magnetic excitations mediated through the magnetic lattice. The number of magnon modes which are excited then dictates the degree of magnetisation which is lost from full alignment. This can be achieved by integrating the magnon density of states and, for a 3D Heisenberg system, results in Bloch's law [39] which states that, in the low temperature region,

$$M = M_{T=0} - aT^{3/2}, \tag{2.8}$$

where a is a constant. If these calculations are instead performed for a 2D lattice, the reduced coupling strength within the lattice creates a regime in which the magnetic excitations are sufficient to overcome the ferromagnetic alignment at all temperatures for Heisenberg systems. This is the basis of the Mermin-Wagner-Berezinskii (M-W-B) theorem [40]. However, this theory assumes that the moments can be orientated in any direction without any additional energy cost, or that there is no preferential alignment direction. There will, however, be preferred alignment directions within a geometric arrangement of lattice points. This anisotropy requires an additional energy cost to reorientate the moments which scales with the size of the magnetic excitation. The lowest energy, longest wavelength excitations are the most

long-ranged, and are thus suppressed allowing ferromagnetic order to be preserved. A 3D Heisenberg system, can dissipate thermal energy with much greater efficiency than an Ising system generally leading to a significant increase in T_C and resulting in a much more gradual decline in the nett moment of the lattice as T_C is approached [30].

In the 2D XY system, the addition of anisotropy is not sufficient to produce a globally ordered phase at any finite temperature. Instead, the moments form into a pseudo-ordered vortex state, where the moments form into concentric rings. The energetic ground-state of such a vortex system produces equal numbers of clockwise and anti-clockwise vortices (vortices and anti-vortices) which form into pairs in order to minimise the free energy. These vortex anti-vortex pairs have a small nett moment. However, these pairs also have a lower entropy than unpaired vortices. As the temperature increases, the entropy term of the free energy begins to dominate and it becomes energetically beneficial for the pairs to separate. Unpaired vortices carry no nett moment. This is a topological phase transition called the Kosterlitz-Thouless-Berezinskii transition [41] which allows the ordering of the otherwise disordered 2D XY phase.

As these different states have different expected behaviours as they approach T_C, their combination of spin and spacial dimensionalities can be investigated by observing the magnetisation as a function of temperature. The Landau model (equation 2.6) can then be expanded upon by allowing the exponent to differ for different ordering models. The magnitude of the total moment (i.e. the moment summed over the whole lattice) is then described by a power law where the magnetisation, M, as a function of temperature, T, is of the form

$$M = (T_C - T)^{\beta}, \tag{2.9}$$

where, for an ideal system, the exponent, β, is governed only by the spin and spatial dimensionalities available in the lattice [30]. As this represents a critical phase transition, from the ferromagnetic to paramagnetic phase, β is referred to as the *critical exponent*. Since the magnetic interactions have no dependence on the chemical composition of the layer, β falls into one of several universality classes depending on the spin and spatial degrees of freedom available. β is therefore a constant for each combination of spin and spatial degrees of freedom regardless of sample composition, geometry, T_C etc. Determining both the spin and spatial degrees of freedom is then achieved by measuring the exponent of the magnetic ordering. A summary of the universal critical exponents of magnetic ordering are presented in table 2.1[30].

β	Spin(d)	Spatial(D)
0.125	1	2
0.23	2	2
0.31	1	3
0.33	2	3
0.35	3	3

Table 2.1: Critical ordering exponents, from [30].

These exponents are the result of experimental determination with the exception of the 2D Ising case for which this exact solution can be derived. Due to the similarity in exponents, the difference between the magnetic responses for these different dimensionalities is quite subtle. Idealised plots of the normalised magnetic ordering behaviour for 2D Ising, 2D XY and 3D Heisenberg classes are illustrated in figure 2.1. As $M(T = 0)$ and T_C are material dependent quantities, both are normalised to 1 to aid visual comparison.

Ideal critical ordering behaviour is difficult to achieve experimentally; any sample or field inhomogeneity will cause small variations in local magnetic behaviour. In the simplest case, this will lead to a distribution of ordering temperatures within the material. A Gaussian distribution of ordering temperatures causes a Gaussian convolution to be applied to the ordering data. The most pronounced effect of this convolution is a residual moment above T_C manifested as an extended tail in the ordering data. However, the data will be subtly altered at all temperatures, with the critical ordering exponent, β, also subtly altered.

If, rather than an inhomogeneous field, an applied field is present, then an enhancement to the moment at all temperatures will be observed due to the magnetic susceptibility, χ, of the sample which varies as $\chi = dM/dH$. As the sample approaches T_C, M approaches zero and the susceptibility diverges. An applied field therefore leads to a pronounced enhancement of the moment at T_C, and extended tail above T_C. Experimentally, a true zero field can be difficult to achieve using electromagnets due to their non-zero coercivity. Helmholtz coils are used where possible to minimise both inhomogeneity and coercivity. However, as M varies as a function of temperature, and χ varies as a function of M, it follows that χ varies as a function of T. Furthermore, as $M(T)$ is governed by the magnetic spin and spacial dimensionalities, $\chi(T)$ must also be. This forms the basis of the Curie-Weiss law [24],

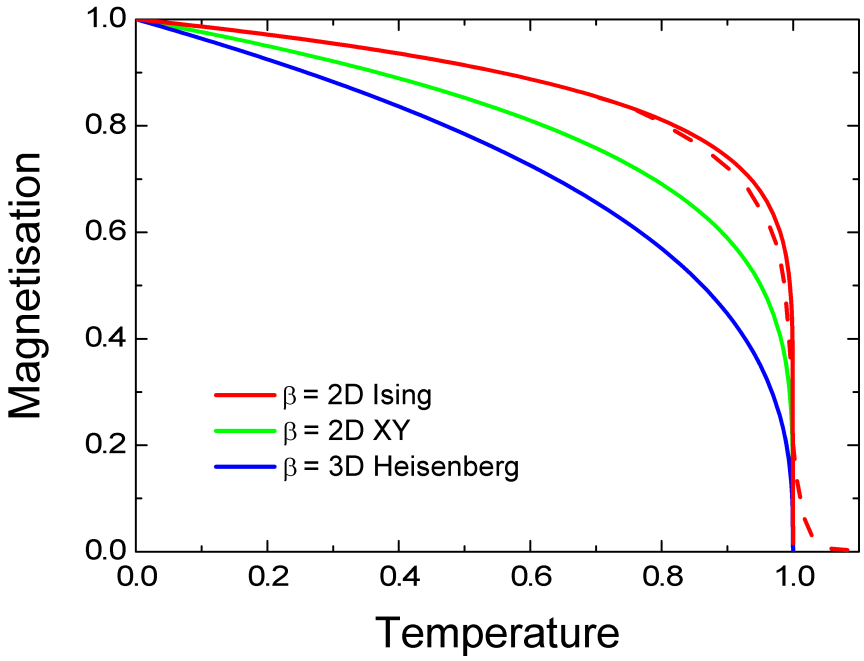

Figure 2.1: The expected temperature dependent magnetisation curves for universality classes with ideal critical exponents (solid lines). Dashed line shows a Gaussian convolution to the 2D Ising case to show the influence of field or sample inhomogeneity on the magnetic ordering. T_{C} and $M(T=0)$ are arbitrarily normalised to 1 to aid visual comparison.

$$\chi = \frac{1}{(Tc - T)^{\gamma}}, \tag{2.10}$$

where γ is a critical exponent. This technique is employed to analyse data above T_{C} making it a useful, complementary technique to analysis of $M(T)$ through β. A final critical exponent can be extracted from the magnetic response to the applied field at T_{C}, which follows the relation [24]

$$M = H^{1/\delta}, \tag{2.11}$$

governed by a third critical exponent, δ. These three ordering exponents are clearly highly correlated, and in fact it can be shown that the three are related through the Widom equality [42]:

$$\gamma = \beta(\delta - 1). \tag{2.12}$$

γ	δ	Spin(d)	Spatial(D)
7/4	15	1	2
-	15	2	2
1.2373(2)	4.78	1	3
1.3177(5)	4.81	2	3
1.388	4.78	3	3

Table 2.2: Critical exponents compiled from [30] and [24].

More practically, both δ and γ have theoretically or experimentally determined values for each universality class, shown in table 2.2. γ is omitted for the 2D-XY case as it is not defined, due to the evolution of magnetic correlation lengths within the array. As discussed, γ is dictated by the susceptibility of the system just above the ordering temperature. Above the ordering temperature, the moments are globally disordered, but some localised order may remain. The magnetic correlation length, which will be discussed in more detail in chapter 7, is a measure of the size of these locally ordered regions. Kosterlitz [41] showed that the correlation length, ξ, in the 2D-XY regime varies as

$$\xi \approx \exp\left(b(T_{\mathrm{C}} - T)^{1/2}\right), \tag{2.13}$$

where $b = 1.5$. Similarly, the susceptibility, rather than being governed by the Curie-Weiss law, follows the relation

$$\chi \approx \exp\left(b(T_{\mathrm{C}} - T)(2 - \eta)\right), \tag{2.14}$$

where η is the critical exponent of the correlation function, and in this case is equal to 1/4. In this thesis, phase transitions with various dimensionalities will be studied. In order to consistently perform this analysis, the magnetisation as a function of temperature will predominately be investigated, and so β is the experimental value of interest.

Regardless of investigative method, these descriptions of magnetic behaviour all rely on the material being treated as bulk, i.e. far from an interface or boundary; the theoretical models are reliant upon the assumption of an infinite plane of interconnected moments (approximated by periodic boundary conditions). At an interface, the material and electronic structures are unavoidably altered, potentially causing a significant modification to the magnetic behaviour. Any experimentally determined ordering exponents must therefore be treated carefully, and as such will

be termed *effective* exponents denoted, for example, β_{eff}, to distinguish them from determinations of bulk behaviour. These effective exponents are still meaningful, and may still fall into one of the described universality classes. However, the effect of interfaces on the magnetic lattice can not be ignored.

2.2 The Magnetic Interface

As metallic heterostructures reduce in size, the magnetic behaviour will begin to deviate from that of the bulk because of the added influence of the material interfaces [43–45]. This has two contributing factors: the termination of the magnetic lattice, and shape anisotropy.

The termination of the magnetic lattice necessarily results from the termination of the crystal lattice at a material surface. Within the Curie-Weiss description, this termination leads to a modification of the magnetic behaviour of those moments closest to the interface due to a reduction in coupled nearest neighbours. The range of interactions is not, however, limited to nearest neighbour interactions in real systems; the greater the range of magnetic interactions, the further from the interface deviation from bulk magnetic properties will be observed.

This phenomenon was explored by Taroni and Hjörvarsson [46] who performed simulations on freestanding magnetic lattices of Ising spins. For a 10 monolayer (ML) film, assuming only nearest neighbour interactions, T_{C} was seen to decrease to 0.96 of that of an otherwise identical 40 ML film. The ordering behaviour was found to differ as a function of depth, as shown in the upper panel of figure 2.2 with an overall β_{eff} of 0.23. The simulation was repeated assuming the range of interactions was five interatomic distances (lower panel figure 2.2). Clearly the effect of the interface permeates further into lattice. This effect lead to a greater relative reduction in T_{C} to 0.92 of that of an otherwise identical 40 ML film. With this greater interaction range, β_{eff} was 0.40. This pronounced change in the effective exponent, induced by changing only the range of interactions, is greater than the difference expected of a dimensionality change (see table 2.1). This highlights the critical importance of interfaces in systems with reduced size, and also the difficulty in robustly determining the dimensionality of a terminated lattice.

For a buried interface between a ferromagnetic and non-magnetic material, though the crystal lattice may not be terminated at the interface, the magnetic lattice is. As such, the same modification in magnetic coupling, and thus change in magnetic behaviour, would be expected. At a buried interface between two ferromagnetic materials, however, the termination of the magnetic lattice is not implicit.

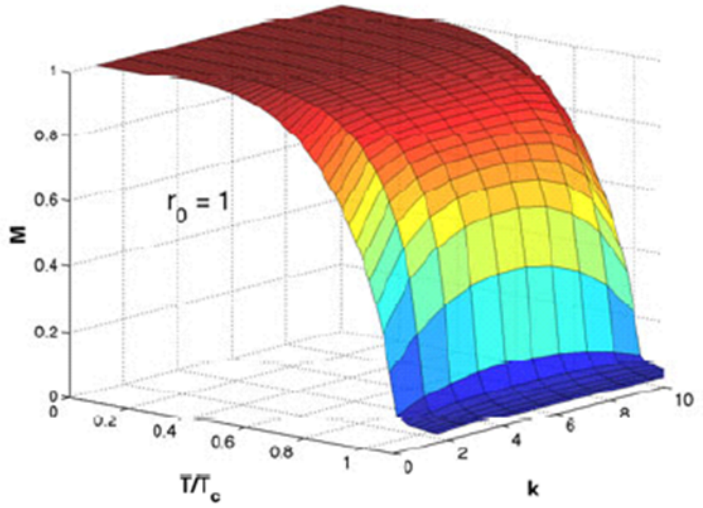

(a)

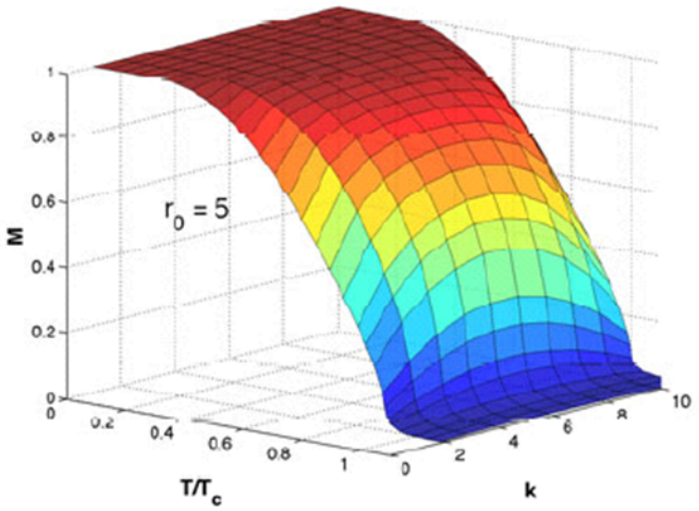

(b)

Figure 2.2: Taken from [46]. The simulated magnetic ordering behaviour of a free-standing, cubic lattice of Ising spins with a thickness of 10 ML. Upper and lower panels show the influence of the interfaces when considering the range of interactions to be 1 and 5 interatomic distances respectively.

In the Curie-Weiss model, the magnetic coupling between adjacent moments is a product of their proximity and magnitude with no consideration of chemical species; the two magnetic sub-lattices are directly coupled. It is possible, however, for the two sub-lattices to have different spin-dimensionalities where one sub-lattice may

support magnetic excitations in a direction forbidden in another. If a 2D lattice is magnetically adjacent to a 3D lattice, will the interaction between 2D and 3D moments stimulate magnetic excitations in the forbidden direction of the 2D lattice? The nature of the interactions at such an interface is poorly understood.

The second significant contribution is due to magnetic anisotropy, i.e. the preferential alignment of the magnetic moments along particular directions. A bulk, amorphous material, can be considered isotropic. A crystalline material is subject to magnetocrystalline anisotropy, where the crystal structure dictates preferential directions for magnetic alignment. In the simplest case, an infinite 2D rectangular lattice of moments will have a magnetic *easy axis* along the minor axis of the rectangle and a *hard axis* along the major axis. The easy axis represent the energetic minimum for the moment orientation, and the hard axis represents a local maximum. An applied field can align the moments to another direction if the field strength is sufficient to overcome the energy barrier. If the lattice is truncated those moments at the periphery will have an additional energy cost if they are aligned perpendicular to the interface. There then exists a competition between the latter *shape anisotropy* and the former magnetocrystalline anisotropy.

It is clear then that the effect of magnetic interfaces and truncated systems can have a significant effect on a wealth of magnetic properties including the magnetic ordering behaviour, the ordering temperature and the moment orientation. In this work, systems with reduced dimensionality will be investigated. In particular, the effect of a reduction in spacial extent of a film on the magnetic ordering dimensionality will be investigated.

2.2.1 Magnetic Proximity Effect

When considering the magnetic interface, it is prudent to consider the chemical potential between atomically adjacent materials, i.e. the interaction of electrons across the interface. In a metallic heterostructure, materials on both sides of an interface will have conduction electrons. These itinerant electron bands will hybridise and influence each other [47]. This can give rise to an observable effect whereby magnetisation is stimulated in some materials when adjacent to FM materials. This is known as the magnetic proximity effect. This results in the stimulation of ferromagnetic order in a paramagnetic material through direct contact with an inducing ferromagnet [48].

At a material interface, a chemical potential exists due to the different populations and energies of electrons on either side of the interface. In a metallic system containing itinerant electrons, the electrons form into electron clouds with individ-

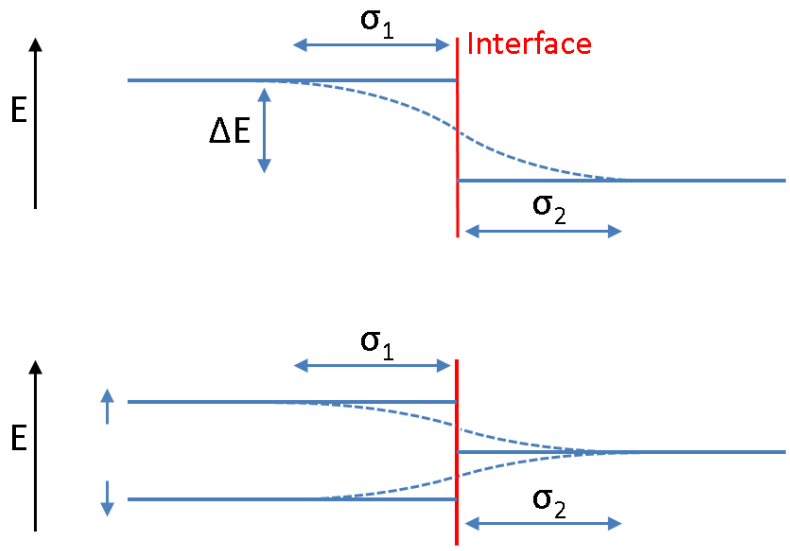

Figure 2.3: Electron diffusion produces a gradual and continuous transition in the electron energy across a material interface (upper panel). If one of these materials has a spin-split band, this splitting permeates into the neighbouring material (lower panel).

ual electrons not bound to particular atoms [47]. At an interface between two such materials, the electron clouds from the adjacent materials overlap and become hybridised. The electrons are then free to move between the two electron clouds, across the interface, as long as the nett electron flow remains zero. The potential is then blurred across the material interface as shown in the upper diagram in figure 2.3. If one of the materials at the interface is magnetic, the population imbalance between the two electron sub-bands leads to an energy difference between the two. Each sub-band then has it own chemical potential at the interface to the neighbouring material, as shown in the lower diagram of figure 2.3. The electron diffusion length within each material, σ, dictates the shape of this potential and is governed by the localisation of electrons within the material: localised electrons produce a narrow potential, itinerant electrons produce a broad, hybridised profile.

Although there is no nett charge flow across the interface, the spins of the electrons are preserved for a finite time in the new band. The balance of spin populations within the two materials, close to the interface, can therefore be modified. As this is the critical determinant of spontaneous FM order, the hybridisation can

induce FM order in a traditionally non-magnetic material. In practice, the material in which magnetic order can be stimulated must already be close to meeting the Stoner Criterion e.g. Pd and Pt [49]. The range of the induced magnetic moment is limited by the spin diffusion length, i.e. the finite penetration depth over which the polarisation of the diffusing electrons is maintained. Beyond this distance, scattering processes lead to the equilibrium spin state of the material being met, and any modification to the electron population being lost.

In the case of the itinerant paramagnet Pd, a material which is very close to fitting the criteria for spontaneous ferromagnetic order, atomic contact with a ferromagnetic material such as Fe, leads to a hybridisation of the Fe 3d and Pd 4d electron bands. This increases the electron DOS sufficiently in the 4d electron band causing the band to become exchange split, and thus the Pd to become independently, spontaneously ferromagnetic [50]. The inverse process, unpolarised electrons diffusing from the PM into the FM, can lead to the suppression of FM order in typically FM materials [51].

Due to the finite probability of the diffusing electron undergoing a spin-flipping scattering event per unit distance, the nett polarisation of the diffusing electrons exponentially tends towards that of the conducting material with increasing distance from the interface. A semi-quantitative description of the polarisation, is given by [52]:

$$\sigma_{\mathrm{S}}(r) \sim \chi_{\mathrm{P}} \frac{3k_F^2}{\pi r} \exp\left(-\frac{2k_{\mathrm{F}} r}{\sqrt{S/3}}\right) \tag{2.15}$$

where r is the distance from the polarising atom, χ_{P} is the Pauli susceptibility, k_F is the wave vector at the Fermi surface, and S is the Stoner enhancement factor. As the magnetisation is likely to scale with the degree of polarisation of the diffusing current, this description can be applied to the magnitude of the induced magnetic moment. The range of the induced moment is therefore dependent only upon material constants and the temperature dependent Stoner factor, S. A modification to this polarisation description arises due to long-ranged RKKY interactions [53–55]. The influence of these interactions is oscillatory as a function of distance from the material interface, successively enhancing and suppressing the polarisation. As the effect is small relative to the contribution described by equation 2.15, it only provides a noticeable contribution in the outermost polarised regions. For simplicity, it will be ignored.

Itinerant magnetic systems containing induced moments will be of primary interest to this work because they represent systems in which the magnetic behaviour

at an interface can be studied. The magnetic behaviour at interfaces is a crucial area of study for the realisation of spintronic devices which rely on the manipulation of spin polarised currents across material interfaces. Conducting a spin polarised current can only be achieved using magnetic materials. Due to the hybridisation of the electron bands at such an interface, the magnetisation at the interfaces are intrinsically coupled. The nature of this coupling is, however, poorly understood. In patterned materials, desirable for magnetic data storage devices, additional interactions between the islands are introduced, adding a further layer of complexity to the magnetic coupling present in the system. To study these types of interactions, methods for probing the behaviour of the magnetic lattice are therefore required.

2.3 Studying Magnetism

Studies of the magnetic ordering behaviour, which are necessary to probe the coupling within the magnetic lattice, are commonly conducted using Superconducting Quantum Interference Device (SQUID) magnetometry. These measurements are highly sensitive to the total moment of a sample and as such, are of particular use when studying freestanding crystals or encapsulated powders. A layered metallic sample, such as those of particular interest to this work, must be grown on a substrate material and may have only a small volume of the sample which is magnetic. The high sensitivity of the SQUID technique then makes any small diamagnetic or paramagnetic response from areas within the sample which are not of particular interest, difficult to remove. As the sample orientation can also not be accurately controlled, directional studies are difficult. As such, in this thesis, scattering techniques will be employed throughout. These involve scattering a particle (either a photon or a neutron) from the sample, and measuring the response. The details of these studies, and their sensitivity to the magnetisation within the sample will be discussed below and in the following two chapters.

Initial categorisation of samples as well as previous work was performed using the magneto-optic Kerr effect (MOKE). These previous studies were performed by collaborators at the University of Uppsala and form the foundation of the studies presented in this thesis.

2.3.1 MOKE

The mageneto-optic Kerr effect is a table-top technique employing laser generated, polarised optical photons to probe the total moment of magnetic films. The magnetic sensitivity of these optical photons is manifested as a rotation in the reflected

photon polarisation with respect to the incident polarisation [56]. The electric field of an incident photon exerts a force on the photons within the target material in accordance with $F = qE$. The oscillatory motion of the electrons interacts with the magnetic field within the material (due to the Lorentz force law: $F = q(V \times B)$, creating an additional component of the electric field vector in a direction perpendicular to both the magnetic field and polarisation directions, and with a magnitude proportional to the sample magnetisation. This additional component induces an ellipticity in the polarisation of the reflected photons, with a major axis rotated from the incident polarisation direction. Quantification of this Kerr rotation, typically achieved by separating the additional component from the reflected beam with a second polariser, then directly yields a value proportional to the sample magnetisation.

This magnetic sensitivity can be exploited in a number of geometries in order to probe sample magnetisation in different directions. Sensitivity to the in-plane magnetisation desired in this work is possible in the "Longitudinal Geometry" shown in figure 2.4. An external field is applied in the in-plane direction using a Helmholtz coil. The angle of incidence, and thus of reflection, is fixed to be approximately 60°. This is due to the trigonometric dependence of the degree of rotation arising from the Lorentz force vector cross product. At 90°, used in the polar MOKE geometry, the additional component acts along the beam direction, producing no measurable rotation. 60° maximises the rotation, increasing signal to noise.

The high flux of modern lasers allows high count rates, and fast data collection. As there is little absorption of optical photons in air, experiments do not need to be conducted in vacuum allowing greater flexibility and interchangeability of sample environments. Cryogenically cooled sample environments, with optically transparent windows, incorporating electromagnetic coils allow routine access to a wide range of temperatures and fields. Optical photons, however, only have a relatively short penetration depth into metallic materials (typically around 20 nm) [57], potentially causing difficulties as sample thicknesses increase. MOKE is only sensitive to the volume integrated magnetisation within the penetration depth of the beam. MOKE does not provide depth resolution nor element specificity.

Employing MOKE to simply record the magnetic response of a systems is, however, not very instructive. Nor is recording the magnetic response while dynamically ramping the sample temperature as magnetic systems tend to form into domains [24]. The most revealing measurement is one of the field response of the magnetisation, i.e. the response of the system to a changing internal energy, separate to that of thermal excitations. This is the basis of magnetic hysteresis studies.

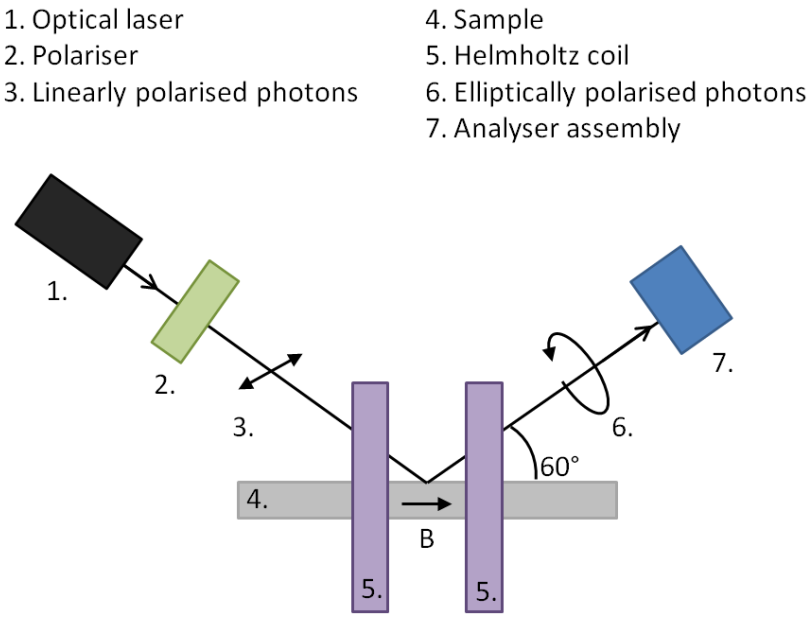

Figure 2.4: Longitudinal MOKE employs linearly polarised optical photons reflected off a magnetic sample surface. The Kerr rotation of the major axis of the elliptically polarised reflected photons, with respect to the incident polarisation, is then proportional to the in-plane sample magnetisation.

2.3.2 Magnetic Hysteresis

Magnetic hysteresis is the inability of a system with spontaneous magnetic order to reach $M = 0$, $H = 0$ through the application of an applied magnetic field. Instead, the magnetisation will trace a path around a loop centred on $M = 0$, $H = 0$ as shown in figure 2.5. The shape of the loop contains important information about the behaviour of the system.

A ferromagnetic material, when cooled from above its ordering temperature, can exhibit zero nett moment due to the formation of magnetic domains the reorientation of which is energetically challenging [24]. With the application of an external field, the domains can be aligned. Once all the moments are aligned with the field, further increase of the applied field strength yields no further increase in sample magnetisation, and the material is said to have reached its saturation magnetisation, M_{Sat}. The minimum field required to fully align the moments is then H_{Sat}. An increase in temperature within a magnetic system will reduce the maximum achievable degree of alignment to an applied field. This leads to a reduction in M_{Sat}, and potentially an increase in H_{Sat}, as T_C is approached.

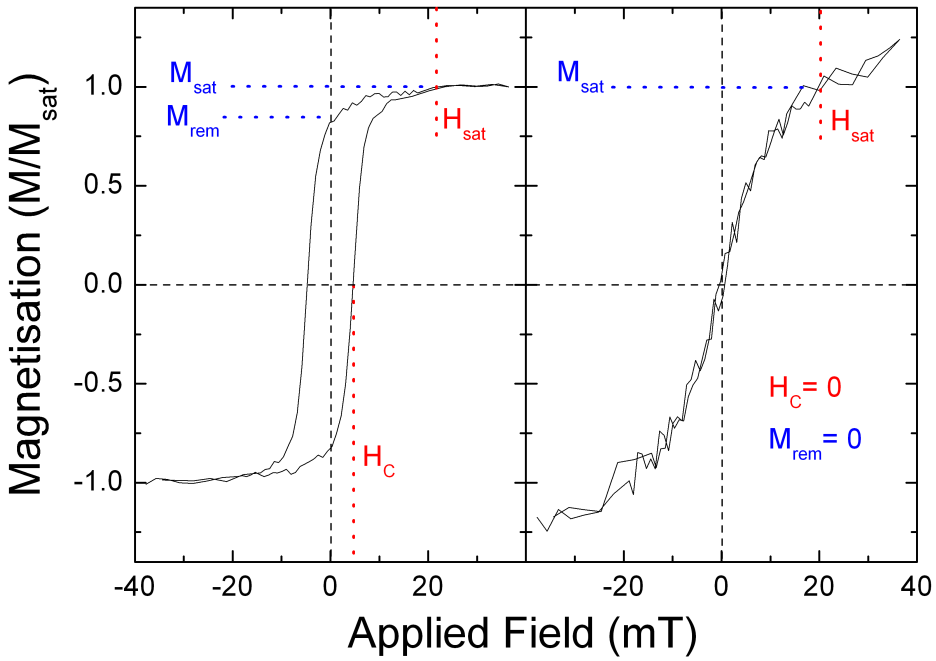

Figure 2.5: Example hysteresis loop data from a system in a ferromagnetic phase (left) and paramagnetic phase (right) with key parameters indicated.

If the field is reduced from saturation, the system does not have enough energy to revert back to its starting position at $H = 0$, $M = 0$ and so maintains a remanent moment, M_{Rem}. M_{Rem}, after the application of a saturating field, is an unbiased measure of the samples temperature dependent, spontaneous magnetisation since it removes the influence of the domain structures. In order to remove the sample magnetisation in a system with non-zero remanence, an externally applied reversing field is required. The minimum field strength required to remove this magnetisation is the coercive field, H_c, which is a measure of the energy required to reorientate the magnetic structures within the sample. In larger structures, the increase in sample volume makes magnetic reorientation more difficult, increasing H_c. Conversely, thermal energy within the system makes it easier to overcome the magnetic alignment, and thus lowers H_c. The collapse of the coercive field to zero is an accurate measure of the thermally driven loss of ferromagnetic order at T_C as it necessarily coincides with the loss of the remanent moment and thus the onset of the paramagnetic phase [30].

The energy required to rotate moments, and hence the coercive field, within a system is influenced by the magnetocrystalline and shape anisotropies of the mag-

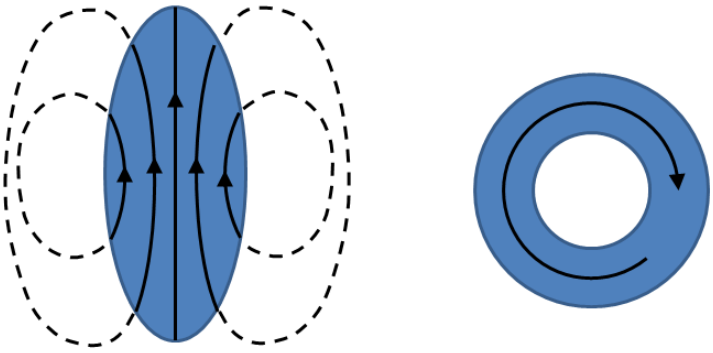

Figure 2.6: Minimising the stray field in an ellipsoid (left) leads to an energetically favourable moment formation which reduces the overall moment in the element. Concentric alignment of moment in a toroidal element (right) produces no stray field.

netic lattice. The resultant preferential alignment directions can produce easy and hard magnetic axes. These represent global and local minima of the moment orientation energy respectively. When a system is aligned along its magnetic easy axis, the energy cost for reorientating the moments is maximised, and so the coercive field is also maximised. In a system which lacks anisotropy, the energy cost for reorienting the moments within the lattice is negligible, and so the coercive field vanishes to zero. This results in the loss of long-range order predicted by the Mermin-Wagner-Berezinskii theorem [40].

The shape anisotropy will also influence the saturation moment recorded due to the demagnetisation factor. A detailed description is given in [23]. In short, an infinite system can be assumed to contain collinear moments throughout. A finite system, however, produces a stray field which it is energetically beneficial to minimise. This affects the orientation of moments throughout the lattice volume, and collinearity it lost. This reduces the nett moment carried by the lattice. For simple geometric shapes, this demagnetisation predictably affects the total moment, and so tabular values of demagnetisation factors exist. As demonstrated in figure 2.6, an ellipsoidal element has a reduction in its nett moment due to the stray field. A toroidal element allows concentrically aligned moments with no stray field and so its demagnetisation factor is zero.

In a paramagnetic material, M_{Rem} and H_c are both equal to zero. However, the application of an external field can still align the randomly orientated moments within the system. Therefore, although the system no longer displays

magnetic hysteresis, H_{Sat} and M_{Sat} both remain as positive, non-zero quantities. As a paramagnetic system is driven towards alignment by an external field, it transitions through an intermediary phase of locally ordered, correlated magnetic regions. As the field strength increases, these regions expand by amalgamating with those around them until the system is globally aligned, and saturation is reached. The shape of the field dependent magnetic response, in the $0 \leq H \leq H_{Sat}$ region, reflects this evolution. In the region close to $H = 0$, the magnetic regions are small, and thus easily reoriented, and so the susceptibility is high and a rapid increase in M with H is observed. As H_{Sat} is approached, the larger magnetic regions reduce the susceptibility and so a gradual response of M to H is seen. This results in the field response displayed in the right panel of figure 2.5.

The size of the magnetic regions present within the system can be examined by investigating the field response of a paramagnetic material using Langevin Analysis (originally described in [58], summarised in English in [23]). This involves fitting the magnetic response as a function of field to the relation

$$M(H) \propto n\mu L\left(\frac{\mu_0 H\mu}{k_B T}\right) \tag{2.16}$$

where n is the number of atoms per unit volume in the correlated regions with nett moment μ, and $L(x) = 1/tanh(x) - 1/x$ is the Langevin function [58]. All other parameters carry their usual meanings. The size of the correlated region can then be derived from the nett moment by assuming uniform magnetic distribution. For systems where the material thickness is sufficiently thin (< 1 nm) this is achieved by assuming each region is an out-of-plane cylinder with a diameter equal to the extent of the correlated region. The size of the magnetic regions formed is temperature dependent, strongly decreasing with increasing temperature. Meaningful quantification of the region sizes is therefore obtained from analysis of data as close as possible to T_{C}.

The combination of MOKE and hysteresis loop analysis is undoubtedly powerful. However, the lack of element selectivity and tunable depth sensitivity using MOKE introduces limitations. When taking measurements from relatively large systems (with a thickness of 100s of nm) which are magnetically homogeneous, MOKE is ideal, and is commonly used. Such a system would be expected to display similar characteristics of a bulk material. The magnetic dimensionality would then be expected to be bulk-like. This has been demonstrated in, for example, Ni films [59] which showed mean-field behaviour at thicknesses of ≈ 130 nm. The three dimensions in which magnetic excitations can exist lead to the efficient dissipation of

thermal energy within the system, and an ordering temperature which remains close to that of the bulk (deviating by only 5 K in this example). It is usually energetically beneficial for a large sample to split into locally ordered domains, which makes the realignment of the moments to an external field more energetically challenging, and is thus typified by a high coercive field. Regions within such a sample which are within a few atomic layers of the material interface only represent a negligibly small fraction of the total sample volume, and so the effect of interfaces can be ignored.

If the system is reduced in thickness to 1 nm or less, the comparatively high penetration depth of MOKE becomes unfavourable. The data collected will be affected by the substrate upon which the film is grown, which could impact the reliability of the results obtained. The expected behaviour is likely to show finite size effects, and deviate significantly from that of the bulk. As the spatial extent is reduced, the out-of-plane excitations are suppressed, as they must have shorter wavelengths to form, and a 2D magnetic lattice may form. In, for example, Gd [60], a crossover to 2D behaviour is observed below 15 ML. The influence of restricting the allowed magnetic excitations leads to a reduction in T_C as the magnetic lattice is less able to dissipate thermal energy. In this example a reduction of $\approx$ 50 K from that of the bulk is observed. Domain structures can form only in the in-plane direction [61]. In these reduced dimensionality systems, the effect of interfaces becomes critical. The fraction of atoms which are within a few atomic layers of the interface is high, and possibly 1. Interface effects such as induced moments and modifications of the ordering behavior must be considered. For studies where the specific behaviour of interfaces is paramount, a measurement technique with element selectivity (to resolve magnetic lattices from either side of an interface) and depth sensitivity (due to the spatial variation in the magnetic lattice) becomes critical.

If a spatial restriction is additionally applied in the in-plane direction, a patterned film can be created. The effect of interfaces must again be considered. If the patterned islands are below a critical size, magnetic domain formation becomes energetically unfavourable, and single domain elements are formed [62]. For a single domain element, the shape of the element will dictate its moment per unit volume because of the effects of stray fields [23]. Additional interaction mechanisms also exists in patterned media which describes the coupling between neighbouring islands [63]. The flexibility and tailorability of patterned magnetic media can potentially provide systems with a wealth of exploitable properties. Tailoring the shape and arrangement of islands can lead to a variety of artificially induced magnetic effects, such as frustration [64]. Measuring the magnetisation from a periodic array of elements can be achieved using MOKE, but the obtained signal is dominated by

the contribution of the substrate. Meaningful studies can still be performed [65–67]; however, the magnetic behaviour of the islands is potentially dominated by the effect of interfaces. If the effect of these interfaces is to be explored, element selectivity and depth sensitivity are again necessary.

The only applicable technique which provides the magnetic sensitivity required, while also providing element selectivity, is resonant x-ray scattering. This technique, supplemented with hard x-ray scattering and polarised neutron reflectivity (PNR), will therefore be the primary method of investigation throughout this work.

Chapter 3

Scattering

The work presented in this thesis investigates layered structures with parallel interfaces, with layer thicknesses in the Å and nm regimes. The scattering techniques employed to investigate these structures use beams of photons or neutrons to probe their structure and magnetic profile. To understand how this is achieved, the process of a wave interacting with matter must first be considered.

3.1 Introduction

A photon incident upon a material interface has a scattering behaviour which is dictated by the refractive indices (RIs) of the materials on each side of the interface. In optics, the RI of a material is assumed only to vary with the material density [57]. More strictly, the RI varies with the scattering cross-section which defines the likelihood of an interaction having occurred after a photon has penetrated a given distance into a target material. Photons with an energy significantly less than the rest mass energy of an electron can be assumed to scatter inelastically through Thompson scattering [68]. The *scattering factor*, $f(E)$, which described the cross-section can be described as the sum of energy dependent and independent terms such that [23]

$$f(E) = Z + f'(E) + if''(E), \tag{3.1}$$

where Z is the proton number and the energy dependent terms f' and f'' are dictated by the electronic configuration of the material. The real and imaginary part of the scattering factor are traditionally termed $f1$ and $f2$ such that

$$f1 = Z + f'(E) \quad \text{and} \quad f2 = if''(E). \tag{3.2}$$

The variation of this scattering cross-section translates into a variation of the refractive index, n, which must also be treated as complex quantity such that [23]

$$n(E) = 1 - \delta(E) + i\beta(E). \tag{3.3}$$

where δ describes the dispersion (or refraction) of the material, β described its absorption. δ and β are directly proportional to $f1$ and $f2$ respectively. The RI of a material then has a complex dependence on energy governed by its electron configuration. Away from an absorption edge, however, f' and f'' can both be assumed to be small and so δ, and thus n, only varies with Z which varies with the density.

An incident wave meeting a material interface will have some proportion of the wavefield reflected and some transmitted. In the simplest model, the reflected angle is fixed to the incident angle, θ_i, and the transmission angle, θ_t, is refracted in accordance with Snell's law [57],

$$\frac{sin\,(\theta_i)}{sin\,(\theta_t)} = \frac{n_1}{n_2}, \tag{3.4}$$

where n_1 and n_2 are the refractive indices (RIs) of the media before and after the interface respectively. The proportions of the incident wave which are transmitted and reflected are similarly described by the Fresnel equations [57],

$$r = \frac{n_1 cos\,(\theta_i) - n_2 cos\,(\theta_t)}{n_1 cos\,(\theta_i) + n_2 cos\,(\theta_t)} \quad \text{and} \quad t = \frac{2n_1 cos\,(\theta_i)}{n_1 cos\,(\theta_i) + n_2 cos\,(\theta_t)}. \tag{3.5}$$

These equations have slightly different forms depending on the orientation of the electric field with respect to the scattering plane, the examples given are for s-polarized photons. If a wave is incident onto a material with multiple layers, the transmitted signal from the first interface becomes the new incident wave onto the second interface. The reflected signal is then incident on the first interface again, and the transmitted onto the third, as shown in figure 3.1. This process continues indefinitely, with smaller intensities at each subsequent interface. Clearly, this is an iterative process; one which can be described using Parratt's recursive formalism, which will be described in more detail in section 4.2.1.

This description of the scattering assumes that the interfaces are perfectly parallel, and perfectly flat (i.e. have no roughness). Modern growth techniques can produce materials with interfaces which are essentially parallel, but can not eliminate roughness. The roughness is categorised by correlation lengths, i.e. the

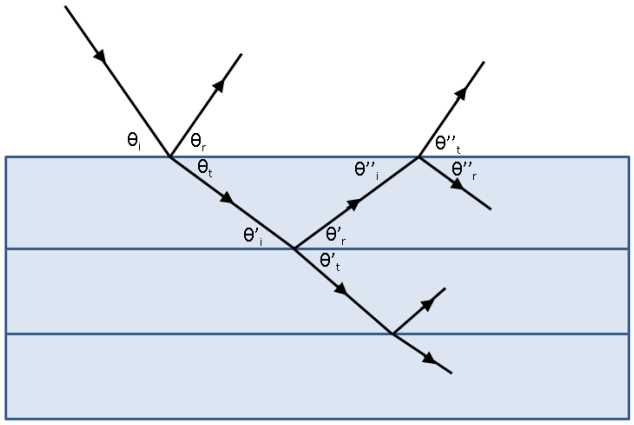

Figure 3.1: At each interface, the incident wave is split into transmitted and reflected waves in accordance with Snell's and Fresnel's laws. The incident, transmitted and reflected angles are denoted θ_i, θ_t and θ_r respectively.

distance scale over which the roughness structures repeat. In figure 3.2, short and long correlation length roughnesses are shown. A wave incident onto a rough surface is scattered through different angles by the various facets, denoted θ_F, of which the interface is comprised. If the angles of these facets are distributed in a Gaussian manner, with a standard deviation σ, the Fresnel equations then gain an additional exponential damping term which has the form [69]:

$$r = r^* exp(-q_z^2 \sigma^2) \tag{3.6}$$

where r^* is r for an ideal interface, and q_z is the out-of-plane component of reciprocal lattice vector (described later) which increases with the incident angle. This damping term causes the reflected intensity to fall more rapidly as a function of angle, with the degree of the intensity reduction increasing for rougher interfaces. For now, interfaces will be considered to be ideal, and roughness will be ignored. However, when dealing with data, the modification of the scattered intensity must be taken into account, which will be discussed in more detail in section 4.2.1.

For a perfect interface, if the incident angle is sufficiently low, total external reflection will prevent the transmission of the beam into the material. This can be predicted from the RI of the uppermost layer. For a simple estimate, it is convenient

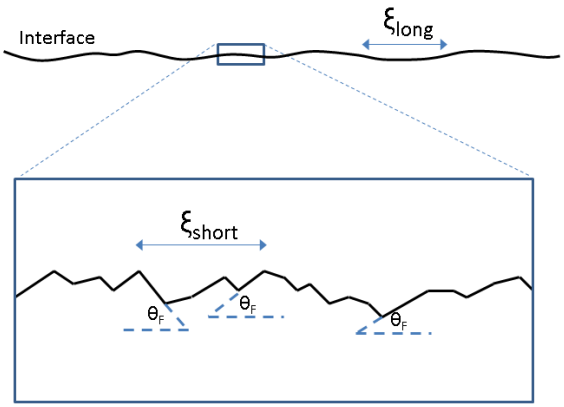

Figure 3.2: The roughness of a material interface can be defined by correlation lengths, ξ, on different scales, and on the smallest scale can be treated as facets. By approximating the distribution of facet orientations, θ_F, the impact of the roughness on the reflectivity can be calculated.

to ignore the absorption, leaving $n = 1 - \delta$. By applying Snell's law and the small angle approximation it follows that:

$$1 - \delta = cos(\theta_C) \approx 1 - \frac{\theta_C^2}{2} \tag{3.7}$$

where θ_C is the critical angle. This gives a critical angle which varies approximately as $\theta_C \approx \sqrt{2\delta}$. Critical angles in metals are typically below 1° [70]. Above this angle, if the reflected signal is measured from a layered material, at an angle (denoted 2θ) fixed to the incident angle, the resultant data will contain contributions from scattering events at every interface in the material. However, as the incident wave has a phase (which can reverse when scattered) some contributions will be constructive, and others destructive. This interference gives rise to periodic peaks in the reflected signal, as a function of incident angle, as the component of the wave-vector in the out-of-plane direction varies. If a repeat distance, in the out-of-plane direction is a whole number multiple of the out-of-plane component of the wave vector, then constructive interference will occur, and a peak in the reflected intensity will be observed.

Furthermore, the interference of the incident and reflected waves within the

material generates a standing wave perpendicular to the material interfaces. Changing the incident angle changes the component of the wavevector along this perpendicular direction, and so changes the periodicity of the standing wave nodes. Maxima in the scattering of the standing wave occur at the anti-node positions, and so careful choice of incident angle can tune the sensitivity of the probe to specific reciprocal space features. The exploitation of this technique is demonstrated in, for example, reference [71].

To relate these periodicities as a function of angle into periodicities as a function of distance within the sample so called *q transforms* are required. For elastic scattering the wavevector, $\mathbf{k}$, is preserved after a scattering event, and so $|\mathbf{k}_{in}| = |\mathbf{k}_{out}| = 2\pi/\lambda$. As illustrated in figure 3.3, the *reciprocal space* scattering vector, $\mathbf{q}$, is defined as $\mathbf{k}_{out}$ - $\mathbf{k}_{in}$ which, through simple geometry gives

$$\mathbf{q} = \frac{4\pi}{\lambda} sin\left(\frac{2\theta}{2}\right), \tag{3.8}$$

with q_x, q_y and q_z orthogonal components. This reciprocal space vector is so termed as repeat distances within the system are the inverse of real space separations.

This transform ignores the effects of refraction. If refraction were included, the changes in transmission direction and speed of light would change the components of the k vector within the material, as discussed in [72]. Ignoring the influence of refraction will adversely affect the reliability of layer thicknesses and RIs. As both of these parameters will be fitted in this work, and are not of key interest, the effect of refraction will be henceforth ignored for simplicity.

In this way, *reflectivity* data, i.e. the reflected intensity as a function of incident angle, represent the Fourier Transform of the real space structure. If the detection angle, 2θ, is not fixed to that of the incident angle, θ, then the additional periodicity of in-plane structures can also be studied. Resolving the scattering vector along the out-of-plane (q_z) and in-plane (q_x) directions then yields the $\mathbf{q}$ transforms

$$q_z = \frac{4\pi}{\lambda} sin\left(\frac{2\theta}{2}\right) cos\left(\alpha\right), \quad \text{and} \quad q_x = \frac{4\pi}{\lambda} sin\left(\frac{2\theta}{2}\right) sin\left(\alpha\right). \tag{3.9}$$

where $\alpha = (\theta - (2\theta/2))$. In the special case of the *specular condition*, 2θ is exactly twice θ and so $q_x = 0$ and the scattering is only sensitive to out-of-plane structures. A slice through reciprocal space in the q_x direction can be achieved by fixing 2θ and scanning θ (a "Theta Rock"). Although a small change in q_z is unavoidable during a scan of this type, it is typically negligible and can be ignored.

In order to quantify the desired real-space extents, the proportionality con-

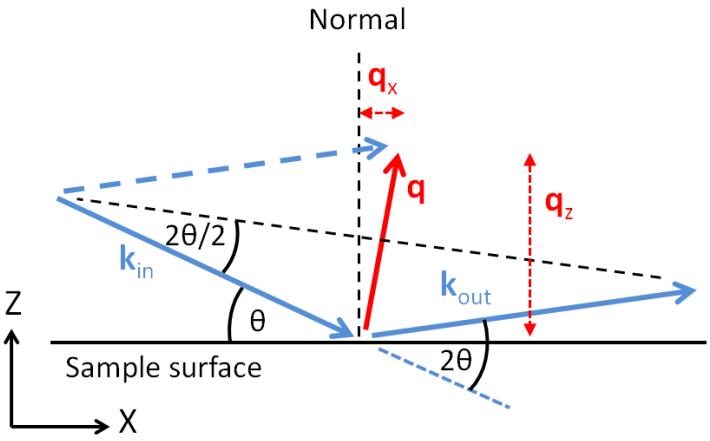

Figure 3.3: The wavevectors $\mathbf{k}_{in}$, at the incident angle θ, and $\mathbf{k}_{out}$, at the reflected angle 2θ, define the reciprocal lattice vector q with orthogonal components q_x and q_z. Note: θ does not have to equal half of 2θ.

stant between real and reciprocal space is required. Since $\mathbf{k} = 2\pi/\lambda$ it follows that

$$\Delta\mathbf{q} = 2\pi/\Delta\mathbf{d}, \tag{3.10}$$

where $\Delta\mathbf{q}$ is the reciprocal space repeat distance, and $\Delta\mathbf{d}$ is the real space separation (this is simply an alternative form of Bragg's Law where $n\lambda = 2\mathbf{d}sin\,(\theta)$).

The structure of a layered material can then be determined by exploiting the periodicities in reciprocal space observed within the scattered intensity when collected as a function of scattering angle.

3.1.1 Structure

Determining the magnetic profile within a material can not be achieved without first accurately characterising the structure. The structures studies in this work include simple alloys, crystallographic trilayers and multilayers of amorphous binary alloys. Multilayers comprise of several repeats of an identical stack (i.e. collection of 2 or more layers). Regardless of complexity, the structures all share the property that their interfaces are parallel. Structural categorisation in such materials is commonly achieved through reflectivity, which exploits the Bragg reflection [73] of, for example, an incident photon from the chemical interfaces within a material in a process

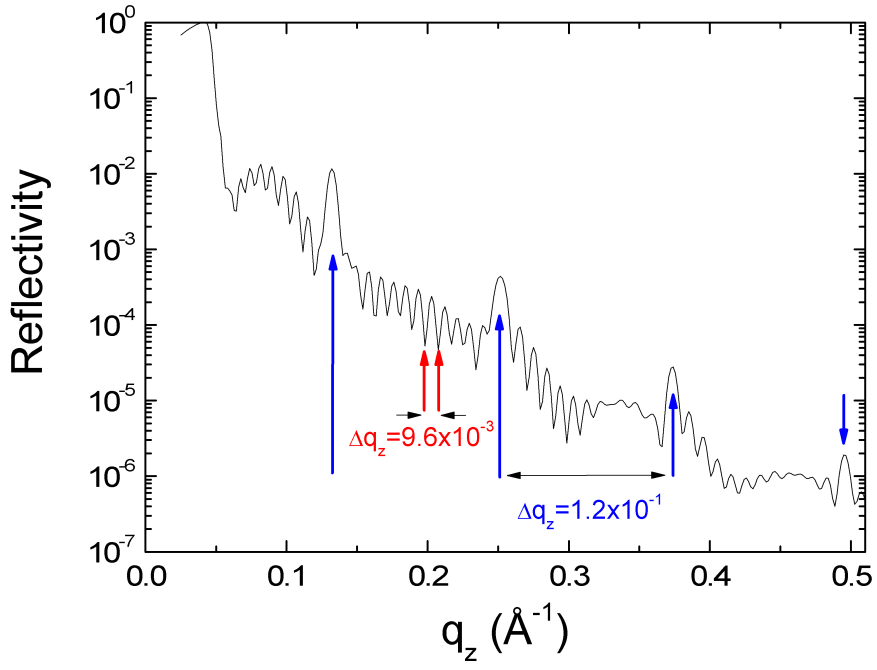

Figure 3.4: Hard x-ray reflectivity from a [$FeZr_{50\ Å}/CoZr_{5\ Å}$]$_{\times 10}$ multilayer with 50 Å AlZr seed and capping layers. Blue arrows indicate Bragg peak positions governed by the multilayer repeat distance and red arrows indicate total thickness fringes.

comparable to that of diffraction from crystallographic planes. The interference between the reflected photons from each interface, produces a total reflected signal that contains characteristic fringes. For a multilayer structure, the most prominent of these arise due to total sample thickness (Kiessig fringes) and the multilayer repeat distance (Bragg peaks). In a multilayer, each repeat of the stack amplifies the interference signal obtained. Characterising the structure in the out-of-plane, q_z, direction requires data to be collected in the specular condition.

Figure 3.4 shows the 7.11 keV specular x-ray reflectivity from a room temperature FeZr/CoZr multilayer. The reflectivity is defined as the scattered intensity as a fraction of the incident intensity. The indicated Bragg peak positions are separated by approximately 0.12 Å^{-1}. This corresponds, through the equation 3.10, to a real space separation of 52 Å, in approximate agreement with that expected. The Keissig fringes are separated by 9.6×10^{-3} Å^{-1} describing a total sample thickness of 654 Å, again in approximate agreement with that expected. Below the critical angle, corresponding to $q_z \approx 0.04$ Å^{-1}, total external reflection produces a reflected

intensity equal to the incident intensity, and is thus normalised to 1. Above this, absorption and interface roughness cause a drop in measured intensity. More detailed analysis of the sample structure, including quantification of the interface roughnesses and layer densities, requires data fitting, details of which will be described in section 4.2.1. This simple analysis, however, illustrates the effectiveness of reflectivity to determine out-of-plane structures; a technique which will form a core part of this work.

If these data were collected with an ideal point source, and ideal point detector, and a perfect sample, the reflected intensity below the critical angle would be strictly 1 and the intensity at very high angles would be limited by the background photons or neutrons within the experimental chamber. This is clearly not achievable. Both the source and the detector have a finite size, with the beam illuminating a finite area of the sample surface called the *beam footprint*. With any sample imperfections, such an interface roughness, diffuse scattering will occur, i.e. scattering at an angle not equal to the incident angle. Though the detailed nature of diffuse scattering is beyond the scope of this work, its impact on the specular scattering must be considered. The finite size of the beam footprint coupled with the finite size of the detector means that diffuse scatterers can be detected when in the specular condition. To counter this, there are two techniques available. The first and most accurate method is to collect so called *off-specular* scattering data. This involves setting a small offset between incident and detector angles, to remove the specular scatterers from the detected signal, and repeating the reflectivity measurement. These data then approximate the additional diffuse scattering within the specular reflectivity data and so can be subtracted. This method doubles the experimental time to collect each data set, which is sometimes impractical. In lieu of these data, a constant background can be subtracted from the data during the fitting process. This latter method is inaccurate, as the off-specular data will vary as a function of the reflected intensity, but can be employed when experimental time is limited.

3.2 X-rays

Reflectivity studies are clearly strongly related to the RIs of the material layers. The further apart the RIs of adjacent layers, the greater the proportion of scatterers which are reflected from the interface between them, and the greater the angle of refraction of the transmitted beam. Such an interface is said to have high contrast. Conversely, if the RIs are sufficiently close together, the incident wave is completely transmitted, with no change in direction, and the interface is said to have low

contrast. Adjacent layers with low contrast can not be resolved using reflectivity methods. For optical photons, the RI is chiefly determined by the material density [57]. If the incident wavelength is in the shorter wavelength x-ray regime, then a significant additional contribution to the RI can arise due to the excitation of electrons within the material when tuned to an absorption edge; this is the basis of resonant scattering studies.

3.2.1 Resonant Scattering

Earlier, the energy dependence of the RI was ignored. However, photons at the lower energy end of the x-ray spectrum, i.e. 200 eV to 10 keV, have energies of the same order as the electron transition energies of a broad selection of the periodic table. These transition energies represent the energy difference between electron bands. This excitation process constitutes a significant increase in the scattering cross-section of the material for x-rays of particular energies and is greatest near to the energy required to excite an electron from one shell to another; an *absorption edge*.

Close to an absorption edge the scattering factors, $f1$ and $f2$ (see equations 3.1 and 3.2), can change dramatically. An example of the change in scattering factors across the Fe L_3, at 706.3 eV, is shown in figure 3.5. At the absorption edge, there is a step change in $f2$, the absorption term. At the same time, there is a large dip in the dispersion term, $f1$.

This large change in the RI provides a useful route for enhancing the available contrast through choosing a photon wavelength to be close to a resonance energy within one of the materials. This is particularly appealing when investigating structures composed of the magnetic transition metals, which have very similar proton numbers. This is demonstrated in the upper panels of figure 3.6 which shows a simulation of the reflectivity of a $[Fe_{50\ \text{Å}}Co_{5\ \text{Å}}]_{\times 10}$ multilayer on a Si substrate at both 10 keV and 708 eV. Each interface was simulated with a roughness of 3 Å which is a realistic value while remaining low enough to provide clear fringes. The change in scattering length density (SLD), a value comparable to the scattering cross-section, from that of the Co layer is included in the lower panels, though it should be noted that the SLD of the Co layer also changes as a function of energy.

The difference in SLD between the Co and Fe within the 10 keV simulation is minimal. This is an energy which is far from the absorption edges of either material. The reflectivity simulation correspondingly shows very little contrast. The high frequency oscillations are Kiessig fringes correspond to the total sample thickness. The Bragg peaks corresponding to the bilayer repeat distance, which occur at every

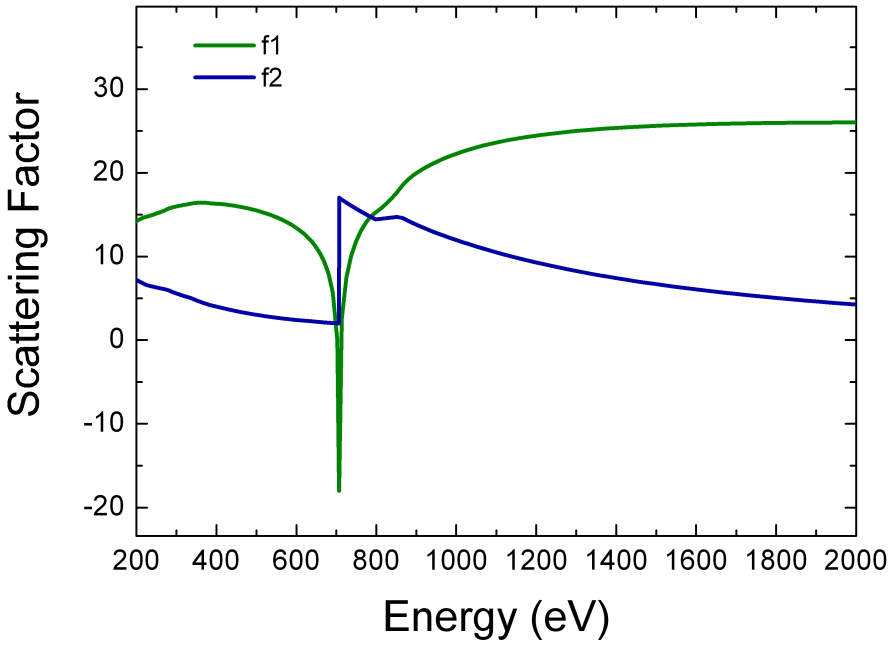

Figure 3.5: The change in the real and imaginary contributions to the total scattering, $f1$ and $f2$ respectively, across the Fe L_3 edge. The data are taken from [74].

10^{th} Kiessig fringe due to the number of repeats in the sample stack, are difficult to discern. Conversely, at 708 eV, an energy close to the L_3 absorption edge of Fe, a significant enhancement of the Bragg peaks is seen due to the enhanced contrast in the SLD. It is also useful to note that the location of the reciprocal space features is fixed irrespective of the incident energy, though experimentally, the angular range over which data would need to be collected to replicate this simulation would differ significantly.

Resonant reflectivity is clearly a powerful tool for investigating the structure of periodically adjacent materials. To extend this technique to include magnetic sensitivity, which is imperative for this work, requires the exploitation of the photon polarisation and its interaction with the material.

3.2.2 Magnetic Scattering

Circularly polarised photons, when close to an appropriate absorption edge, have a subtly different energy dependence depending on their helicity. This is because of

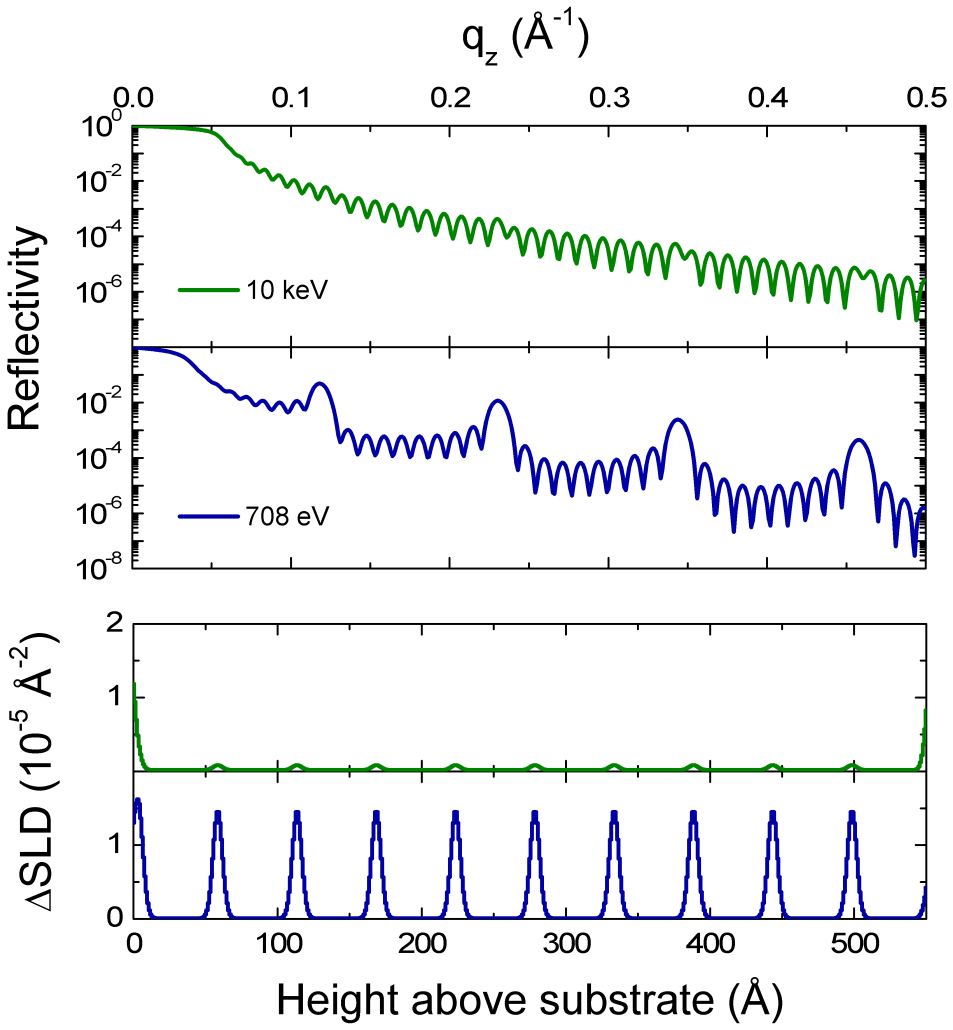

Figure 3.6: Simulations of an $[Fe_{50\ Å}Co_{5\ Å}]_{\times 10}$ multilayer on a Si substrate at both 10 keV and 708 eV. The contrast between the periodically adjacent materials is greatly enhanced at the Fe L_3 absorption edge (lower panels) manifested as an enhancement of the Bragg Peak amplitude (upper panels).

the angular momentum carried by the polarised photon, which has a spin component of $\pm\hbar$ parallel to the beam propagation direction.

The effect of a polarised photon interacting with matter is illustrated in figure 3.7. When a photon interacts with matter, it can be absorbed by an electron, raising the electron to a higher energy orbital. As momentum must be conserved during this process, the electron momentum must change from the initial to the final state. Selection rules exist [23] which describe the allowed changes in angular momentum during such a transition. One such rule dictates that only the orbital

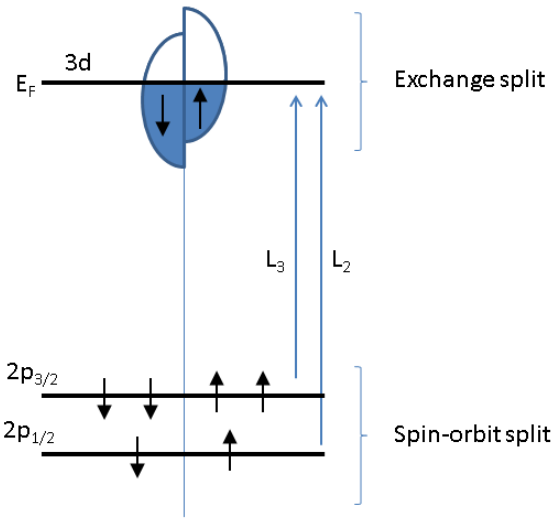

Figure 3.7: Circularly polarised resonant photons are used to excite spin polarised photoelectrons from the spin-orbit split 2p states to the exchange split 3d state. The 3d state acts as a spin filter producing a change in scattering cross-section between the left and right circularly polarised photons. This enables magnetic sensitivity.

angular momentum (and thus total angular momentum) can change, and the spin angular momentum must be conserved. In the 2p orbital, however, spin-orbit coupling splits the band into two sub-bands with different angular momenta: $J = L \pm S$. As the orbital quantum number, L and the spin quantum number, S, in the 2p band are 1 and 1/2 respectively, this produces two sub-bands with $J = 3/2$ and $J = 1/2$ (denoted $2p_{3/2}$ and $2p_{1/2}$). As a polarised photon excites an electron from one of these spin-orbit split bands, the spin-orbit coupling allows the spin angular momentum of the photon to be transfered to either the spin or orbital angular momenta of the electron. This transfer means that as the electron is excited, its spin angular momentum will be aligned to that of the incident photon, producing spin-polarised photoelectrons. A reversal of the photon polarisation then reverses the photoelecton polarisation.

The d band of a magnetic transition metal is exchange split, as described in section 2.1.1, and so if the photon energy is tuned to excite electrons from a core to a valence state (L edge - 2p to 3d, in 3d transition metals), a difference in transition probability will exist between the two photoelectron polarisations. This is because the exchange split band has a population imbalance between the two electron spin-states and therefore acts as a spin-filter for the excited electrons. This constitutes a change in the scattering cross-section between the two helicities which is proportional

to the d-band splitting, and thus proportional to the nett magnetisation.

The rate of absorption of polarised, resonant photons in transmission through a magnetic material is then a function of the filled electron states in the valence band. This allows the spin and orbital moments of this band to be quantified through the use of x-ray magnetic circular dichroism (XMCD); the process of measuring the absorption profile across the L_2 and L_3 absorption edges via total electron yield [75]. This is achieved by measuring, as a function of energy, the current at the sample surface generated by exciting electrons into the conduction band of the target layer using circularly polarised resonant photons. The measurement is performed with a high incident angle which is altered dynamically to remain at a fixed q position as the energy varies.

The magnetic sum rules [76–78] can then directly yield the spin and orbital contributions to the magnetic moment per atom at that fixed q vector. The first of these is the charge sum rule, which, after assuming an isotropic charge distribution is defined as:

$$I_{L_3} + I_{L_2} = C.N_h, \tag{3.11}$$

where I_{L_2/L_3} represents the integral of the XMCD spectrum across the L_2/L_3 edge respectively, N_h is the number of d-band holes and C is a proportionality constant. If the difference in intensity between the two polarisation channels is instead considered, the integral of the difference across the L_3 edge is commonly denoted A, and the integral of the difference across both the L_3 and L_2 edges is denoted B. These parameters can then be used to describe the spin and orbital moments, again assuming an isotropic charge distribution, through the relations:

$$-[A + 2B] = \frac{C}{\mu B} m_s \quad and \quad -[A + B] = \frac{3C}{2\mu B} m_o, \tag{3.12}$$

where m_s and m_o are the spin and orbital moments respectively. This is, in principle, a simple measurement to directly determine the strength of the moments within the system. In practice, however, for systems of the types studied in this work, it is not.

The signal strength acquired using XMCD is directly proportional to the amount of magnetic material present, and, due to the diffusion of electrons through matter, diminishes rapidly with the distance of the magnetic layer from the sample surface. The samples studied in this work primarily consist of buried magnetic layers with thicknesses of only a few monolayers, making XMCD unfavourable. Furthermore, the variable magnetic profile expected, due to the decay profile of induced moments, makes a fixed q vector technique unsuitable. Neutron scattering will

instead be used to quantify the magnetic moments, described in section 4.1.2.

In many cases, however, the quantification of the moments is not necessary and a measurement proportional to the total moment is sufficient. If so, x-ray resonant magnetic scattering (XRMS) can be employed [79]. This exploits the simpler relation, discussed earlier, that a difference in excitation probability exists between left and right hand circularly polarised light which is proportional to the total moment of the d-band. The magnetisation within the sample then provides a difference in scattering cross-section between the two polarisations, which produces a change in the reflected intensity in a reflectivity measurement.

If the earlier FeCo example is again considered, but this time each Fe atom is assumed to have a moment, the difference in reflectivity between left and right circularly polarised light can be demonstrated. However, as exploited in XMCD, the difference in scattering cross-section between left (-Pc) and right (+Pc) circularly polarised light depends critically on the electron configuration of the material and the incident photon energy. In the simulation programme used, which will be described in more detail in section 4.2.1, the difference in both $f1$ and $f2$ between the polarisation states can be controlled. Setting these differences both to 10% of the total cross section allows the splitting effect to be demonstrated, as shown in the upper panel of figure 3.8, with all other parameters consistent with the resonant example shown earlier in this chapter.

As the effect of the splitting between the two helicities is subtle, a clearer representation is to use the flipping ratio (F.R.), demonstrated in the lower panel of figure 3.8. This is percentage difference in reflected intensity between the spin channels, and is thus defined as

$$\text{F.R.} = \frac{(I^+) - (I^-)}{(I^+) + (I^-)}, \tag{3.13}$$

where I^+ and I^- are the reflected intensities for +Pc and -Pc respectively. The high frequency oscillations in the F.R. simulation are caused by the finite slicing of the structural interfaces, which will be discussed in section 4.2.1. The F.R. is usually presented along with the helicity averaged reflectivity, $((I^+) + (I^-))/2$, which contains only the structural contribution of the resonant scattering data.

It is useful to note that a reversal of the moment direction (i.e. the applied field direction), with a fixed photon helicity, will provide an identical difference in scattered intensity as flipping the helicity for a fixed field direction. This is because the population imbalance of the spin-split electron band is reversed when the applied field direction is reversed. It is not usually convenient to reverse the field direction

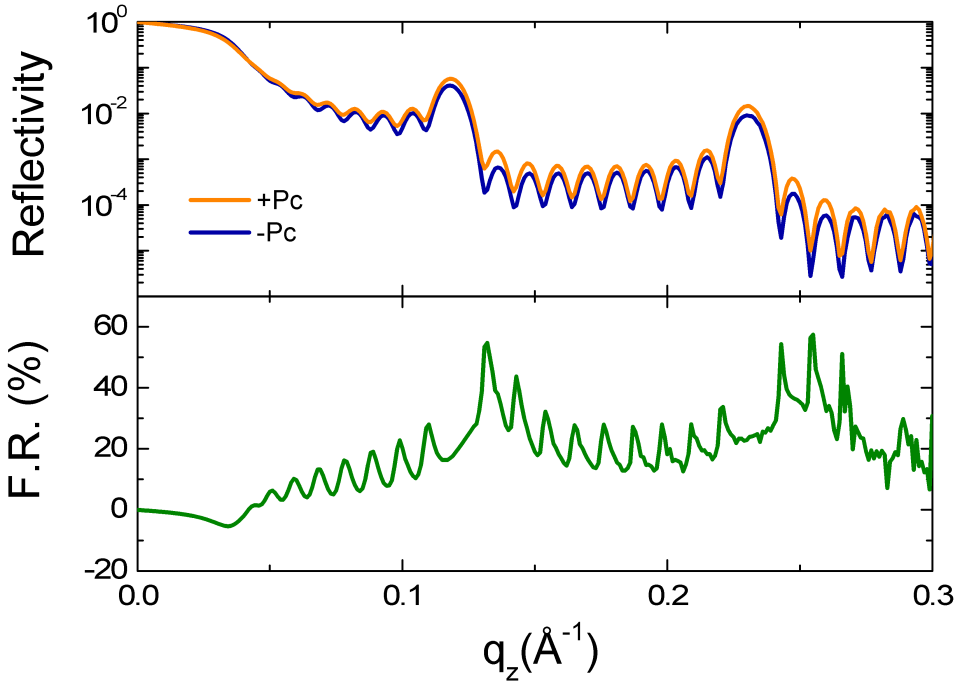

Figure 3.8: A simulation of a magnetic $[Fe_{50\ Å}Co_{5\ Å}]_{\times 10}$ multilayer on a Si substrate at 708 eV. The change in the electron excitation probability between left and right hand circularly polarised x-rays leads to a difference in refractive index and thus splitting in the reflectivity simulation (upper panel). The fractional difference between the helicities describes the magnetisation in the sample (lower panel).

for each datum. Instead, the reflectivity data for one field is collected before the field is reversed and the measurement repeated. Similarly, if the L_2, rather than L_3 were used, the apparent moment would reverse as the angular momentum of the incident photon couples oppositely to that of the electron as it lies in the opposite spin-orbit split band. However, the $2p_{1/2}$ band only contains two electrons, rather than four for the $2p_{3/2}$, making the L_3 the typical energy chosen. Data presented in later chapters are collected through helicity reversal, at the L_3 edge, unless otherwise stated.

Resonant x-ray scattering will be used to determine the distribution and relative magnitudes of elements specific moments within the magnetic lattice. As the photon spin angular momentum aligns parallel or anti-parallel to its propagation direction, only the component of the magnetic moments in the sample which lie in the scattering plane (shown in figure 3.9) can coincide with the photon angular momentum orientation. Only these components can then contribute to the magnetic

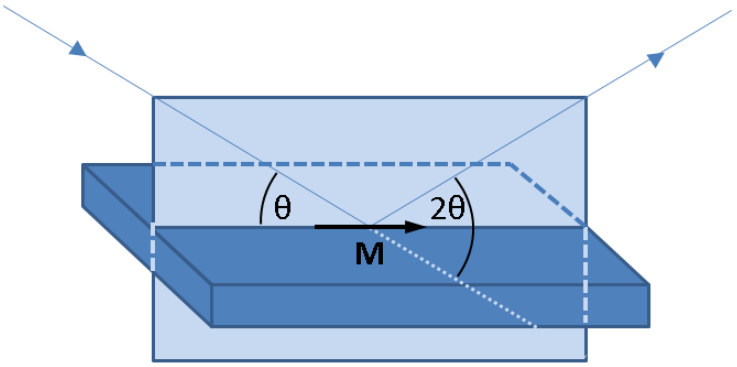

Figure 3.9: In a particular scattering condition, the scattering geometry used in XRMS studies only provides sensitivity to the component of the moment, at that q vector, which is parallel to both the sample and scattering planes, as described in the text. Furthermore, the measured moment is area averaged over the portion of the sample surface which is illuminated by the beam.

sensitivity of XRMS studies. However, components which lie in the out-of-plane direction will see equal and opposite magnetic sensitivity for the incoming and outgoing waves, and so have no nett effect on the scattering for a change in photon polarisation. This leaves sensitivity only to the moment in the in-plane direction which lies parallel to both the sample and scattering planes (as shown in figure 3.9). Furthermore, as the moment is area averaged over the beam footprint, XRMS has no sensitivity to anti-ferromagnetic alignment. Data will be collected using the methodology described in section 4.1.1.

3.3 Neutrons

High intensity beams of neutrons can be created for use as material probes which combine both nuclear and electronic scattering [80]. Neutrons can provide structural information via reflectivity through techniques analogous to those using x-rays [81]. The high penetration depth beams are ideally suited to studying multilayer materials, particularly heterostructures containing elements with similar proton numbers (or isotopes). This is because, unlike x-rays, the contrast between the scattering cross-sections of even periodically adjacent elements can be very high [82]. Neutrons also have the advantage that their magnetic sensitivity is proportional to the magnitude of the material moment, allowing quantitative analysis to be achieved directly [83–85]. Neutron sources, however, have low flux when compared to photon sources, and so a wide beam is often used. This allows greater beam divergence,

which can limit angular resolution. Additionally, the magnetic sensitivity is limited to the total moment at each q-vector meaning element specific magnetic sensitivity can not be achieved.

Incident neutrons can be scattered from a target material in one of two ways: from nuclei via the strong force, or electromagnetically via a dipole-dipole interaction between the internal field and the neutron magnetic moment [86]. The former is independent of incident neutron polarisation, whereas the latter has a scattering cross-section which is dependent on the relative orientations of the internal field and incident neutron dipoles. The scattering amplitude, as defined by Fermi's Golden Rule [87], is

$$\left(\frac{d\sigma}{d\Omega}\right) = \left|\left\langle \phi_1 \left(\boldsymbol{q}, \boldsymbol{\sigma}\right) \left| U_n + U_m \left(\boldsymbol{q}, \boldsymbol{\sigma}\right) \right| \phi_0 \left(\boldsymbol{q}, \boldsymbol{\sigma}\right) \right\rangle\right|^2, \tag{3.14}$$

where $\boldsymbol{\sigma}$ is the polarisation of the neutron and $\phi_{0,1}$ are the wavefunctions which, in the Born approximation, can simply be replaced by spherical waves. The nuclear and electromagnetic contributions to the scattering potential are described by U_n and $U_m \left(\boldsymbol{q}, \boldsymbol{\sigma}\right)$ respectively.

The neutron studies presented in this work are performed on laterally homogeneous materials. Therefore only the out-of-plane component of the scattering potential needs to be considered. Ignoring incoherent scattering, the potential is then described as

$$U\left(z\right) = U_n\left(z\right) + U_m\left(z\right) = \frac{\hbar^2}{2m} N\left(z\right) b\left(z\right) + \boldsymbol{B} \cdot \hat{s}, \tag{3.15}$$

where N is the number of nuclei per unit volume and b is the non-magnetic contribution to the neutron scattering length [88]. The magnetic contribution is the dot product of the internal field, $\boldsymbol{B}$, and the neutron spin operator, $\hat{s}$.

The simplest cases occur when the scattered incident neutron moment is parallel or antiparallel to the internal field. In the parallel case, the magnetic component provides an additive contribution to the scattered potential. Conversely, in the antiparallel case, a subtractive contribution of equal magnitude is observed. Non-collinear interactions add additional complications as the torque exerted by the cross product of the interacting dipoles seeks to reorient the neutron moment. This can be exploited to probe in-plane magnetic structures.

With the neutron polarisation collinear to the internal field direction, the potential simplifies to

$$U^{\pm} = \frac{\hbar^2}{2m} Nb \pm \mu \boldsymbol{B}, \tag{3.16}$$

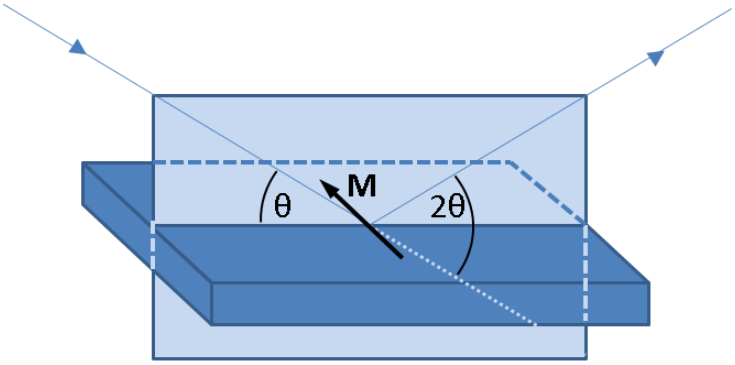

Figure 3.10: The scattering geometry in PNR provides sensitivity to moments collinear with the neutron polarisation direction. In this work, this direction is parallel to the sample surface and perpendicular to the scattering plane.

where μ is the neutron magnetic moment for neutron in the parallel (+) and antiparallel (−) orientations. The difference in scattered intensity between the parallel, I^+, and antiparallel, I^-, channels is proportional to the magnitude of the internal field of the material. The sum, $I^+ + I^-$, and flipping ratio, $(I^+ - I^-)/(I^+ + I^-)$, contain the structural and magnetic information respectively in a format analogous to that of XRMS. The "flipping ratio" is conventionally termed the "asymmetry ratio" in neutron scattering studies to avoid confusion when considering spin-flip events. As this work ignores the additional effect of spin-flip scattering, this unconventional notation will be used to parallel that of the x-ray studies.

Polarised neutron reflectivity (PNR) is sensitive only to the in-plane sample moments. In this work, the applied field direction and sample magnetisation direction are collinear; both are in the sample plane, perpendicular to the beam propagation direction and parallel to the beam polarisation direction. If present, magnetic components in the in-plane direction perpendicular to the applied field direction would lead to spin-flip scattering events, which could be resolved through polarisation analysis of the reflected beam. However, to maximise the available flux, such analysis was not performed and sensitivity to these components was lost. Therefore, the PNR studies presented in this thesis are sensitive only to moments in the direction which is parallel to the sample surface and perpendicular to the scattering plane, illustrated in figure 3.10. As with XRMS, PNR, at a particular q vector, is sensitive only to the moment averaged over the beam footprint. As such, the studies presented in this work have no sensitivity to in-plane antiferromagnetism.

Chapter 4

Experimental Details

4.1 Data Collection

4.1.1 X-ray Reflectivity

The element specific magnetic sensitivity of x-rays arises through careful selection of its energy and polarisation which relies on producing high intensity, polarised, monochromated x-rays. This is achieved using a synchrotron, where a flow of electrons is accelerated round an approximately circular ring, consisting of both straight and curved sections, by electromagnets [89]. As the charged electrons accelerate round the curved section of a bending magnet, bremsstrahlung radiation generates x-rays in a fan tangential to the beam. As the exact path of each electron takes differs slightly, an unmonochromated beam is produced. Monochromation is achieved through diffraction from a crystal, typically silicon, at a variable angle to the beam direction. Choice of angle dictates which wavelengths constructively scatter from the crystal, and so defines the energy. These crystals are often arranged in parallel pairs (as in figure 4.1) to ensure only a small change in beam height is incurred for a change in energy, rather than a change in beam direction. Such an arrangement is referred to as a "double bounce monochromator".

The straight sections of the synchrotron house insertion devices which oscillate the electron beam back and forth [89]. The bends in these *undulating magnets* produce unmonochromated x-rays which overlap and interfere, increasing the x-ray intensity with each undulation. These x-rays are then monochromated. The spacings between the evenly spaced undulations cause certain frequencies to constructively interfere, known as harmonics. These can be suppressed by detuning the undulator, i.e. by changing the spacings between successive undulations. Synchrotrons provide high intensity, highly coherent x-rays. This is particularly benefi-

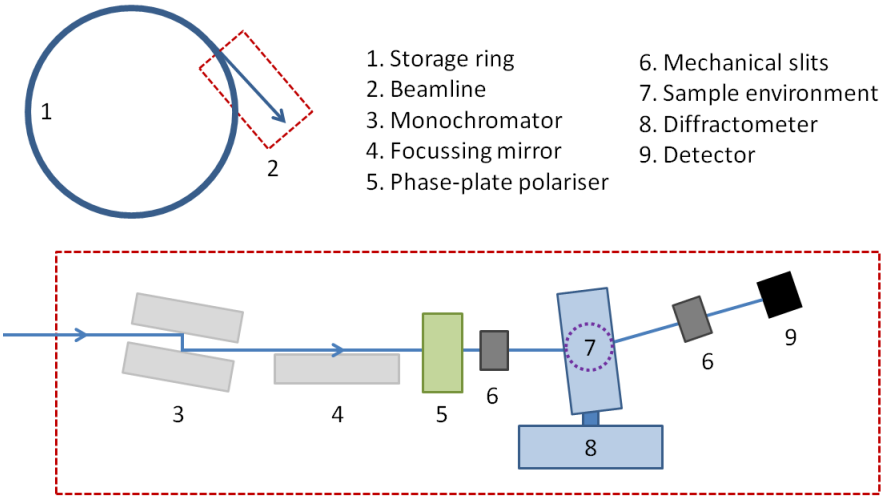

Figure 4.1: A simplified synchrotron beamline schematic. A highly coherent x-ray beam is tangentially emitted from the electron storage ring before being monochromated. A series of optical refinements then define the size and polarisation of the beam before it encounters the sample.

cial when examining the low scattered intensity interference from patterned arrays of islands, as the coherence of the beam allows many islands to be averaged over without destructive interference occurring. Synchrotron radiation, after monochromation, passes through a series of slits which define the beam shape. The beam size is a compromise between flux and resolution. Due to the differences in available flux, typical beam sizes are 800 x300 μm on a bending magnet beamline, and 50 x 50 μm on an undulator beamline. X-ray energies from synchrotron sources vary from approximately 200 eV to 10 keV. The resonant energies used in this work are the Fe, Co and Pd L_3 edges (706.3, 777.5 and 3174 eV respectively). At the exact resonant energy, the absorption peaks sharply (see section 3.2.1), leading to a pronounced reduction in scattered intensity. By tuning the x-ray energy to be approximately 0.5 - 1eV below the absorption edge, a better signal to noise is recorded when measuring the scattered signal. Henceforth, where transitions are referred to by name, for example "Fe edge", 0.5 - 1 eV below the L_3 edge should be inferred.

The necessary polarisation of a synchrotron x-ray beam can be achieved in several ways. Linearly polarised incident photons can be circularly polarised by transition through a phase plate [90]. These are typically made of diamond, though other materials such as silicon can be used for lower energies due to reduced absorption. These phase plates have different refractive indices for the σ and π components

of the transmitted photons. As the photons pass through the phase plate, a phase-shift between the components is observed. Optimisation of the phase-plate angle can then induce a quarter wave shift, producing circularly polarised light. An alternate method exploits the natural polarisation of the bremsstrahlung radiation. Above and below the beam axis, the radiation produced is positively and negatively circularly polarised respectively. In an undulator [91], the electron flight path is additionally oscillated perpendicularly to the undulation direction, using an electromagnet, creating a helical trajectory. The polarised, off-plane, component of the radiation is thus projected along the axis of this helix. Reversal of the electromagnetic field directions reverses the helicity of the electron trajectory, and thus reverses the polarisation direction; a reversal mechanism that allows high frequency polarisation switching. Both methods incur a significant reduction in flux with respect to the unpolarised beam, with the method constituting the lowest reduction depending critically on photon energy. Above approximately 3 keV, a phase-plate provides higher polarised flux, whereas at low energies, where absorption rates are high, an elliptically polarised undulator becomes advantageous. Experiments conducted in this work at the Pd edge (3.174 keV) were therefore performed using a phase plate polarisor, and those at the Fe and Co edges (706.3 and 777.5 eV respectively) using an elliptically polarised undulator.

The magnetic sensitivity and element selectivity of x-rays make them the ideal tool for probing the element specific magnetic ordering behaviour. This behaviour can be elucidated through the collection of magnetic hysteresis loops at discrete temperatures. The method employed for determining the changes in behaviour from the hysteresis loop response is discussed in section 4.2.3. Critical to these studies, however, is careful control of sample temperature. For the studies presented in this work, cooling power is provided by a He compressor for Pd edge studies and using a helium flow cryostat for Fe edge studies. The former method employs a pressure change of He gas to cool the sample environment; high pressure He gas is fed into the system, expanded and removed. The latter flows liquid helium through a tube in contact with the cold-finger upon which the sample is mounted. Both methods, in principle, allow access to temperatures down to 10 K, however, due to He flow restrictions, the Fe edge experiments were conducted at 30 K. The temperature in both cases is manipulated through proportional-integral-derivative (PID) control of a heating elements and either a Si diode or Pt resistor temperature sensor close to the sample position (see figure 4.2). The sample temperature can not, however, be assumed to be identical to that of the sensor. To ensure the closest correlation possible, the sample temperature must be allowed to stabilise for several

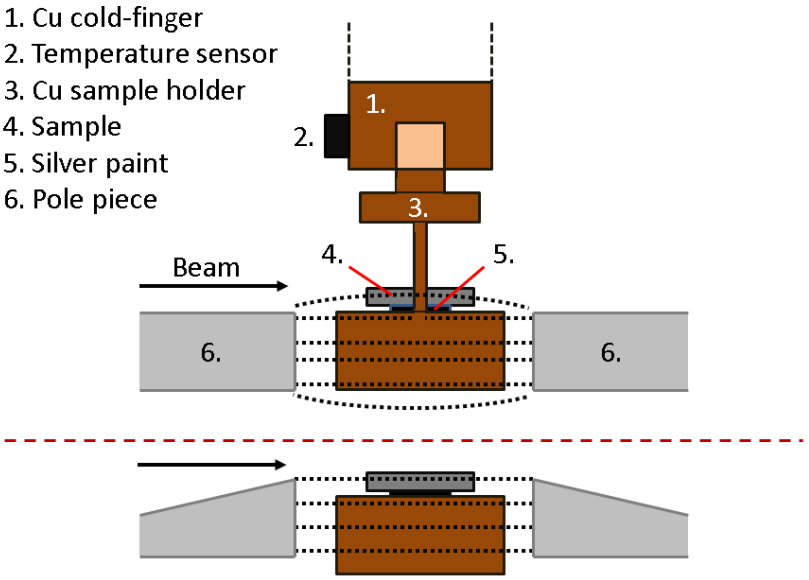

Figure 4.2: In vacuum sample environment schematics (not to scale) showing the two electromagnet pole piece configurations. Earlier work, conducted with square pole pieces (upper), suffered from inhomogeneous applied field strengths. Chamfered pole pieces (lower) allows a uniform field to be applied.

minutes per temperature step, with the exact waiting time dependent on the size of the step. An unavoidable thermal lag will still exist between the sample and cold-finger due to the material interfaces (sample/sample holder/cold-finger) between the sample and sensor, each of which will likely produce a small temperature gradient. Eliminating the effect of this is achieved by ensuring all desired temperatures are approached consistently, and therefore all temperature dependence data are collected as a function of *increasing* temperature. The absolute sample temperature therefore has a systematic uncertainty of ≈ 1 K, differing for each sample.

Conducting experiments at the Pd edge requires a novel approach to sample chamber design. Instruments designed for work at the Fe edge have no material in the beam from the storage ring to the sample, with the beam trajectory held under ultra-high vacuum (UHV). At higher energies, of several keV, the higher penetration depth of the photons [74] makes such measures unnecessary. Typically Be windows are used at intervals along the beam trajectory to separate the beam line into distinct sections at varying levels of vacuum, depending on requirements. This also helps to protect the storage ring in case of a vacuum failure. Samples are

often mounted in air for simplicity, or in a cryogenic sample environment which is separated from the beam flight tube by an air gap. These instruments are optimised to operate in a window of perhaps 5-10 keV. The Pd edge is at the lowest end of what beamlines designed in this way can achieve, and in fact is beyond the capability of most facilities. The absorption of Be in particular increases significantly as 3 keV is approached [74], and the additional air of lower vacuum environments or air gaps reduces the available flux at the sample to an unusable level. For the Pd edge studies undertaken in this work, an in vacuum sample chamber, named "Zebedee", was employed which eliminated any air gaps. The magnet system and cold-finger must all be mounted within this sample chamber, limiting space and restricting sample mobility. A schematic of the sample environment, showing the arrangement of the magnetic pole pieces with respect to the sample, is shown in figure 4.2. Ideally, the sample would sit exactly between the centres of the pole pieces. Required access to low angle scattering data makes this impossible. The best achievable compromise is to mount the sample flush with the tops of the pole pieces. However, making the sample surface exactly parallel to both the pole pieces and incident beam can not reasonably be achieved when mounted. The sample orientation must be altered after mounting, with the use of the x-ray beam, to ensure it is flat. However, as the magnet pole pieces are contained within the vacuum system, their orientation is fixed to that of the sample. This invariably produces a small offset between the beam direction and pole piece orientations, causing the pole pieces to clip the grazing incidence beam. The only practical solution is to mount the sample proud of the pole pieces, as shown in the upper portion of figure 4.2, where the applied field is inhomogeneous. To reduce the effect of magnetic clipping, later work was carried out using chamfered pole pieces, allowing the sample to be mounted in a more homogeneous field (lower portion figure 4.2). The affect of any field inhomogeneity is to systematically increase the effective ordering exponent, β_{eff}. The effect should, however, be small enough to prevent adverse impact on the data quality. Fe edge data were collected using an alternate sample environment which comprised a larger UHV sample chamber housing magnetic pole pieces, each with a slot cut through the centre. This allowed the sample to be mounted in a position where a homogeneous field is expected.

4.1.2 Neutron Reflectivity

Neutron beams can be generated either through fission or spallation. In a nuclear reactor, fission generates neutrons. In spallation, a target is bombarded with high energy protons releasing neutrons [92]. A reactor source produces the highest in-

tensity of neutrons. These neutrons, as they exit the reactor core, must be slowed down, through inelastic collisions, to increase their wavelength to one comparable to interatomic spacings, approximately 1 Å, corresponding to a neutron temperature of approximately 300 K. These neutrons, moving at a velocity comparable to that of room temperature air molecules, are known as thermal neutrons and are created by passing the neutron beam through a moderator. The neutrons then have a Maxwellian distribution of wavelengths from which the desired wavelength can be selected using a monochromator. Often this simply comprises of a rotating steel disc with a curved slot cut through. Only neutrons traveling at the desired velocity will be able to safely pass through this slot; the remainder are absorbed by the disc. Alternatively, Bragg reflection from a monochromating crystal can be used, akin to the technique used in synchrotron studies. This monochromated beam can then be used in reflectivity studies using a scattering geometry akin to that of x-ray scattering.

Spallation sources produce neutrons through collisions between high energy protons and stationary target nuclei [92]. In the spallation source at the ISIS facility, H^- ions are first accelerated in a linear accelerator, before being stripped of their electrons and injected into a small synchrotron. The protons continue accelerating within the synchrotron, where they accumulate into bunches. These bunches are ejected from the synchrotron and impact a Tungsten target, producing neutrons. Maximising the potential of the incident flux is achieved by utilising the whole energy spectrum through operation in Time Of Flight (TOF) mode. A pulse containing neutrons with different energies will probe a sample, when incident at a fixed angle, with different q vectors. These neutrons will also travel at different velocities, resolvable by recording the time of detection with respect to the generation time of the pulse: the TOF. As such, rather than collecting reflectivity data with a fixed energy and varying incident angle, a fixed angle and varying incident wavelength can be exploited. Spallation sources will be used exclusively in this work.

Magnetic contrast can be obtained through the use of a polarised incident neutron beam. To achieve polarisation, the neutrons, with angular momentum of $\pm\hbar/2$, can be reflected off a polarising supermirror. This is a magnetic multilayer in which the layer thicknesses diminish with increasing depth. The diminishing layer thicknesses allow constructive scattering from the multilayer over a wide range of incident wavelengths. This effectively increases the critical angle for total external reflection. As the multilayer is magnetic, the effective change in refractive index due to the difference in scattering cross-section observed between the two incident spin-polarisations leads to an offset in critical angles. Aligning the mirror such that the

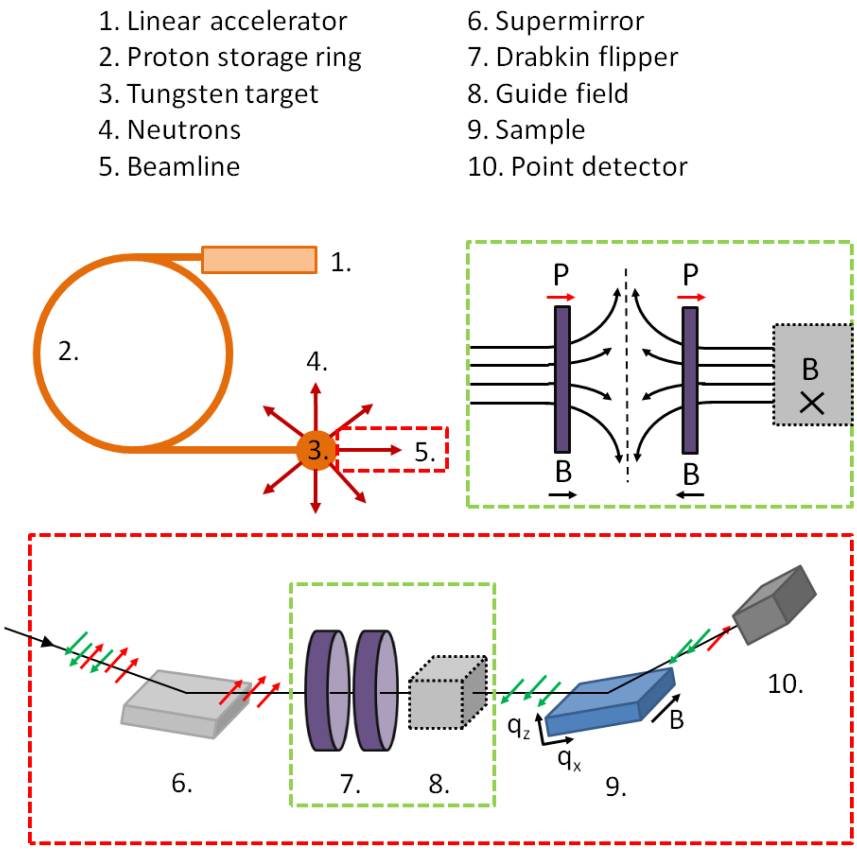

Figure 4.3: Schematic of a spallation neutron source and beamline. The linear accelerator injects protons into the storage ring before collision with a tungsten target producing radially scattered neutrons. The neutron beam is then chopped into packets before entering the beamline, where time of flight can be employed to gain q_z resolution.

angle of incidence is between these angles allows one polarisation (typically neutrons with angular momentum $\hbar/2$) to be reflected while the other is transmitted. This creates a fully polarised beam at the cost of halving the beam intensity.

To create a useful probe, the polarised neutrons in the incident beam must be aligned parallel or anti-parallel to the sample field direction. On the CRISP instrument at the ISIS facility, where the neutron reflectivity data presented in this work were collected, this is achieved with a Drabkin Flipper [93]. This is comprised of two adjacent electromagnetic coils with applied field directions collinear with the beam direction (see figure 4.3). The first of these coils, the applied field direction of which is fixed, adiabatically rotates the incident neutron polarisation to be parallel

to the beam direction. The second coil, with a reversible field direction, can then operate in two states: flipping and non-flipping. In the simplest, non-flipping case, the applied field direction of this coil is identical to that of the first coil, producing no additional affect. The polarised neutrons then enter a guide field, with an applied field direction parallel to that at the sample surface, which adiabatically reorientates the neutrons into a final state parallel to this field direction. If the second coil field is reversed, an adiabatic transition occurs at the point equidistant between the two coils. The polarisation direction is then preserved in the lab frame, but has reversed with respect to the applied field. As the neutrons subsequently enter the guide field, the adiabatic reorientation causes an antiparallel alignment of the neutron polarisation to the applied field direction; the polarisation has been flipped. Polarised neutron sources can then be exploited using experimental techniques and scattering geometries analogous to those performed using resonant x-rays.

As the scattered intensity, and thus statistical significance, is rapidly lost with increasing q, reflectivity data were collected at several incident angles while maintaining the specular condition. The instrument slits were modified at each angle to maintain a fixed Δq_z resolution of 4 %. Data from each angle are then combined to form the final reflectivity data set. The combination of data with different statistical significance, and the continuous distribution of neutron wavelengths in the TOF mode, producing data at continuous, rather than discrete, q values, necessitates data rebinning. This was performed as a post-processing technique with the width of the bins determined manually as a compromise between data uncertainty and point density. The reflected neutrons were detected with a point ^{3}He detector. Typical acquisition times were of the order of 20 hours for a specular measurement out to 0.25 Å^{-1} in q_z. However, as the samples are stored and transported in air, no modification to the sample structure is expected during the experiment. All PNR experiments were performed at 10 K using a helium flow cryostat.

After collection, data from either polarised neutron or resonant x-ray scattering must be processed in order to yield useful information about the structural and magnet composition of the samples and the magnetic interactions present. These are achieved through the fitting of specular reflectivity and hysteresis loops as a function of temperature respectively.

4.2 Data Processing

4.2.1 Reflectivity Simulations

The fitting of specular reflectivity data provides the structural and magnetic profiles in the out-of-plane (q_z) direction. Fitting is achieved by simulating a sample structure and calculating the reflectivity expected. The sample structure is then modified to minimise the difference between the simulated and experimentally observed reflectivity. For the simulation and fitting of data, the freely available GenX software was used [94] which can model both x-ray and neutron data.

To produce a simulation to the data, three basic parameters are needed: the thicknesses, refractive indices (RIs) and roughnesses of each layer. The thicknesses can be assumed to be approximately known from the growth procedures. The RIs can be calculated from the scattering cross-sections. For both neutrons and photons, tabulated values for the scattering terms of each chemical element are readily available [74]. For neutron scattering studies, these values are appropriate, whereas in x-ray studies, they are only appropriate when sufficiently far from an absorption edge. An example of the available atomic scattering factors for Pd, across the L_3 edge, are shown in figure 4.4. As a photon energy approaches a layer resonance, the poor energy resolution of the available atomic scattering data can dramatically affect the RI and thus makes the tabulated values unsuitable.

GenX allows $f1$ and $f2$ to be fitted, and thus the RI modified, for each layer. Within GenX, $f1$ and $f2$ are composed of different contributions from resonant and magnetic scattering. Each layer starts with $f1$ and $f2$ from the Henke tables [74] which both then have fittable correction terms added. This modification affects the RI of the layer identically for all incident polarisations, and allows resonant scattering data to be fitted without prior knowledge of the absorption profile. This technique, though powerful, must be used carefully. Changing the scattering terms is equivalent to modifying the density of the layer, and if used without caution, could lead to unphysical results. Where possible, it is therefore prudent to simultaneously fit resonant and non-resonant scattering data to ensure a robust simulation is obtained. Similarly, simultaneous fitting to PNR data could be employed to fit the structure of resonant scattering data; however, PNR lacks the high resolution of non-resonant x-ray studies.

An additional modification to the RI of each layer is made if the layer is magnetic. As described in section 3.2.2, a magnetic layer produces a difference in scattered intensity between left and right hand circularly polarised light. In GenX, this effect is simulated using a modification to the resonant scattering factors, which

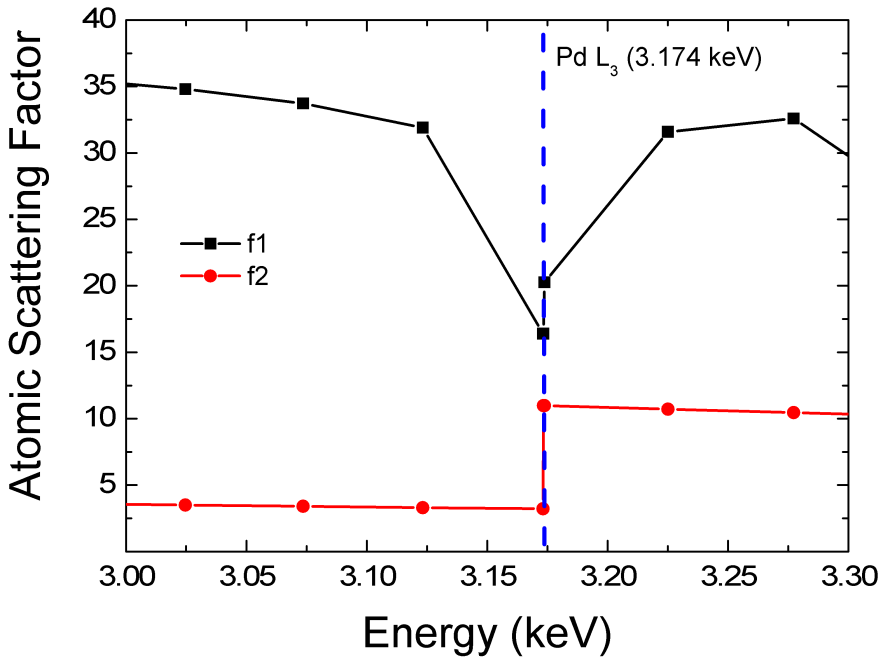

Figure 4.4: $f1$ and $f2$ respectively represent the real and imaginary parts of the atomic scattering factors of Pd from the Henke tables [74]. The low point density, and large variation makes these tabular values unsuitable for simulations to data collected near to an absorption edge. The atomic scattering factor is defined as the ratio between the amplitude scattered by an atom and a single electron.

is additive or subtractive depending on the polarisation. These modifications apply to both $f1$ and $f2$, producing four fittable resonant scattering terms in all. When discussing the simulations in later chapters, these four corrections will be referred to as the two *resonant scattering terms* and the two *magnetic scattering terms*. If the RIs are assumed to be known, the sample can be modeled and the structure can be determined from reflectivity data.

However, difficulties arise when trying to model imperfect interfaces. As discussed in section 3.1, interface roughness scatters the incident wave, and so intensity in the reflected and transmitted beams is lost. Predicting the effect of roughness on the reflectivity data can be achieved if the standard deviation of the orientation of the facets which comprise the interface is known. Clearly this is not realistically measurable. However, the large beam footprint in scattering studies, which illuminates an area much greater than the correlation length of the roughness, allows a rough interface to be modeled only by considering the spatially averaged RI as a

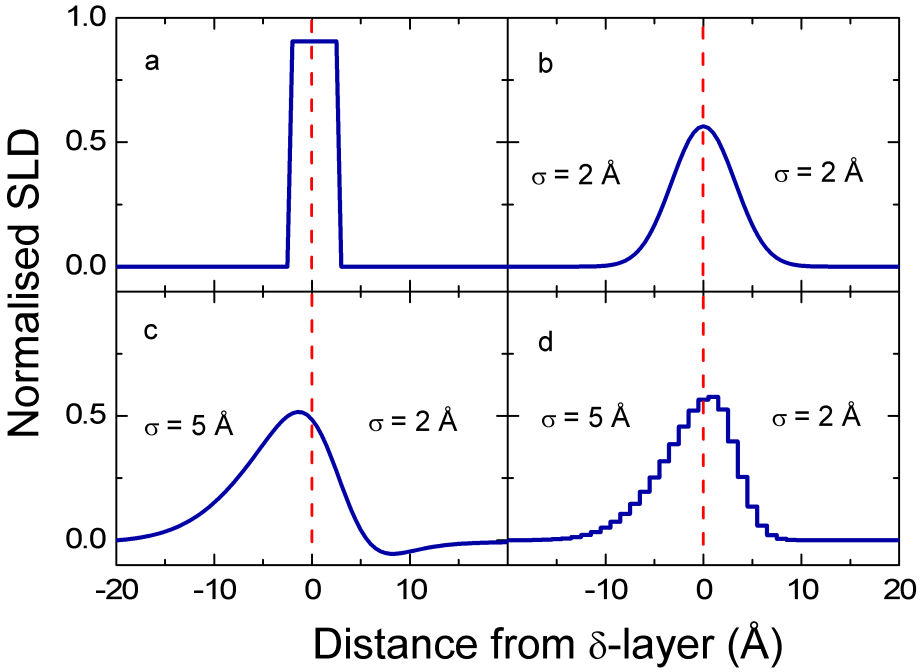

Figure 4.5: A simulated interface under different roughness models. The ideal interface (a) can be approximated with error function roughness (b). Where two Erf.s overlap, unphysical results can occur (c). Slicing the interface (d) prevents these unphysical results at the cost of greater computational intensity.

function of depth. A rough interface then becomes a smoothly varying transition between the RIs above and below the interface. The variation of this RI profile is defined by the distribution of the interface facets, i.e. that same sigma which defined the roughness profile in the facet model. This approximation is the basis for all interface roughness models, with the profile defined by an error function with a width defining the magnitude of the roughness. This is computationally fast as it has an analytical solution which can be integrated into Parratt's recursive formalism [95].

Problems with this technique arise as the layer thicknesses reduced to a level comparable to the magnitude of the roughness, as the error-function roughness profiles begin to overlap. This is demonstrated in figure 4.5. An ultra-thin layer (panel a), can be modeled with appropriate error-function roughness (panel b). However, if the roughnesses of the adjacent interfaces differ (which is inevitable to some degree), the overlapping functions cause unphysical results whereby the resultant RI extends beyond that of any of the constituent layers (panel c).

The solution is to remove the analytic roughness and split the interface into slices, with each slice acting as an alloy of the layers adjacent to the interface. If, for example, we consider a trilayer A/B/C comprised of layers with refractive indices a, b and c respectively, the RIs of the alloy slices at the AB interface will vary as $ax + b(1 - x)$, where x varies, between 0 and 1, with distance from the interface. Similarly, the RIs at the BC interface will vary as $bx' + c(1 - x')$. If B is sufficiently thin to cause the interfaces to overlap, the RI of slices across the AB interface will become $ax + (bx' + c(1 - x'))(1 - x)$, through substituting b for the alloy RI due to the BC interface. As x and x' are both constrained to be within 0 and 1, the RIs of the slices are always physical, producing an interface as illustrated in panel d of figure 4.5. As the width of the slices is reduced, the approximation to a smoothly varying profile is improved. However, this increases the computationally intensity of the simulation, particularly for multilayers with many buried interfaces. GenX allows the interfaces to be sliced, in this way, to any specified thickness.

In a recent study by Tonnerre et al. [96], soft X-ray magnetic reflectivity was used to investigate the magnetic distribution in Fe_xMn_{1-x} alloy films (2.4 nm with x = 0.7, 0.8) and Au/Fe(X ML)/Cu(001) thin films (with X = 4, 6, 8). Initially, reflectivity data was fitted to model the structural profile, after which the magnetic profile could be simulated, keeping the structure parameters constant. The magnetic distribution was modeled by splitting the alloy layer into a number of equal slabs, allowing only the magnitude and orientation of the moment to change in each. The optimum number of slabs to accurately model the data corresponded to a slab thickness of approximately 1 ML depending on the complexity of the system; further reduction in slab thickness resulted in no appreciable improvement. Though not implementing a slicing method at each stage in the process, this work provides a reasonable guide to the minimum effective slice depth. In the work presented in this thesis, a minimum slice depth of 1 ML will be used.

In this example, the magnetisation of the slices were treated separately with a moment and orientation which was allowed to change. In the work presented in this thesis, the magnetisation will always be aligned along a specific direction by an applied field, and the component of the magnetisation along that direction will be measured. As such, only the magnitude of the moment for each slice is required. However, as systems with induced moments will be studied, which can have polarised magnetic regions extending $\approx$ 1 nm from the structural interface, individually fitting the magnitude of the moment within each ML slice is inefficient. Instead, a function can be defined which describes the magnetic profile, from which the moment in each slice can be calculated. The magnetic contribution to the

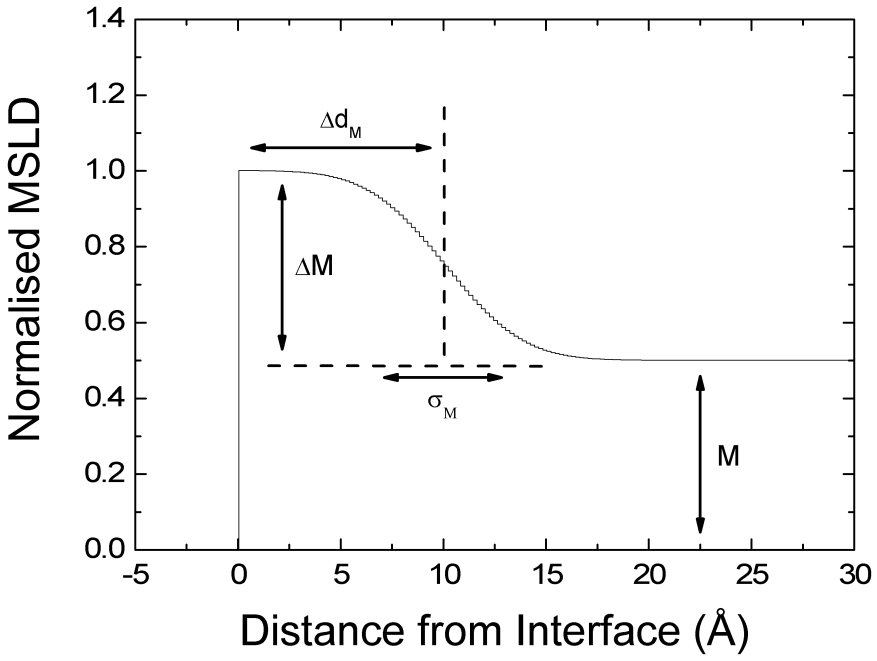

Figure 4.6: The magnetic scattering length density (MSLD) can be tailored at an interface when fitting reflectivity data using GenX [94]. The free parameters shown allow the magnetic interface profile to be accurately controlled.

total scattering can be considered separately to the structural contribution, with a separate *magnetic scattering length density* (MSLD) proportional to the magnetic moment. The function describing the MSLD is based on a few simple, fittable variables. The effect of these parameters on the MSLD are shown in figure 4.6.

The first of these interface parameters is the magnetisation of each material layer (M). This is set through the magnetic scattering terms and the layer moment. As these scattering terms are fitted, the magnitude of the moment is arbitrary without the simultaneous fitting of PNR data. As with the structural interface, there must be a step change in the MSLD associated with the interface between two materials. However, for an itinerant magnetic system, this step change is not necessarily centred exactly at the material interface, and will instead be governed by the electron spin diffusion lengths of the materials on either side of an interface (see figure 2.3). The offset of the magnetic interface with respect to the structural interface is the second parameter used to define the magnetic profile (Δd_M). The third parameter accounts for the effect of interface moments. Close to an interface, the truncation of the magnetic lattice has been shown to suppress or enhance the

measured moments [97]. Within GenX, this is simulated using a parameter which defines a multiplicative modification of the layer moment at the interface (ΔM). The fourth parameters describes the magnetic roughness across this magnetic interface (σ_M). This roughness is simulated using a slicing method identical to that of the structural interfaces.

These parameters can then define the magnetisation across an arbitrary number of slices. If the magnetisation exists on both sides of an interface, for example at a FM-FM interface, these parameters must be defined at each side of a magnetic interface and are included in addition to all structural parameters (e.g. interface roughness). This produces a large number of degrees of freedom, making the magnetic profile difficult to unambiguously determine. In multilayer structures, the magnetic profile is assumed to be identical for each similar interface throughout the sample stack. In trilayer films, with composition ABA, the profile above and below the central layer can be assumed to remain identical, or within a certain tolerance of each other. This reduces the number of degrees of freedom and helps to ensure a robust fit.

The difficulties presented by the high number of degrees of freedom in the fitting procedure are further complicated by the high correlation of parameters. Two pertinent examples in this work are the correlation of thickness and roughness in ultra-thin layers, and the correlation between layer thicknesses in a bilayer stack. To examine the correlation between thickness and roughness, the simulated interfaces shown in figure 4.5 can again be considered. If panel a is compared to panel c, it is clear that the addition of roughness has reduced the peak contract of the interface, while making it appear broader. However, as described in section 3.2.2, the contrast is strongly dependent on the incident photon energy and is fitted through the resonant scattering terms. Resolving a thicker layer with a lower roughness from a thinner layer with a higher roughness is then very difficult, leading to a high degree of correlation between the two parameters. To examine the correlation between layer thicknesses in a bilayer stack, the simulated reflectivity data in figure 3.6 can be considered. It is clear from these data that the Bragg Peak (BP) positions are dictated by the locations of the resonant material within the multilayer. These positions are dictated by the bilayer repeat distance, i.e. the sum of the Fe and Co layers in this example. This repeat distance is then typically well defined by reflectivity data. However, the thickness of the individual components of this repeat distance are much more poorly defined, with the two thicknesses highly correlated.

Defining the uncertainties of fitting parameters is clearly difficult. Typically, layer thicknesses can be considered to have uncertainties of approximately 5%. How-

ever, this uncertainty increases with decreasing layer thickness. As a rule-of-thumb, it is reasonable to consider all thicknesses to have an uncertainty of around 2 Å. Similarly, roughnesses have a typical uncertainty of approximately 10%, but they too can be considered to have a rule-of-thumb uncertainty of around 2 Å. In the following chapters, layer thicknesses and roughnesses will be provided to an accuracy of 0.1 Å. This is well below the realistic uncertainties, but is provided as a record of the fitting results.

The fitting of all reflectivity data presented in this thesis will be performed using GenX, with fitted structural and magnetic resonant scattering terms, where appropriate, and fixed material densities. Simultaneous fitting to hard x-ray data will be used, where available, to refine the structures.

4.2.2 Quantifying Moments

As the magnetic resonant scattering terms are fitting parameters within GenX, the magnitude of the magnetic moment cannot be quantified during fitting. There are, however, several alternative methods of available to quantify the magnetic moments within a system. One commonly used method during resonant scattering experiments is XMCD, described in section 3.2.2, which allows the spin and orbital moments to be measured directly. However, the samples studied in this work are comprised of buried magnetic layers with relatively low volumes of magnetic material. This reduces the available signal strength, making XMCD inappropriate for this work. An alternative is to use superconducting quantum interference device (SQUID) magnetometry. Squid magnetometry is a highly sensitive technique, but only allows the total moment to be measured. However, if the out-of-plane magnetic profile is known from reflectivity studies, and the in-plane sample extent is known, the total magnetic volume can be calculated. From this it is plausible to quantify the magnitude of the moments throughout the varying profile shape. However, one significant drawback to using SQUID magnetometry is the limited sample volume which can be accommodated. The samples used in this thesis are typically of the order of 1 cm $\times$ 1 cm $\times$ 1 mm, and a SQUID may typically only accommodate a tenth of this total volume. Collecting SQUID data then becomes a destructive test, as a piece of the sample is removed for analysis, which is highly undesirable. Nevertheless, as preliminary work to these studies, such measurements were attempted on an FePd trilayer sample similar to those studies in chapter 6. However, the data obtained were not of sufficient quality for meaningful analysis to take place. It was concluded that the significant levels of manual handling of the delicate samples throughout the cutting and mounting processes had compromised the integrity of

the sample. As the process is destructive, it was judged that no further attempts of this type would be made.

As described in sections 3.3 and 4.1.2, polarised neutron reflectivity can also be exploited to probe magnetism. As there are no fitted resonant scattering terms, this sensitivity can be exploited to extract the magnitude of the moments directly from fitted reflectivity data. However, in a manner similar to the strong correlation between thickness and roughness during fitting, there is also a strong correlation between the magnetic moment and magnetic roughness. An ultra-thin layer with a large magnetic moment, but a high roughness, is hard to differentiate from one with a smaller moment and lower roughness. The shapes of the profiles would differ subtly, but resolving the two would then require reflectivity data to substantially higher q-vectors than is typically achievable.

For this work, a quantitative measure the magnitude of the moments is of significantly less importance than the distribution of moments throughout the sample (i.e. the shape of the magnetic profile). If a quantitative description is not necessary, then x-ray magnetic scattering (XRMS) alone is sufficient to allow meaningful, qualitative comparisons between profiles, even with the magnetic scattering parameters being fitted. In instances where data at multiple energies are available, such as in section 6.2, the sensitivity to the total moment allowed by PNR can be exploited to ensure the adjacent sub-lattices, probed separately through XRMS, are correctly normalised to each other during fitting. Simultaneous fitting to complementary PNR data will therefore be employed where necessary, but no attempt to quantify the magnitude of the moments will be made.

4.2.3 Extracting Ordering Exponents

An accurate description of the magnetic ordering can be obtained through the collection of hysteresis loops at discrete temperatures. This has an advantage over a continuous measurement of the magnetisation while increasing the temperature as it eliminates domain effects. It does, however, allow fewer temperature values to be probed in a given time. Element specific hysteresis loops are collected using XRMS at a fixed scattering vector, chosen to produce the maximum F.R. at H_{sat}, by recording the measured F.R. as a function of applied field. The maximum F.R. is often at the point of lowest scattered intensity (see figure 3.8), causing the required counting times to increase. In order to reduce noise in the data, $M(H)$ can be fitted to

$$M(H) = A.arctan(\frac{H \pm H_c}{\nu}) + H.B + C, \tag{4.1}$$

where A,B,C, ν and H_c are all parameters to be fitted. With the exception of H_c, the values of the fitting parameters do not relate to physical properties and should be considered arbitrary. The shape parameter, ν, governs the roundness of the loop. The loop fit then comprises two arctan functions, one each for the increasing and decreasing field directions, which are identical except for a translation of $\pm H_c$. Furthermore, the invariance of the shape parameter with field forces the fit to have two-fold rotational symmetry. The true loop shape often differs subtly from this simplification. As the parameter of interest, the remanent magnetisation, is unlikely to be affected by this difference, the simplification is justified. Similarly, B, the gradient at H_{sat}, should be zero if the sample is truly fully saturated. As some additional paramagnetic response may remain, it is fitted to prevent any adverse influence of this discrepancy on the remanent moment. Furthermore, B is allowed to differ between temperatures, again ensuring the best possible fit to the remanent moment.

The fitted hysteresis loops allows the both the moment and susceptibility as a function of field to be extracted. The susceptibility, $\chi = dM/dH$, can be calculated directly from equation 4.1 yielding:

$$\chi(H) = \frac{A}{\nu\left(1 + \left(\frac{(H \pm H_C)}{\nu}\right)^2\right)} + B. \tag{4.2}$$

The susceptibility is again optimised around the zero-field region due to the fitting compromises faced by equation 4.1. Analysis of the moment and susceptibility as a function of field allows the information contained within the shape of the loop to be extracted and will be described in more detail in chapter 7.

As an example of how the ordering exponent can be extracted from hysteresis loop data, loops from a 0.7 ML Pd/Fe/Pd trilayer, at the Pd edge, can be examined. The value of m at $H = 0$ obtained from the fit is the desired remanent magnetisation. Examples of typical hysteresis loops can be seen in the inset to figure 4.7. Using the remanent magnetisation from the hysteresis loop fitting, shown in the main body of figure 4.7, the magnetisation as a function of temperature can be plotted, where m is described by the power law $m = (T_\mathrm{C} - T)^{\beta_{eff}}$. The scaling exponent, β_{eff}, describes the dimensionality of the ordering which is governed by the spin and spacial degrees of freedom available to the magnetic lattice.

Extracting the ordering exponent from these data can be accomplished through log-log fitting. Plotting $log(m)$ against $log(T_\mathrm{C} - T)$ yields a linear trend with gradient β_{eff}. Small field induced tails in the data near T_C, visible in figure 4.7, make T_C difficult to define precisely. As such, T_C is initially chosen to be the point of

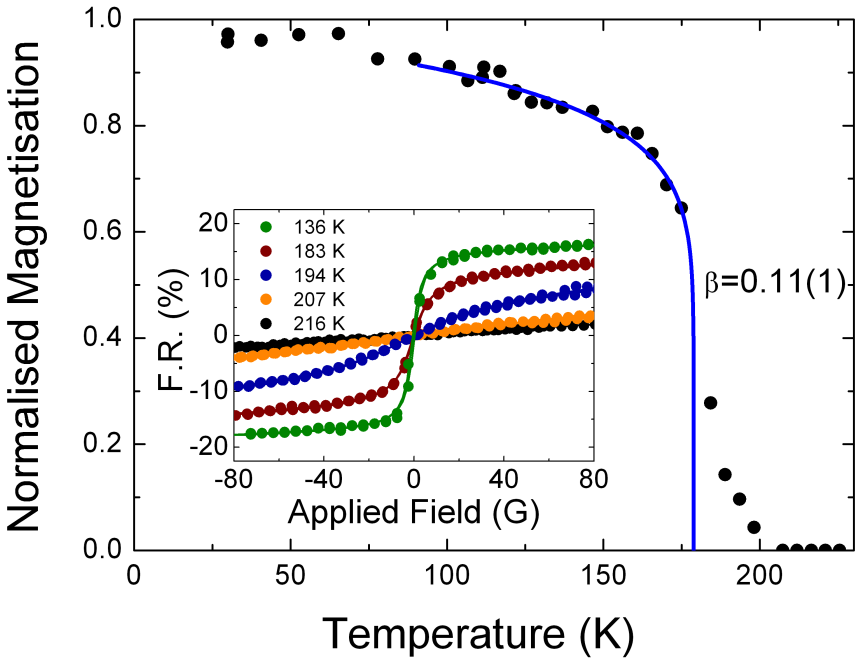

Figure 4.7: Magnetic ordering behaviour of a 1.1 ML FePd trilayer film deduced from arctan fits to hysteresis loops collected as a function of temperature (select loops shown in inset with half point density for clarity). Blue line shows the results of log-log fitting.

inflection in the data, where the tail begins, and is then adjusted to maximise the extent of the linear region over which the linear trend holds. This is the basis of the method outlined by Durr et al. [98].

The magnetic ordering data typically split into three regions governed by different power law dependencies. Below approximately 0.3 T_C, a Bloch law temperature dependence dominates. This region contains no additional information about the nature of the magnetic ordering dimensionality, so is often ignored. Loops collected in this region, where available, are used to improve the accuracy of normalisation, where $m(T = 0) = 1$ is used. For approximately $0.3 < T_C/T < 0.95$, critical behaviour dominates. This region is used to determine the magnetic ordering dimensionality through log-log fitting. Above approximately 0.95 T_C, field dependent tails may appear due to inhomogeneities in the applied field or material composition. The upper limit beyond which critical behaviour is lost varies from sample to sample; if the determined T_C remains close to the point of inflection, this limit tends to 1. In the log-log data shown in figure 4.8, the red points represent

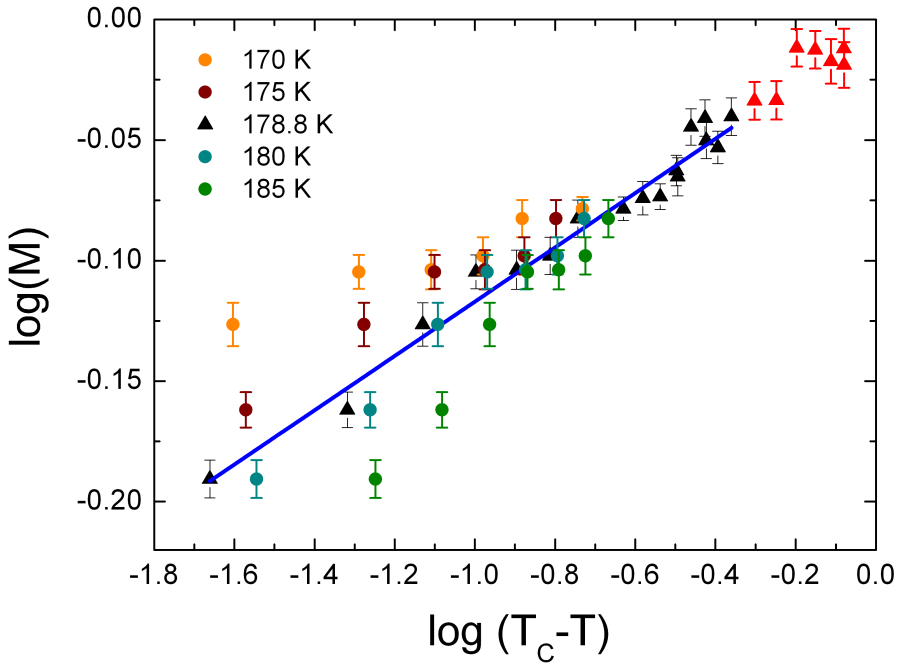

Figure 4.8: Log-log analysis of the Fe edge magnetic ordering data from a 1.1 ML FePd trilayer film showing the influence of T_C on the data linearity. The maximum range over which the linear trend hold occurs at 178.8 K providing a β value of 0.11(1) from the gradient of the linear fit (blue line). Near T_C data points for 170 and 175 K showed significant deviation from the linear trend and are outside of the plotted range.

the low temperature data where critical behaviour is not expected. The low point density close to the determined T_C prevents the appearance of the field induced region as the field affected data all appear above T_C.

The remanent magnetisation is obtained from the zero field loop height of the arctan fit to the data. Quantification of an error using this method is not straightforward, as the extracted value is not a fitting parameter. A reasonable approximation is made by examining the standard deviation from the fitted trend of the five data points closest to zero field. If more data points are included in this analysis, the chance of an outlier adversely affecting the data is minimised. However, due to the rapid falloff in magnetisation approaching T_C, the larger a field range used, the greater the affect of uncertainties in T_C. The resultant error bars, though too small to be seen in figure 4.7, become more critical when analysing the log-log data; the propagated errors in figure 4.8 are much more substantial. Though these

error bars appropriately weight the linear fit used to deduce the ordering exponent, β_{eff}, the uncertainty in β_{eff} is dominated by the uncertainty in T_{C}. To quantify the uncertainty in β_{eff}, the range of T_{C} values over which the linearity of the log-log data remains indistinguishable is manually determined. The concomitant change observed in β_{eff} over the limits of this range defines the uncertainty.

It should also be noted that it is also possible to directly fit a power law behaviour to the data. An additional convolution with a Gaussian broadening function can simulate the field induced tails. The scaling exponent, β_{eff}, and the broadening function are, however, strongly coupled to T_{C}. As there is not a reliable and consistent way to define T_{C} during this fitting, the results obtained using this method are more erroneous. All data presented in this work will therefore be analysed using the log-log method.

Chapter 5

FeZr/CoZr

5.1 Introduction

The production of novel magnetic devices is predicated by the understanding and exploitation of magnetic materials. As materials become thinner, the effects of interfaces becomes increasingly important. Measurements of interface moments have therefore attracted substantial attention within the literature. Often only the magnitude of the interface moments is measured, such as in [20, 99, 100], with more limited studies mapping the interface moments, such as in [45, 97, 101]. Throughout these latter studies, one of the primary limitations is resolution, which prevents more subtle interface effects from being observed. In this work, it will be the subtle influence of external stimuli on interface moments that will be of interest. By collecting high resolution data, and combing with the high resolution slicing available by using GenX, an attempt will be made to resolve the effects of changing temperature and applied field strength on interface moments. In particular, interface moments induced through the magnetic proximity effect, whereby a paramagnetic material in atomic contact with a ferromagnetic material becomes independently ferromagnetic, will be explored. Systems with induced moments naturally provide interfacial moments, and, at sufficiently low temperatures, allow them to be studied in the absence of the dominating influence of bulk moments without introducing additional material boundaries.

The effects of field and temperature on nett magnetisation are, of course, well known, but mapping the effects in induced magnetic profiles has yet to be achieved. To address this knowledge gap, an induced magnetic profile will be mapped, by fitting XRMS reflectivity data, to allow a robust assessment of any stimulated changes to the induced moments to be made.

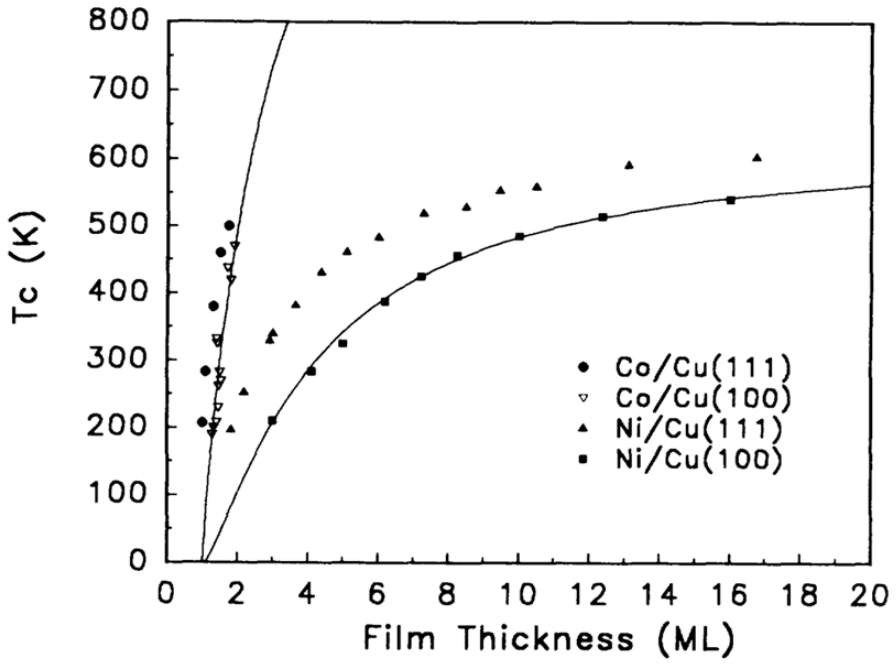

Figure 5.1: Taken from [102]. The critical dependence of ordering temperature on layer thickness in thin transition metal films. To produce a Co magnetic lattice which orders below 300 K, a film thickness of 1-2 ML must be used.

If the range of induced moments can be shown to change with external stimuli, then it is possible that changes in the magnetic ordering dimensionality could result. Low dimensional magnetic systems can display different magnetic behaviour to bulk materials due to the truncation of the magnetic lattice, as discussed in section 2.1.2. This is typically achieved through physical truncation of the lattice. However, changing the range or shape of an induced moment profile could allow the extent of the magnetic lattice to be controlled directly, which may allow changes in ordering dimensionality to be stimulated. The effect of external stimuli on the magnetic ordering dimensionality in systems with induced moments has not been explored in the literature.

There are then two main aims of this work: first to map changes in induced moment profile with changing external stimuli, and second to investigate the possibility of stimulating a dimensionality crossover through changing the extent of induced moments. The temperature dependence of the induced moment profiles will be examined first, in section 5.2, with the magnetic ordering dimensionality studied

in section 5.3. The field dependence of the induced profiles is then examined in section 5.3.1.

For these studies, the inducing moment will be provided by CoZr, with FeZr used as the polarisable material. FeZr and CoZr are both amorphous magnetic materials which, at sufficiently low temperatures, display ferromagnetic behaviour. However, the magnetic ordering temperature, T_C, of FeZr is considerably below that of CoZr. Bulk FeZr, with an Fe concentration of 93%, has an ordering temperature of approximately 120 K [103, 104] whereas bulk CoZr has a T_C above 950 K [105]. For a δ-layer of CoZr, the ordering temperature is significantly reduced. This has been demonstrated in Co layers, shown in figure 5.1. The CoZr layers used in this study have high Co concentrations (approximately 95%) and are thus expected to conform to the same trend. Therefore, to produce an inducing moment with an ordering transition within a conveniently accessible range (i.e. 50 - 300 K) CoZr layers within the monolayer (ML) regime are required. Induced moment profiles in systems of this type have not previously been mapped.

5.1.1 Previous Studies

Multilayered structures of alternating FeZr and CoZr provide a regime in which the effects of external stimuli on the induced moment profile can explored. MOKE studies of FeZr/CoZr multilayers, with varying FeZr thicknesses were therefore conducted [106] by our collaborators at the University of Uppsala. The CoZr layers were fixed to be 1 Å, with FeZr layer thicknesses of 25, 50 and 75 Å. These samples will be henceforth referred to by the FeZr and CoZr thicknesses in Å. For example, a multilayer with a 50 Å FeZr layer and 1 Å CoZr layer sample will be referred to as "50-1". All subsequent samples discussed in this work will be denoted similarly. The expected magnetic profile of the multilayers in this study are shown in figure 5.2. The subjects of primary interest to the study were the range of the induced moments, and the dimensionality of the magnetic ordering.

The range of induced moments was not measured directly during the study, as MOKE was employed which does not allow depth sensitivity. However, the 50-1 and 75-1 samples showed a very similar ordering temperature, around 230 K, whereas the 25-1 sample showed an increase in T_C to 270 K (more details are given in figure 5.3). This increase is likely due to the polarisation extent being sufficient to join neighbouring polarised regions. If the regions are separated, the magnetic regions, centred around the CoZr layers, may be sufficiently narrow to suppress out-of-plane magnetic excitations allowing only 2d magnetic excitations. If the FeZr layer thickness reduces to the point that adjacent induced moment profiles

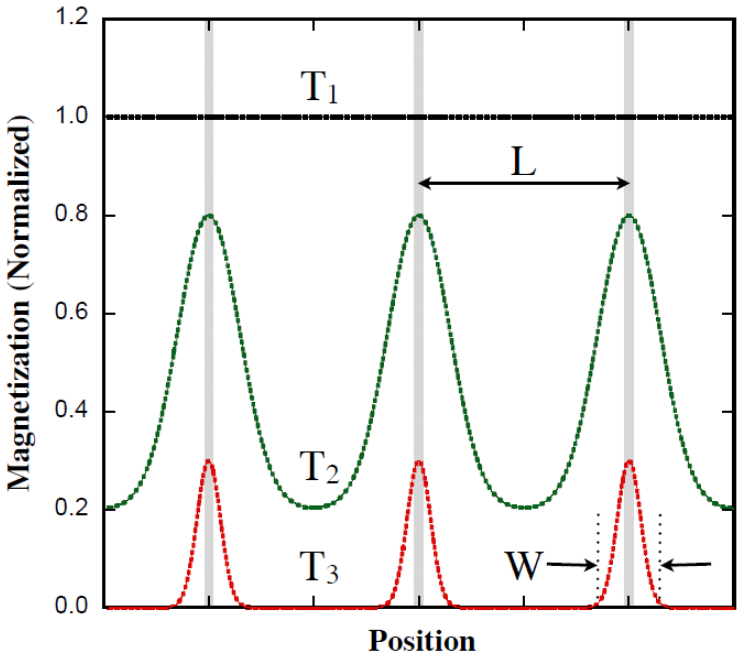

Figure 5.2: Taken from [107]. Schematic illustration of the expected magnetic profile in an FeZr/CoZr multilayer. The grey regions represent the regions with higher ordering temperature (CoZr), embedded in a material with a lower ordering temperature (FeZr). At low temperatures (T = T1), the magnetization is expected to be constant. At elevated temperatures, a periodic magnetic profile emerges (T = T2 and T = T3). The width of the magnetization profile is denoted by W.

overlap, out-of-plane excitations may form, producing a 3d magnetic lattice. This extra excitation mode allows the magnetic lattice to dissipate thermal energy more efficiently, and thus retain its nett moment at higher temperatures. This simple result suggests that the polarisation extent within the FeZr is between 12.5 and 25 Å.

Magnetic ordering data were also collected as part of the previous MOKE study by Ahlberg et al [107]. These data were collected to determine the magnetic dimensionality as T_C was approached. The results are shown in figure 5.3. β and δ were determined from the ordering data and field dependence at T_C respectively, tabulated in figure 5.3. The results obtained were ambiguous, showing no clear correlation between the two equally valid methods of evaluating the dimensionality.

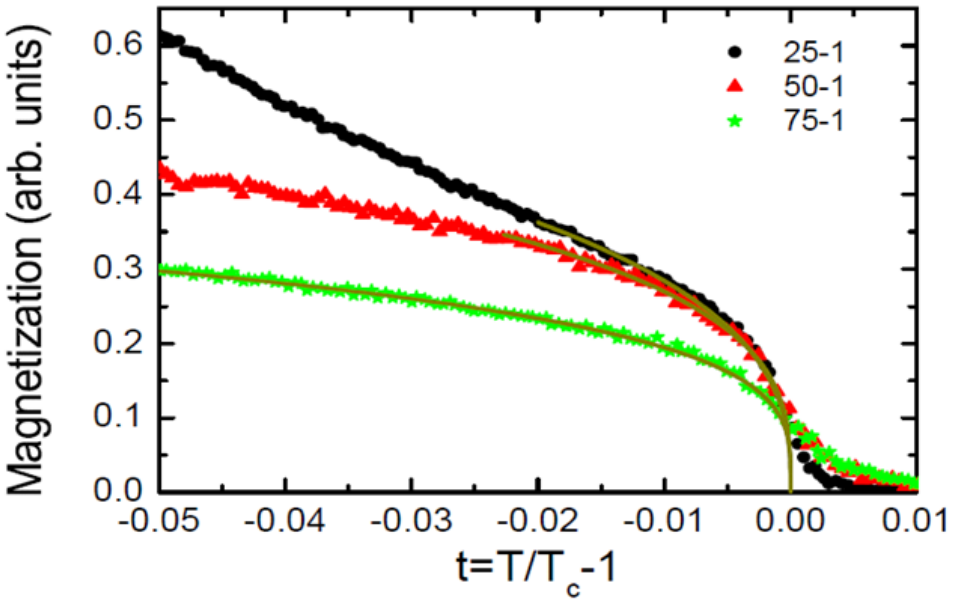

Sample	T_c (K)	β	δ
25-1	270.8(1)	0.35(1)	6.10(31)
50-1	230.7(1)	0.31(1)	6.34(29)
75-1	229.8(1)	0.26(1)	8.54(13)

Figure 5.3: Taken from [107]. MOKE data showing the magnetic ordering behaviour of a series of FeZr/CoZr multilayers as a function of FeZr thickness. The results of further analysis are shown in the included table. An increase in the ordering temperature is observed in the thinnest sample due to the overlap of the induced moment profiles.

5.1.2 Samples

The most suitable FeZr thickness for the continuation of these studies is one which produces a system containing narrowly separated polarised regions. If the regions are close to amalgamating, a smaller change in temperature or field may be required to produce a dimensionality change. This is advantageous as, if the external stimulus widens the polarised region, the potential change in dimensionality may have an observable effect on the ordering temperature. As a 50 Å FeZr thickness was the narrowest examined in the original MOKE study [106] which maintain disconnected polarised regions. Resonant scattering studies will be performed on similar samples with a 50 Å FeZr thickness. These studies will endeavour to map the induced

moment profile as a function of temperature and field.

New samples were grown, using DC magnetron sputtering, on Si (naturally oxidised) topped with a 50 Å AlZr buffer layer. Ten repeats of 50 Å FeZr and X Å CoZr were then grown (with X = 1,2) and capped with an additional 50 Å of FeZr and a final 50 Å AlZr layer. All samples used in this study follow this same basic structure with a multilayer composition that has a magnetic structure which only varies in the out-of-plane direction.

5.2 Temperature Dependent Profiles

One way of more accurately measuring the extent of the FeZr polarisation is to measure the ordering temperature in a range of samples with small variations in FeZr thickness. The limitations in the accurate control of layer thicknesses during growth (typically assumed to be $\approx 10\%$) make this an undesirable option. Additionally, this measurement of the profile extent is limited to being recorded at T_C. A more accurate determination of the induced polarisation profile can be achieved using resonant x-ray reflectivity, as detailed in the previous chapters. This allows the structural and magnetic profiles to be determined directly.

A direct measurement of the profile extent allows the magnetisation to be mapped at an arbitrary choice of temperatures. It is possible that an induced profile of this type will vary in its extent as the temperature is altered. An increase in temperature will reduce the nett magnetisation within any magnetic system, as the thermal excitations overcome the magnetic order. The closer a system is to its ordering temperature, the greater the influence of additional thermal excitations (see section 2.1.2). In a system with an induced magnetic profile, the polarised regions furthest from the inducing moments are most weakly ordered and display the weakest magnetisation. This produces a decaying moment with increasing distance from the inducing atoms (as illustrated in figure 5.2). As the temperature increases, those areas with the weakest moments, and thus weakest magnetic coupling, may lose their magnetic order first with a concomitant reduction in induced profile extent.

To investigate the spatial extent of the induced magnetic moments, magnetic reflectivity data were collected from a 50-2 sample at the Fe edge. These studies were performed on the X13A and U4B beamlines at the NSLS. Due to the large proportion of the sample volume containing resonant magnetic scatterers, complementary Cu K-alpha laboratory x-ray reflectivity data were collected to help refine the sample structure. The hard x-ray data were collected at room temperature while the resonant data were collected a 50, 100 and 300 K. Thermal expansion is

expected to be negligible over this temperature range.

Data were collected from a 50-2 sample, i.e. with a different CoZr thickness than the original study in [107], for two reasons. First, the increased moment of the thicker CoZr layer should make analysis of the magnetic structure easier as the magnetic signal is stronger. Second, the larger Co moment increases T_C so that it is above room temperature [102]. This means that the structural hard x-ray data, which could only be collected at room temperature, could be fitted with room temperature resonant data where the magnetic response still exists. This should improve the quality of the fitting.

To produce the fits, the expected sample structure was first refined by fitting only the hard x-ray data. The structure was then fixed while a second refinement to the magnetic structure at room temperature was performed using the resonant data whilst fitting both real and imaginary parts of the resonant scattering factors. The room temperature data was chosen as it was collected at the same sample temperature as the hard x-ray data; it also provided the best signal to noise. The magnetic structure was allowed three degrees of freedom: the magnetisation at the centre of the FeZr layer, the magnetisation at the interfaces between FeZr and CoZr, and the magnetic roughness between the two. These parameters were shared by all FeZr layers. Two additional parameters were included to allow the interface moment and magnetic roughness to have a 5% discrepancy above and below the CoZr layers to account for any small asymmetries in the profiles. These parameters were again shared by all FeZr layers, and were also shared across all temperatures. A final global fit was then performed which included all structural and magnetic parameters fitted simultaneously to both hard and resonant x-ray data. The results of this fitting strategy are shown with the reflectivity data in figure 5.4. The Fe edge structural profile is included in figure 5.5, with the structural parameters from the fitting procedure detailed in table 5.1.

Typically, materials which are stored and transported in air, can be assumed to have an oxide thickness around 2 nm as a starting point within the simulation pro-

	Si	AlZr	FeZr	CoZr	FeZr (upper)	FeZr Oxide	AlZr Oxide
Thickness (Å)	-	55.1	48.6	0.43	42.6	3.3	69.2
Roughness (Å)	1.4	5.7	0.5	0.0	8.5	3.3	9.4

Table 5.1: Structural parameters from the GenX fit to the 50-2 FeZr/CoZr multilayer data shown in figure 5.4.

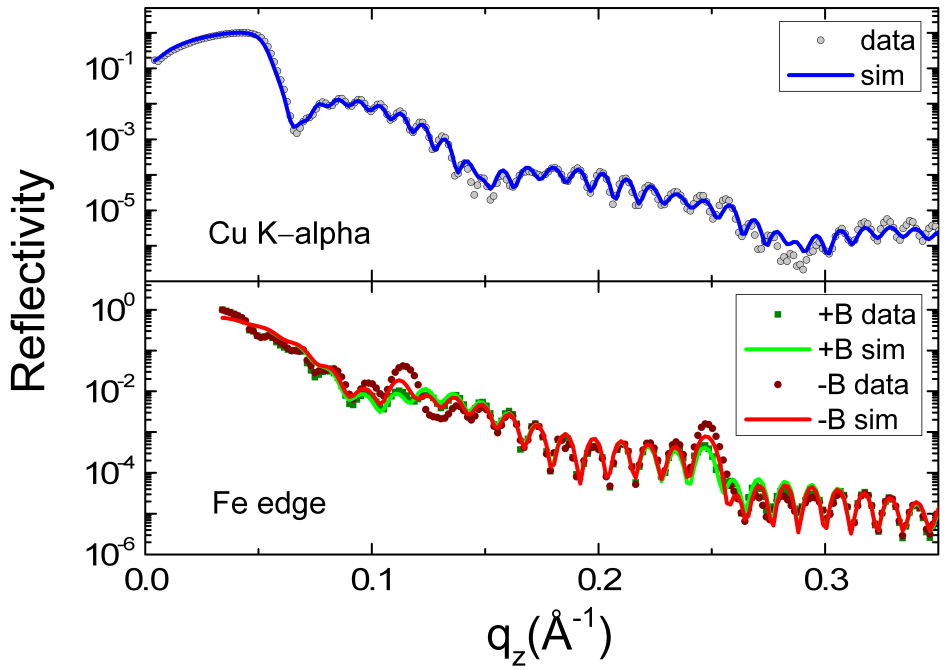

Figure 5.4: Simultaneously fitted hard and resonant (Fe edge) x-ray reflectivity data from a room temperature FeZr/CoZr multilayer material with FeZr and CoZr thicknesses of 50 and 2 Å respectively. Data were collected by Martina Ahlberg from Uppsala University.

cess. The structural fitting to the hard x-ray data, however, showed the 50 Å AlZr capping layer was fully oxidised. This corroborates results from AlZr films of similar composition [108] where oxide thicknesses of 4-6 nm were measured. As the multilayer terminates with FeZr, this will not adversely affect the magnetic profile as the upper surface of this terminating FeZr layer is not expected to be magnetic. The impact of the high level of surface oxidation on the uppermost FeZr layer can be seen in figure 5.5. Any influence on the magnetic profile is expected to be minimal.

Considerable effort was made to improve the fitting quality in the region around the Bragg Peaks (BPs). It is in these regions that the sensitivity to the magnetic profile is greatest, and so accurate fitting within these regions is clearly desirable. Although there is no evidence to suggest a more complicated magnetic structure than a decaying moment profile within the FeZr, attempts to improve the fits included: antiferromagnetic alignment of neighbouring CoZr layers, i.e. the reversal of the moments at subsequent CoZr layers, antiferromagnetic alignment of FeZr moments above and below each CoZr layer, and negative moments in the

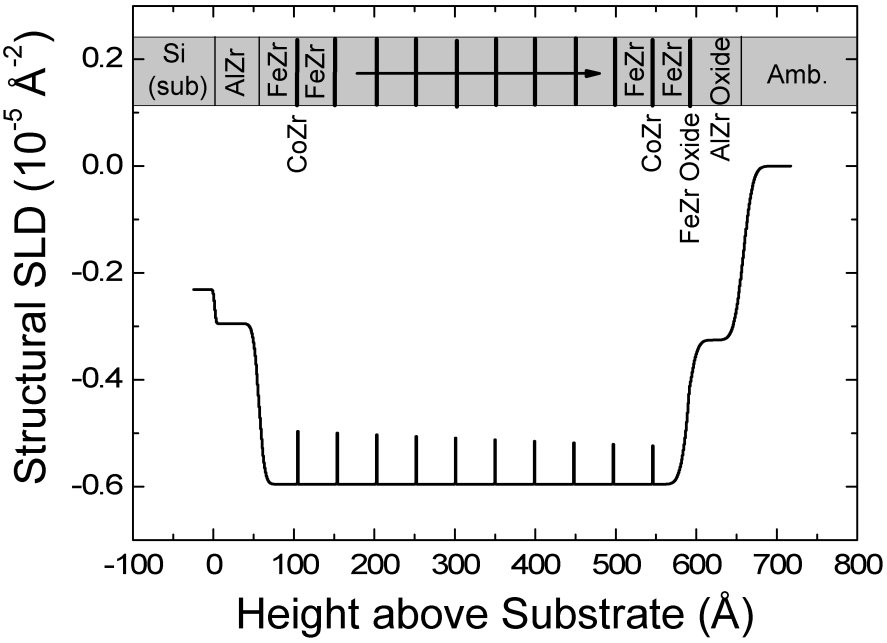

Figure 5.5: The structural profile of a 50-2 FeZr/CoZr multilayer, produced through the fitting of Fe edge resonant reflectivity data. A corresponding sample schematic is included. "FeZr Oxide" is an alloy of 93% FeO and 7% ZrO. "AlZr Oxide" is an alloy of 70% Al_2O_3 and 30% ZrO. The differences in amplitudes of the SLDs at the CoZr positions are an artifact of rebinning.

centre of the FeZr layers. All of these models had a detrimental impact on the fitting quality, and so the simple and intuitive model remained, though the fitting quality remained suboptimal.

Once the best achievable fit was finalised, the additional data collected at different temperatures were included. All structural parameters remained fixed to those ascertained in the initial fit. Each new data set was allowed the three magnetic degrees of freedom described earlier, to fit the profile, and a variable incident intensity to account for changes in beam current between samples. The reflectivity at these additional temperature are displayed, with their corresponding fits, in figure 5.6. The resultant magnetic profiles from fits at all temperatures are displayed in figure 5.7. The profile across the whole sample volume at base temperature is displayed in the lower panel, with the variations as a function of temperature across one CoZr layer shown in the upper panel.

The data do not suggest that the profile narrows with an increase in temper-

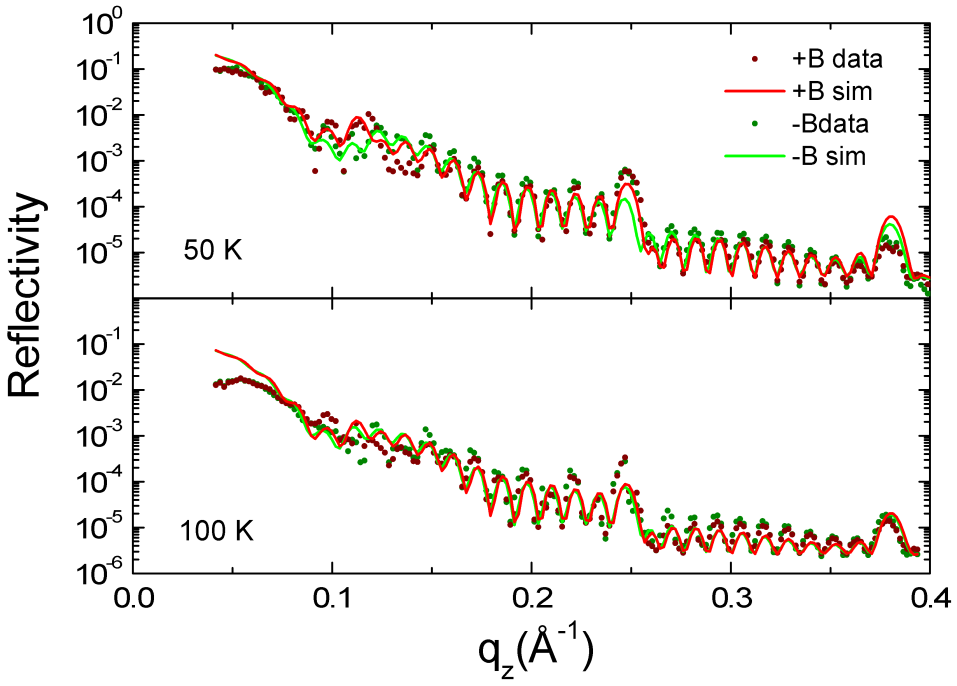

Figure 5.6: Simultaneously fitted Fe edge x-ray reflectivity data from an FeZr/CoZr multilayer material with FeZr and CoZr thicknesses of 50 and 2 Å respectively. Data were collected at the temperatures indicated by Martina Ahlberg from Uppsala University.

ature. An increase in the magnitude of the moment closest to the CoZr interface is caused by an increase in the strength of the inducing CoZr moment which is proportional to the induced moment. The magnetic profile at room temperature displays a profile with an extent of approximately 2 nm which loses its moment at the centre of the FeZr layer. A significant moment exists throughout the sample volume at the lowest temperatures available.

The inaccuracies in the fitting process mean that an accurate profile shape, for which only subtle changes in the data are expected, is difficult to determine. One potential cause of error is a change in sample structure between temperatures. This is not only thermal expansion, which is likely to be small, but a change in the oxide thickness, or deposits building up on the surface of the sample while cold. However, the magnitude of the splitting, and therefore magnitude of the magnetisation profile, should remain unaffected by these structural changes and is therefore determined with greater accuracy.

The resultant profiles appear to show that below the FeZr ordering tempera-

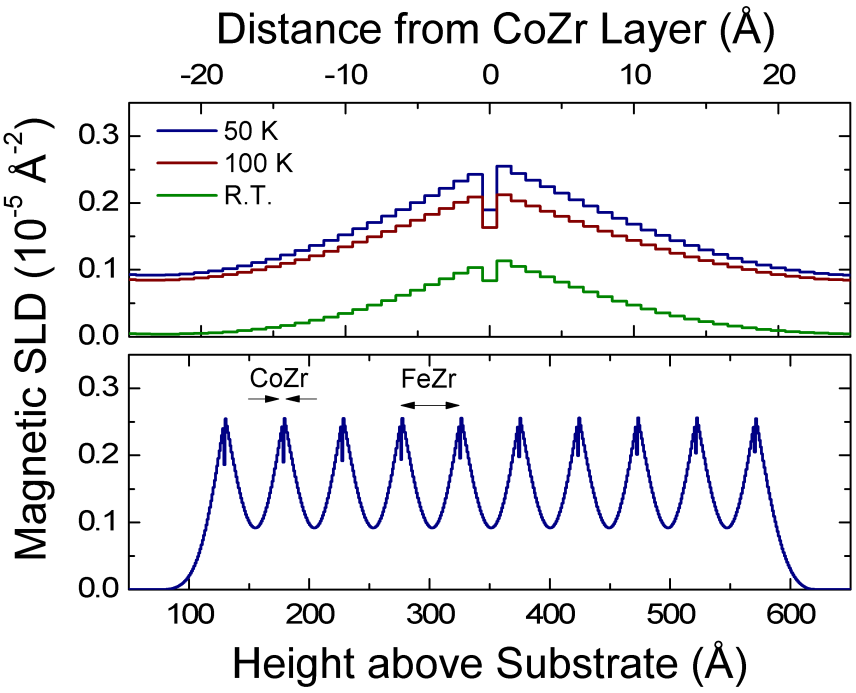

Figure 5.7: Magnetic profiles from fitting Fe edge reflectivity data from an FeZr/CoZr multilayer material with FeZr and CoZr thicknesses of 50 and 2 Å respectively. Lower panel shows 50 K data while the upper panel shows the temperature dependence of the profile shape.

ture (approximately 150 K for bulk FeZr), the induced and intrinsic FeZr moments work additively to produce the profile seen. As the temperature is increased, the intrinsic FeZr moment reduces while the induced moment remains relatively unaffected. An approximately constant reduction, throughout the sample volume, in the magnetisation as a function of depth is then observed. At room temperature, the intrinsic FeZr moment is minimal and an almost zero moment is observed 25 Å from the CoZr (the centre of the FeZr layer).

If it is assumed that a non-zero moment at the centre of the FeZr layer is sufficient for long-range out-of-plane excitations, and thus a 3d phase to be formed, the moment profile observed as a function of temperature suggests the possibility of a dimensionality change as a function of temperature. At the lowest temperatures, when below the FeZr ordering temperature, a 3d phase is expected as the whole sample volume is expected to be magnetic. As the temperature is increased, and the central FeZr moment is lost (due to the ordering of the intrinsic FeZr moment) a transition to a 2d phase could be observed. Further increase in temperature would

then lead to the loss of the total moment as T_C is reached. The presence of these phases in the Fe moments can be determined through analysis of the magnetic ordering behaviour.

5.3 Magnetic Ordering

As a function of temperature, a step change in the magnitude of the Fe moment would be expected if the system transitions from one magnetic dimensionality to another due to the concomitant change in ordering temperature. As a dimensionality crossover does not represent the loss of the moment within the lattice due to thermal fluctuations, it is not governed by the universality classes used to categorise traditional magnetic ordering behaviour. However, the behaviour as T_C is approached should still be dictated by the dimensionality of the final state, and should therefore be determinable. The indication from the magnetic profiles is that a 2d phase will be present as T_C is approached.

The data collected as part of the previous work performed by our collaborators [107], shown in figure 5.3, does not show any step change in behaviour as a function of temperature. However, attempts to determine the magnetic ordering dimensionality produced ambiguous results. It is possible that this ambiguity arises from a difference of behaviour between the two magnetic sub-lattices; behaviour which MOKE studies can not resolve. To remove the influence of the Co lattice, XRMS can be employed. In particular, the FeZr sub-lattice should be probed as it is within this lattice that change in out-of-plane excitation will potentially occur, and so it is the dimensionality of the Fe moments which is of primary interest. As such, Fe edge magnetic hysteresis loops were collected at the first Bragg peak position, for a similar 50-1 sample, as a function of temperature.

Using a 50-1 sample, though different to that used in section 5.2, provided the advantage that the ordering temperature is below room temperature and is within the accessible range of the experimental setup used. The hysteresis loops were fitted to pairs of arctan functions, examples of which are shown in figure 5.8. The loops show clear ferromagnetic alignment which exists until approximately 210 K. The sample displays a very small coercive field of ≈ 0.2 mT at 50 K. As the coercivity is so small, accurate determination of the zero-field loop height is compromised. As such, the remanent moment as a function of temperature was extracted from the loop heights in an applied field of 0.05 mT. This resulted in the magnetic ordering data shown in figure 5.9.

The sample alignment was re-optimised at 100, 150 and 200 K. Immediately

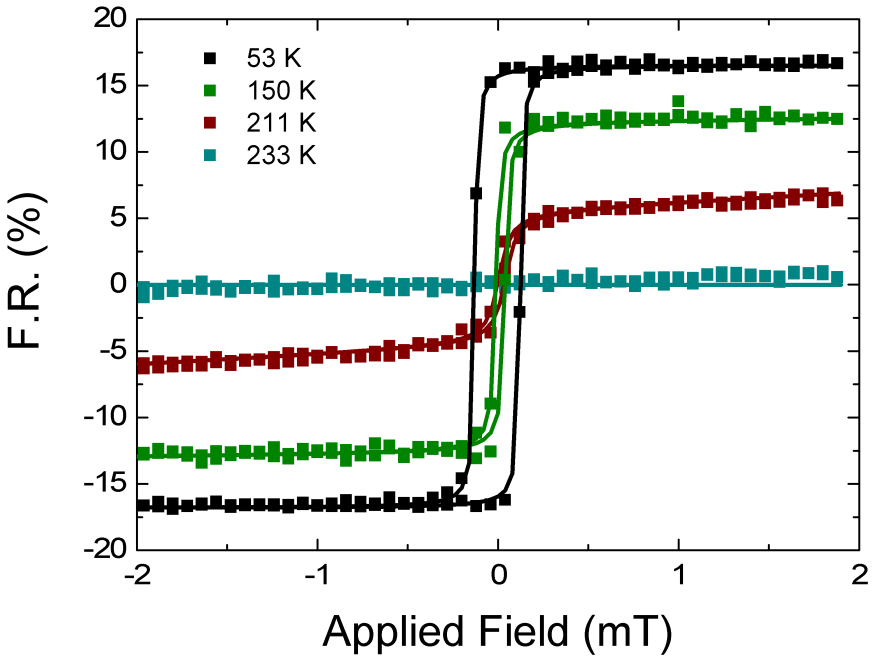

Figure 5.8: Magnetic hysteresis loops, as a function of temperature, from a FeZr/CoZr multilayer with FeZr and CoZr thicknesses of 50 and 1 Årespectively.

before these points, a reduction in the magnetisation from the trend is seen which is not related to the sample behaviour. The data show a linear reduction in the magnetisation as a function of temperature between 50 and 200 K. This corresponds with the reduction in magnetisation shown in figure 5.5. Above 200 K, the magnetisation is rapidly lost. The magnetic ordering dimensionality of the system can be found through analysis of the log-log data (as discussed in section 4.2.3), which is shown in figure 5.10. T_C was chosen to be the point of inflection in the data, which is around 205 K. Due to a sample realignment after collection of the 200 K data point, the 205 K point does not fit the trend of the data. This, coupled with the low point density in the critical region meant that accurate determination of T_C in the usual way, through maximising the linear region of the log-log plot, was not possible. Instead, the starting position of 205 K was used for the analysis. The linearity of the trend does not hold over a wide range of temperatures. The few points close to T_C over which the linearity does appear to hold are fitted to a linear trend with a gradient of 0.15. An ordering exponent of 0.15(1) falls between those of the 2D Ising ($\beta = 0.125$) and 2D XY ($\beta = 0.23$) universality classes, and so can not be unambiguously classified. Determining the magnetic ordering exponent in systems

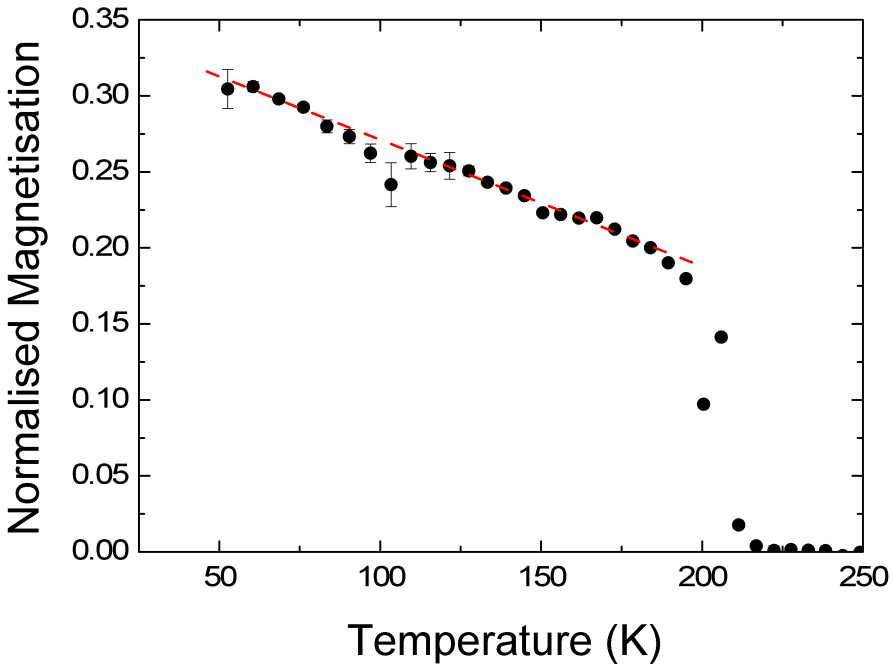

Figure 5.9: The magnetic ordering behaviour of a 50-1 FeZr/CoZr multilayer extracted from fitted hysteresis loops as a function of temperature. The data show a linear decrease in remanent moment, indicated by the broken red line, before a sharp fall to zero at $T_C \approx 205$ K.

which are far from the bulk is intrinsically difficult, as the theoretical descriptions do not account for the pronounced effect of the interfaces. It is possible, however, that the particular ambiguity displayed is due to a crossover in dimensionality within the critical region.

A further attempt to quantify the dimensionality can be conducted using the field dependence of the magnetisation at T_C. This has the advantage that the dimensionality can be sampled at one temperature, which eliminates the possible influence of an evolution in dimensionality as a function of temperature. As the magnetic ordering data were collected through analysis of hysteresis loops, analysis of the field dependence can be conducted on the loop closest to T_C. As the loop closest to T_C, at 205 K, was not representative of the other data, the next available point at 211 K was chosen for this analysis, the results of which are shown in figure 5.11. Fitting a linear trend to the log-log data yielded a gradient of 0.14 which corresponds to $\delta = 7(1)$. This ordering exponent falls between those of a 3D Heisenberg ($\delta = 4.8$) and 2D XY ($\delta = 15$), which is again ambiguous. The value of

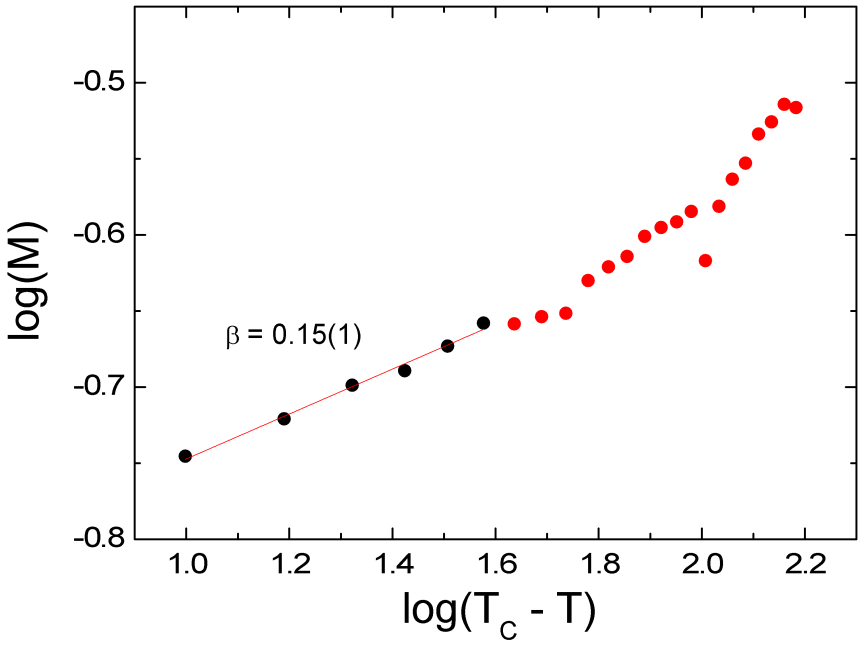

Figure 5.10: Log-log analysis of the magnetic ordering behaviour of a 50-1 FeZr/CoZr multialyer (points). The gradient of the linear fit (line) produces an ambiguous ordering exponent of $\beta_{eff} = 0.15(1)$.

δ is comparable to that obtained in the original MOKE study, suggesting that those data were not compromised by the additional influence of the Co lattice.

As with the original MOKE study, a transition from a 3d phase into an intermediate 2d state is not observed. The loss of the moment in a manner which is not consistent with any universality class, coupled with the ambiguity in the ordering exponents from the MOKE study, suggest that the ordering temperature of the 2d phase is below the intrinsic ordering temperature of the FeZr layers. The phase transition observed instead describes the sample, which is in a 3d state below the transition, approaching the intrinsic ordering temperature of the FeZr. As the intrinsic FeZr moment is lost, the out-of-plane lattice excitations are lost. The thermal energy which was dissipated in this direction must instead be dissipated in the remaining in-plane directions, which is sufficient to overcome the remaining magnetic order of the induced and inducing moments.

This contradicts the hypothesis put forth in the MOKE study to account the different ordering temperatures observed as a function of FeZr thickness. As described earlier, it was proposed that large FeZr thicknesses would produce isolated

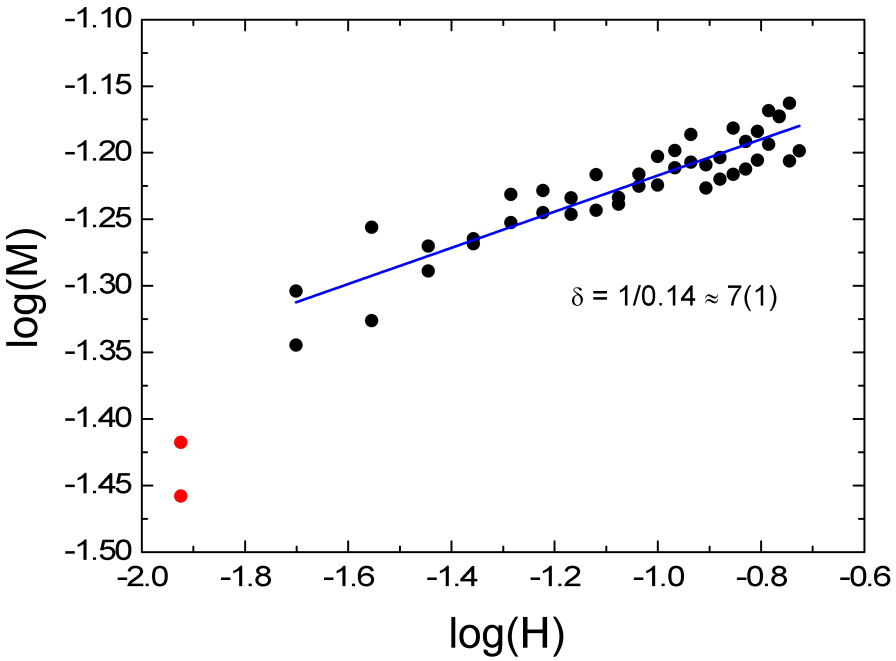

Figure 5.11: Log-log analysis of a hysteresis loop from a 50-1 FeZr/CoZr multilayer close to T_C(points). The gradient of the linear fit (line) produces an ambiguous ordering exponent of $\delta = 7(1)$.

polarised regions in which only 2d excitations could exist. Narrower FeZr layers were expected to allow the overlap of adjacent polarised regions to produce 3d excitations and higher ordering temperatures. In light of these new XRMS data, a new description of the two distinct phases can be produced. If the induced moment profiles are sufficiently separated (i.e. the FeZr thickness is sufficiently large) that they do not overlap, the moments at the central FeZr regions (those which are furthest from the CoZr layers) can be said to solely arise due to the intrinsic FeZr moment. The range of the induced moments was earlier shown to be approximately 25 Å and so FeZr thicknesses of 50 Å and above can be said to satisfy this criterion. If the existence of out-of-plane moments is dictated by the existence of these central moments, then the dimensionality is dictated only by the intrinsic FeZr moment. At the point that the FeZr moment is lost, a dimensionality crossover from 3d to 2d will be observed for any FeZr thickness greater then 50 Å. This explains the similarity of the 50-1 and 75-1 magnetic ordering data from the original MOKE study. If the FeZr thickness is below 50 Å, the induced moment profiles begin to overlap. The magnitude of the central FeZr moments is then governed by both the intrinsic FeZr

moment, and the moment induced by the CoZr. In this geometry, the loss of the intrinsic FeZr moment is not sufficient to induce a dimensionality crossover, allowing for more efficient thermal dissipation within the magnetic lattice, and producing an increase in T_C. As the temperature increases, the magnitude of the induced moment will gradually decrease throughout the sample volume. At some critical temperature, the strength of the induced moment in the central FeZr position will become insufficient to support out-of-plane magnetic excitations and the transition from 3d to 2d will again occur, and the total moment will be lost. This is observed in the increased T_C of the 25-1 sample. Neither of these distinct phase transitions represents a true critical ordering process, as it is induced by the dimensionality crossover, and so the origin of the ambiguity in ordering exponents becomes clear.

One area in which the data potentially contradict this result is the room temperate induced profile of the 50-2 sample (see figure 5.7). This profile shows a moment in the FeZr layer which has vanished while a nett moment remains. However, in the 50-2 sample, the increase in thickness of the CoZr layer has potentially lead to an increase in the ordering temperature of the 2d regime formed after the loss of out-of-plane excitations. In similar FePd trilayers [109] a linear increase in the ordering temperature is observed as the inducing Fe layer thickness is increased. It is therefore likely that the 2d moments exist above the intrinsic ordering temperature of the FeZr in the 50-2 sample.

The proposed hypothesis to explain the observed behaviour is that the loss of the central moment of the FeZr layer is sufficient to break the ordering within the system due to the transition into a 2d phase with a lower ordering temperature. If this hypothesis is correct, then the application of an applied field to the system above T_C could cause a rapid transition into an ordered state, as the out-of-plane excitations reform.

5.3.1 Field Dependence

Under the influence of an applied magnetic field, the magnetic susceptibility of a material causes an enhancement of the magnetisation. In a system which is above its magnetic ordering temperature, an applied magnetic field can realign the moments within the system and cause magnetic order to reform. If a field is applied to an FeZr film above its ordering temperature, the spontaneous moment would be reestablished. If the earlier hypothesis about the magnetic ordering behaviour is correct, then the reformation of the FeZr moment will reintroduce the long-range out-of-plane magnetisation. This boosts the ordering temperature of the induced and inducing moments which can then also realign.

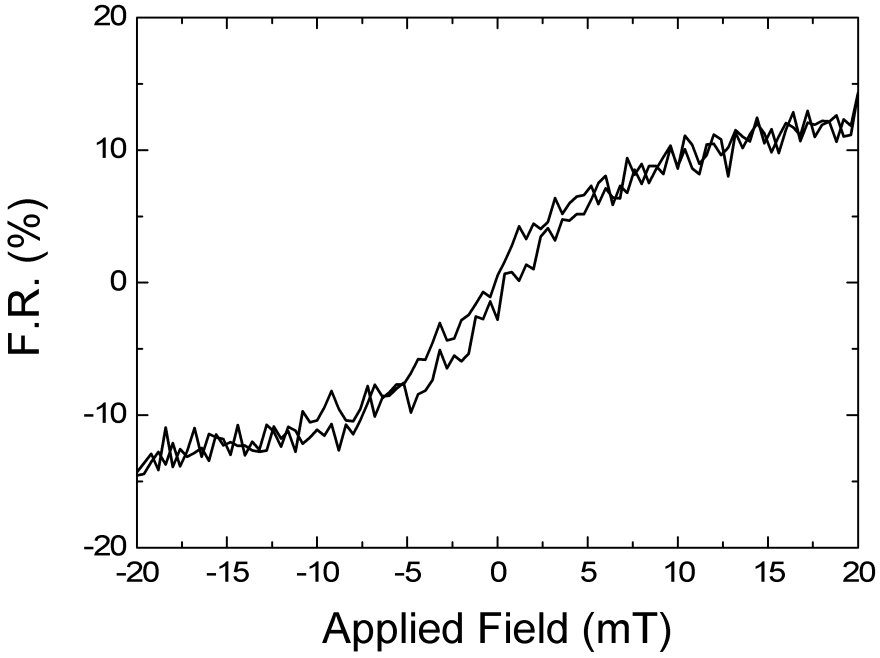

Figure 5.12: A hysteresis loop from a 50-1 FeZr/CoZr multilayer at 220 K, approximately 15 K above the ordering temperature of the system.

A further examination of the 50-1 sample must therefore be conducted as a function of applied field with the sample held just above T_C. By measuring the magnetic profile as a function of applied field strength, it is possible to map the magnetisation within the sample as the field realigns the moments. The dynamic response of the profile with applied field can then establish whether the hypothesised reordering mechanism is present. To investigate this influence of the applied field, a 50-1 sample was used; the same sample used for the magnetic ordering studies in the previous section. A hysteresis loop was first collected at the first Bragg peak position at 220 K, shown in figure 5.12.

The sample shows the broad paramagnetic response expected of a material just above its ordering temperature. At this temperature, approximately 15 K above the ordering temperature of the system, the response to an applied field is significantly smaller than at T_C. This potentially hints at the ordering hypothesis being incorrect, as a greater susceptibility would be expected if the moments were being additionally affected by the onset of out-of-plane excitations. However, the gradual response with field allows a controllable environment in which to study the profile shape as a function of applied field.

Field dependent reflectivity studies were carried out on 50-1 samples at the Fe L_3 edge using the X13A beamline at the NSLS. Data were collected at 220 K, the same temperature as the hysteresis loop in figure 5.12, in the field driven tail of the magnetic ordering data. As the field was fixed throughout each scan, the helicity was flipped at each point to gain magnetic sensitivity. The resultant reflectivity data were fitted using the GenX programme [94], and are shown in figure 5.13. As the reflectivity data at different fields only differ due to the changing magnetic contribution, only the structural contribution to the total scattering at the lowest field available is shown (uppermost panel). The central four panels show the fits and data from the magnetic contributions to the field dependent reflectivity, and the lowermost panel shows the residuals of these fits. The structural parameters from the fitting are shown in table 5.2, with a sample schematic corresponding to that shown in figure 5.5.

Due to a lack of hard x-ray data, the structure and resonant scattering parameters were refined simultaneously to the same data set (at 0.2 mT). To ensure the most robust fit possible, the fit was initialised using the fit to the 50-2 data as this included hard-x-ray data which was lacking for the 50-1 sample. As the two structures are likely to be very similar, this not only saved time, but prevented the fit falling into local minima. This is a more common occurrence when refining the structure and resonant parameters simultaneously due to their strong correlation. At subsequent field positions, only the magnetic profile was allowed to change with the same three degrees of freedom as described in section 5.2.

The energy chosen for this study, was closer to the Fe absorption edge than that of the 50-2 data shown in section 5.2. Due to the large volume of Fe within the multilayer stack, this has suppressed the fringes in the reflectivity data. As the resonant scattering terms are fitting parameters, and a good approximation to the structure is known, this has not impacted the quality of the achieved fit.

The field for the initial fit would ideally be zero to eliminate the change in absorption created by including a magnetic response. However, the small, unphysical coercive field displayed in this temperature region makes a non-zero applied field more prudent to avoid negative moments due to any field inhomogeneity. The lowest field data were therefore collected at 0.2 mT. The changing magnetic contribution, contained within the F.R., displays the change in magnetic profile. The F.R. ratio was used for this analysis, rather than fitting the two helicity channels, to allow the significance of the magnetic contribution within the overall fitting quality to be artificially increased. The weighting of the F.R. data to the overall quality of fit was multiplied by a factor of 10. This preferentially optimised the data fitting towards

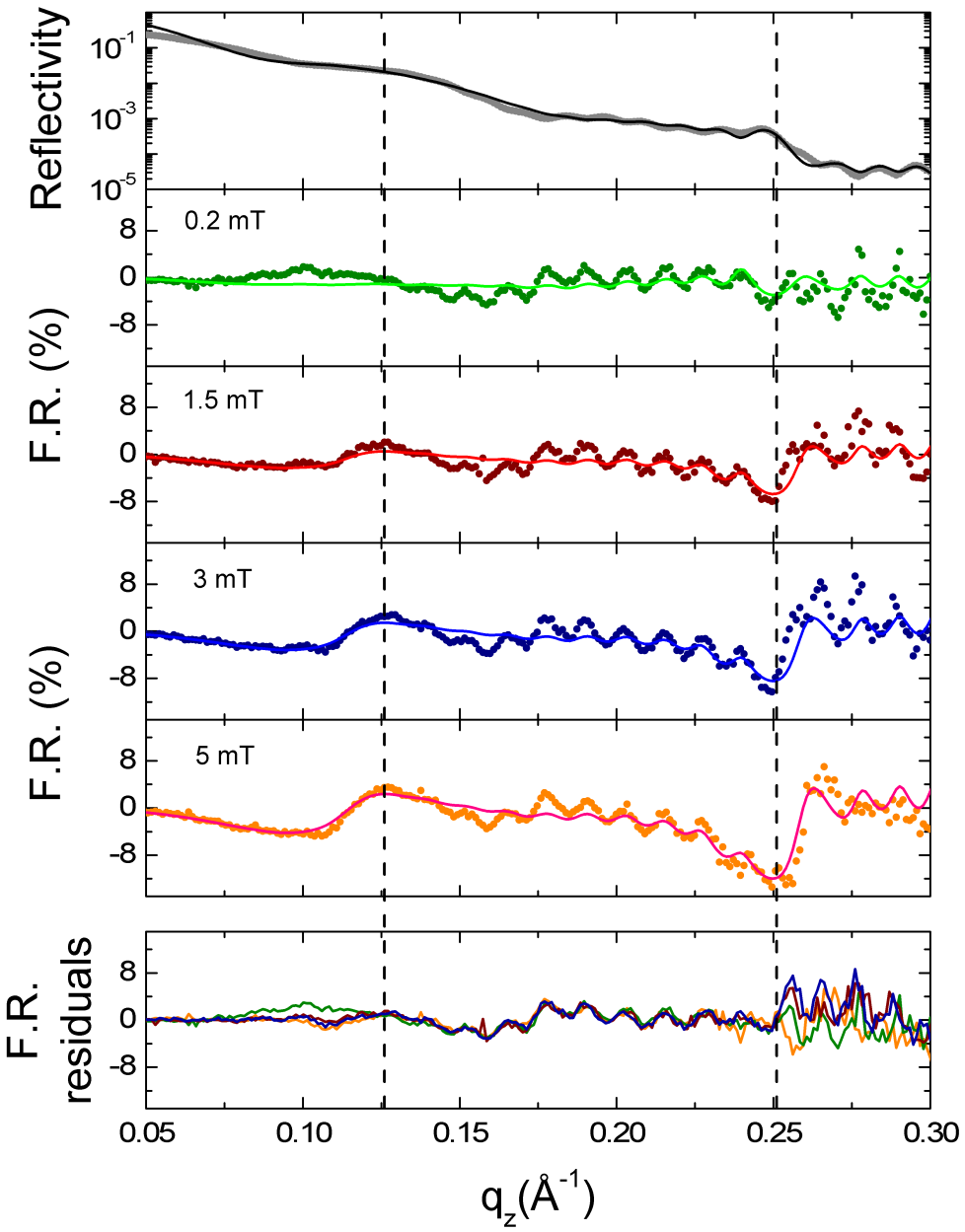

Figure 5.13: Fe edge magnetic reflectivity data (points) from a 50-1 FeZr/Zr multilayer as a function of applied field with fitted profiles (lines) produced using GenX [94]. Vertical broken lines show the first and second Bragg Peak positions.

the magnetic profile which was of primary interest.

The magnetic signal is weak due to the suppression of the Bragg Peaks caused by being too close to the resonance, and so the data are noisy. Within the F.R.s,

	Si	AlZr	FeZr	CoZr	FeZr (upper)	FeZr Oxide	AlZr Oxide
Thickness (Å)	-	56.2	48.6	0.43	40.6	10.2	69.6
Roughness (Å)	1.5	4.2	0.7	0.0	3.8	4.2	5.7

Table 5.2: Structural parameters from the GenX fit to the 50-1 FeZr/CoZr multilayer data shown in figure 5.13. "FeZr Oxide" is an alloy of 93% FeO and 7% ZrO. "AlZr Oxide" is an alloy of 70% Al_2O_3 and 30% ZrO.

the fitting quality is poor, particularly for lower q values. However, if the difference between the simulation and the data is taken (lower panel, figure 5.13) it is clear that all simulations differ from the data consistently. This means that there was a systematic error within the simulated model. This is most likely an error in the fitted structure which was difficult to determine accurately with the low intensity features within the data. The consistency between the residuals allows firmer conclusions to be drawn from the data as the differences in the data with respect to field are accurately represented by the differences in the profiles used within the respective models. Though the model is imperfect, the trend with respect to field can therefore be meaningfully examined.

If the F.R.s are compared, then useful information about the profiles can still be extracted. First, all field values showed a magnetic moment containing periodic fringes. The narrowest fringes, particularly prominent at higher q values, have equal intensity as a function of field. This shows that the background moment, i.e. the intrinsic moment of the FeZr, or moment at the centre of the FeZr layers, remains approximately constant between data sets. If the FeZr moment is increased in the higher field simulation, these fringes grow in amplitude.

Second, the enhanced splitting at the second Bragg Peak (BP) position (indicated in figure 5.13), which is observed in the data at the highest three field values examined, is missing from the low field data. This splitting at the BPs is caused by the induced moments within the FeZr layer which are centred around the CoZr sites, and thus around the BP positions. In the lowest field data it is therefore apparent that little or no induced moment is yet present. As the field strength is increased, the induced moment strengthens and the BP splitting is observed.

These observations are supported by the magnetic profiles produced from the simulations, which are shown in figure 5.14. At the lowest field values, a uniform moment is observed throughout. As the field strength is increased, the induced moment arises and subsequently strengthens. The central FeZr moment is minimally

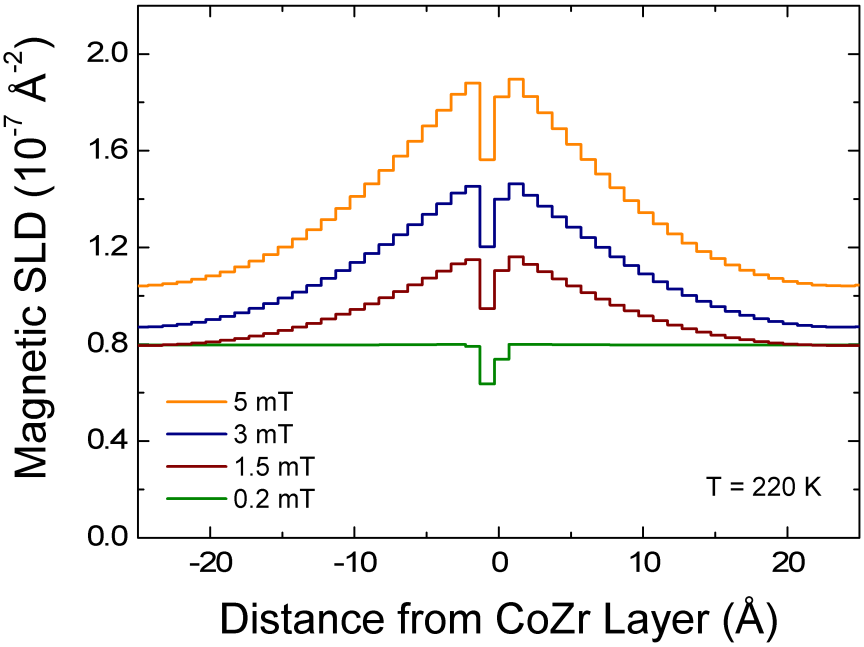

Figure 5.14: The resultant magnetisation profiles from Fe edge magnetic reflectivity data as a function of field from a 50-1 FeZr/CoZr multilayer. A small field first aligns a uniform moment with the FeZr. Further increases in field strength lead to the stabilisation and subsequent enhancement of the induced moment profile.

affected until the highest field strength is applied where it is still only moderately affected. The spatial extent of the induced moment profile remains approximately invariant over the field range examined.

Though the fitting quality is suboptimal, making affirmation of the behaviour difficult, these results appear to corroborate the ordering hypothesis. The applied field first produces a moment uniformly throughout the FeZr layer. This moment then establishes magnetic excitations in all three spatial dimension. After these excitations have been formed, the induced moments, which are no longer constrained to be 2d, can begin to form. Further increase of the applied field then enhances the strength of these induced moments.

5.4 Conclusions

Proximity effects and dimensionality changes have great potential to be exploited in future magnetic devices. This work sought to directly examine the influence of

external stimuli on the induced moment profiles in FeZr/CoZr multilayers through resonant x-ray reflectivity. Of particular interest was the change in the extent of the induced moment profile with changing temperature and field. It was expected that a narrowing of the profile extent with increasing temperature, and a widening of the profile with increasing field, would be observed. However, these assumptions were shown to be incorrect. With increasing field, or decreasing temperature, the data suggest that the induced moments increase in magnitude while maintaining their extent. Crucially, it is the presence of the intrinsic moment carried by the FeZr, rather than the additional induced moment it gains through proximity to the CoZr, which is responsible for the ambiguous magnetic ordering dimensionality observed. This ambiguity arises because the order-disorder transition is not represented by a typical universality class. Instead, the loss of the intrinsic moment in the FeZr leads to a dimensionality change within the magnetic lattice into a state which has a lower magnetic ordering temperature. The total moment is then rapidly lost. The application of an applied field when in a paramagnetic phase produces the opposite effect; the intrinsic moment is first stabilised, allowing out-of-plane moments to form and increase the ordering temperature of the lattice. The induced moment profile subsequently arises.

The details of the underlying mechanisms to these phenomena clearly warrant further investigation. A detailed study of the magnetic ordering behaviour and induced moment profile of an individual FeZr/CoZr/FeZr trilayer is greatly desired. A single trilayer allows the total sample thickness to be controlled by the FeZr thickness. If the FeZr thicknesses were 25 Å, giving a total sample thickness of approximately 50 Å, the out-of-plane excitations required for the formation of a 3d lattice could be eliminated. This would force a 2d regime to be formed in the polarised region. The ordering temperature of this 2d phase could then be investigated without the influence of a dimensionality crossover. It would be expected that the 2d ordering temperature would be below the 205 K of the multilayer sample studied in this work. This regime should also enable the dimensionality to be measured: 2D XY would be expected. If the FeZr thicknesses were subsequently increased, at some critical thickness the out-of-plane excitations would form, and a 3d regime would be created. This critical thickness is likely to be between 5 and 10 nm as it is in this thickness range that dimensionality crossovers have been observed in other systems [98, 110]. Above this thickness, the ordering temperature of the trilayer would be expected to be the same as that of the multilayer, as again the loss of the FeZr moments would drive the ordering of the whole sample volume. The measured dimensionality would again be expected to be ambiguous as the dimen-

sionality crossover, and loss of induced moment, prevents a universality class being represented. If the FeZr thickness was sufficiently increased to cause the intrinsic FeZr moment to dominate that of the induced FeZr moment, the dimensionality of the magnetic ordering may then resemble a simple 3d order-disorder transition. If these responses were observed in a simple trilayer, it would confirm the origin of the ordering mechanism used to describe the observed behaviour in the multilayer system, and our understanding of these low dimensionality systems would be greatly increased.

Chapter 6

FePd

6.1 Introduction

FePd systems, in a multitude of geometries and compositions, have been studied extensively both theoretically [111, 112] and experimentally [113, 114] in the literature. A variety of unusual properties have been observed. These properties are driven primarily by the high polarisability of Pd [115]. When a highly polarisable material, such as Pd, is in atomic contact with an itinerant ferromagnet (FM), an FM moment is induced within the Pd. A single atom of Fe in bulk Pd produces a so called "giant moment" as a polarised sphere of Pd is created, with a radius of approximately 1 nm, which produces an effective moment per Fe atom which is an order of magnitude larger than that of the Fe atom alone [116]. At an interface between Fe and Pd, where both induced and inducing moments are present, a regime is created with two interacting magnetic sub-lattices. This produces a unique opportunity to study magnetic interactions across a FM-FM interface. The behaviour of magnetic lattices close to an interface is crucial to the implementation of a spintronic device, where spin-polarised currents are necessarily conducted across a FM-FM interface. The substantial modification of the bulk magnetic ordering behaviour at an interface has been explored in a number of studies [117, 118]. However, the detailed nature of the behaviour of, and interaction between, magnetic sub-lattices across an interface remains poorly understood.

Previous studies [119] performed by our collaborators at the University of Uppsala, on FePd trilayer systems, showed some interesting and unexpected results. This study used the magneto-optic Kerr effect (MOKE) to study Fe thicknesses ranging from 0.3 to 1.5 ML buried in nominally bulk Pd. Firstly, although the Fe thickness used was significantly thinner than the 2 ML Ni thickness below which no

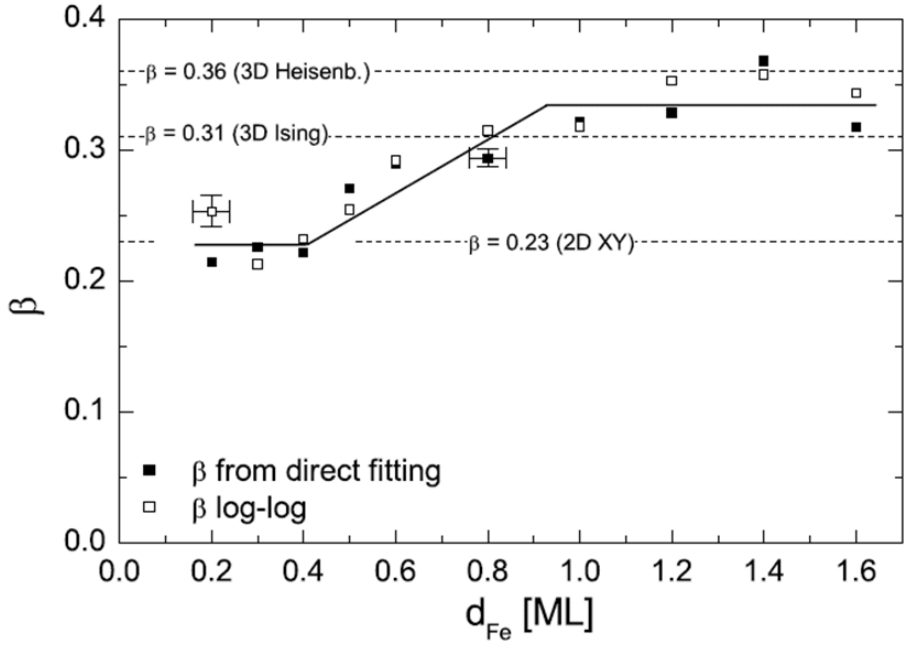

Figure 6.1: Taken from [119]. Ordering exponent, β, versus Fe δ-layer thickness, d_{Fe}, in FePd trilayer samples as determined by direct fitting and by double logarithmic plotting. The dashed horizontal lines represent β of the 2D XY, 3D Ising, and 3D Heisenberg models. The solid line serves as a guide to the eye. Typical uncertainties in β and thickness are indicated.

moment was observed, the total moment within this FePd system was never seen to vanish. As a nett moment was measured, polarised, diffusing electrons exist within the itinerant material. These electrons should then ensure that a moment is carried by both Fe and Pd sub-lattices. However, further, element specific experimental data are required to verify this expectation.

A second interesting result of this FePd study was an observed crossover in the magnetic ordering dimensionality, from 2d to 3d, as the Fe thickness was increased from 0.5 to 1 ML. The results are illustrated in figure 6.1. A concomitant increase in the ordering temperature, at a linear rate of 200 K/ML, was observed.

A similar dimensionality crossover has been seen in thin Ni films [110, 120] where a transition from 2d to 3d between approximately 5 and 10 ML was seen. The spin-dimensionality crossover in these works originates from the reduction in Ni film thickness to the point at which magnetic excitations in the out-of-plane direction become energetically unfavourable due to the decreasing wavelength of the available excitation modes.

In the FePd system, the spin-dimensionality crossover occurs at an Fe film thickness which is an order of magnitude smaller than that observed in the Ni. This difference in spatial extent is at odds with a dimensionality crossover which is driven by the allowed excitation modes, as these would be expected to be comparable between the two systems. However, the induced moment carried by the Pd lattice has a spatial extent which is likely to be comparable to the extent of the Ni films. The giant moment carried by the Pd lattice may dominate the MOKE response in the FePd studies, which is sensitive only to the total moment. If the range of induced Pd moments changes when the Fe δ-layer thickness is modified, the critical thickness needed to stimulate crossover in dimensionality may match that observed in Ni. This would not, however, conform with the theoretical expectation of a polarisation extent which varies only as a function of the Stoner factor (see equation 6.1).

A second, plausible explanation for the FePd dimensionality crossover arises when the linear increase in the magnetic ordering temperature, with increasing Fe δ-layer thickness, is considered. The increase in T_C is caused by an increase in the coupling strength within the magnetic lattice. This allows higher energy, shorter wavelength excitation modes can be supported. As the Fe δ-layer thickness is increased, shorter wavelength excitation modes become available until the wavelength is sufficiently short to exist in the spatially confined out-of-plane direction. This is the crossover mechanism proposed by Pärnaste et al. in the original study [119]. This hypothesis relies on the assumption that the Fe and Pd sub-lattices are directly coupled allowing the increasing Fe coupling strength to also permeate the Pd lattice. Identical ordering behaviour would then be expected for both sub-lattices. However, observations of ultrathin Fe films on Au substrates [98] indicate that for Fe thicknesses of 1-3 ML, the magnetic ordering exponent is invariant; remaining 2D XY.

Clearly, ambiguity exists between the descriptions available in the literature. The literature suggests one of two possibilities. First, the crossover observed in the FePd trilayer materials [119] is driven by a changing profile extent, in which case the system is not conforming to the theoretical description of the profile extent [52]. Second, the Fe and Pd lattices are directly coupled (allowing an increase in the Fe coupling strength to increase the Pd coupling strength), in which case the observed crossover in dimensionality does not conform with the observations of 2D XY moments in Fe films on Au [98].

The work presented in this chapter will build upon the work by Pärnaste, and extend the studies of FePd trilayers to include element specific analysis. First, the spatial extent of the moments on each sub-lattice must be determined to in-

vestigate if there is any change in the extent of the polarised Pd region upon a change in Fe δ-layer thickness. This can be achieved through the fitting of element specific specular reflectivity data, and is addressed in section 6.2. Next, the element specific magnetic ordering behaviour must be investigated, again as a function of Fe thickness, which is addressed in section 6.3. This allows two properties of the magnetic lattice to be determined. First, the dominance of total moment by the giant Pd moment can be verified by comparing Pd edge ordering data to the results of the original MOKE study [119]. Second, the coupling between the sub-lattices can be investigated by comparison of their respective dimensionalities. It is hoped that combination of these studies can lead to a new understanding of the magnetic interaction mechanisms across interfaces, and ultimately produce an alternative interpretation of the literature data which addresses the observed inconsistencies. The last part of this chapter will investigate the unexpected loss of the Fe moments, in the thinnest δ-layers studied, which was observed for the first time during the course of these investigations. This remarkable observation will be discussed in section 6.4.

Mapping the magnetic profiles and measuring the magnetic ordering both require element specificity for which x-ray magnetic scattering (XRMS) will be the primary investigative tool. Complementary studies using polarised neutron reflectivity (PNR) will aid this work.

6.1.1 Samples

In order to study the effects of magnetic interactions across an interface, resonant x-ray scattering will be employed as it can provide high resolution, magnetic sensitivity and element selectivity. As such, a regime must be created which varies only in the out-of-plane direction so that reflectivity techniques can be employed. If the polarising Fe is confined to a 2D layer in the plane of the sample, the polarised spheres produced by each atom overlap to form a polarising region without in-plane structure. If the Fe layer is confined within a layer of Pd, rather than at its surface, a number of additional benefits also arise. First, the volume of polarised Pd effectively doubles, as Pd above and below the Fe layer becomes polarised. Second, the number of interfaces is doubled, potentially enhancing any additional interface effects. Finally, the effect of the termination of the crystal lattice at the uppermost interface is removed from the magnetic region.

A semi-quantitative description of the induced polarisation [52] predicts an exponentially decaying Pd moment with increasing distance from the Fe layer in accordance with:

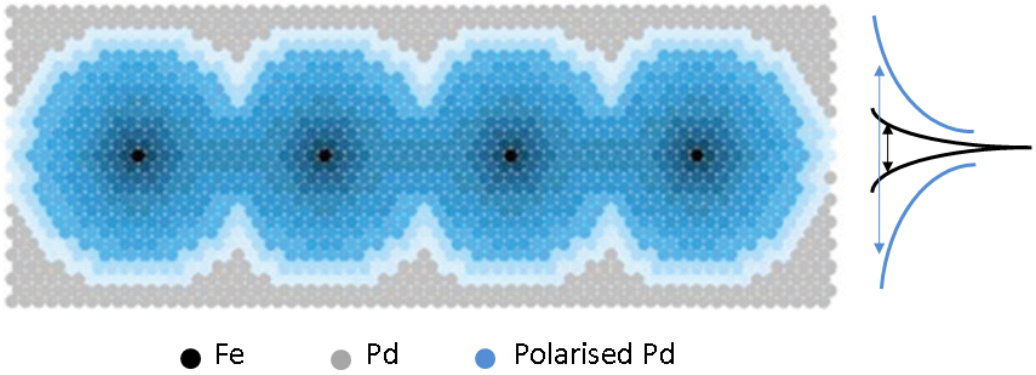

Figure 6.2: Modified from [119]. Spheres of polarised Pd form around Fe impurities. Further addition of Fe within the same 2D plane creates a polarised region varying only in the out-of-plane direction. The approximate distribution of Fe and Pd moments integrated in the in-plane direction are indicated.

$$\sigma_{\mathrm{S}}(r) \sim \chi_{\mathrm{P}} \frac{3k_F^2}{\pi r} \exp\left(-\frac{2k_{\mathrm{F}}r}{\sqrt{S/3}}\right), \tag{6.1}$$

as described in section 2.2.1. The extent of the profile is theoretically dependent only upon the Stoner factor, S. An approximate moment profile for a buried 2D Fe layer within Pd is therefore illustrated in figure 6.2.

FePd systems comprised of a buried Fe δ-layer, with thickness of the order of 1 ML, within nominally bulk Pd were therefore grown by the Material Physics group at Uppsala University. These samples were epitaxially grown on MgO (100) substrates using ultra-high vacuum DC magnetron sputtering [119]. A 100 ML thick Pd layer was deposited onto a 10 ML V seed layer before growth of a thin Fe layer (0.3, 0.5, 0.7, 1.1 and 1.4 ML). The samples were finally capped with a further 10 ML of Pd, which was intentionally left thin to allow XMCD via total electron yield. Immediately after growth, the temperature dependence of the magnetisation (not shown) was measured using the Magneto-Optical Kerr Effect (MOKE) in a longitudinal geometry. All samples showed a ferromagnetic response to applied field at 10 K with an ordering temperature that increased linearly with the amount of Fe in keeping with previous results [119].

6.2 Magnetic Profiles

In order to investigate the out-of-plane extent of the polarised Pd region, magnetic reflectivity can be employed. Using XRMS and altering the incident photon energy, to either the Fe or Pd L_3 edge, enables the magnetisation of the two different element species to be probed separately. The addition of PNR data enables the magnitudes of the moments carried by each sub-lattice to be normalised to each other. Data fitting was performed using the GenX fitting programme [94].

When fitting the magnetic profile, it is prudent to consider possible variations in profile shape. Magnetic interfaces have been shown to display a variety of interesting phenomena, such as enhanced or suppressed moments [97, 101, 121]. The work by Björck et al. [97] is of particular interest, as the enhancement of interfacial Fe moments was observed in FeCo superlattices (itinerant ferromagnetic systems).

The simplest profile shape to model is an exponentially decaying moment with increasing distance from the interface. From equation 6.1 it can be seen that this simple model is appropriate for the induced Pd moments. However, following the findings of Björck et al. [97], the inducing Fe moments may show more complex interfacial behaviour. To allow for the possibility of enhanced or suppressed interface moments, the GenX simulation has to have additional complexity added (allowing the profile to be broken into distinct magnetic regions) which introduced additional degrees of freedom. These additional degrees of freedom can provide too much flexibility during the early stages fitting process, making a robust fit more difficult to reach. Initially then, exponentially decaying profile shapes will be assumed for both Fe and Pd sub-lattices. Once the best fit is ascertained, the additional degrees of freedom will be added to see whether any improvements to the fit can be made.

Figures 6.3, 6.4 and 6.5 show the fitted simulations for the 1.4 ML and 0.5 ML Fe δ-layer thicknesses respectively, with exponentially decaying moment profiles assumed. An example of the corresponding structural profiles, which remained approximately invariant between samples, produced by the fit to the 1.1 ML data is shown in figure 6.6. The structural fitting parameters for all samples are given in table 6.1. Pd data were collected on the 4-ID-D beamline at the APS, Fe data on the X13A beamline at the NSLS, and neutron data on the CRISP instrument at the ISIS facility. The Pd edge XRMS and the PNR data were collected at 10 K, whereas the Fe data were collected at 30 K. No structural or magnetic change is expected over this temperature range. These data were collected in saturating fields of approximately 5 mT. At these temperatures, any change to the magnetisation due to a field of this size is expected to be minimal.

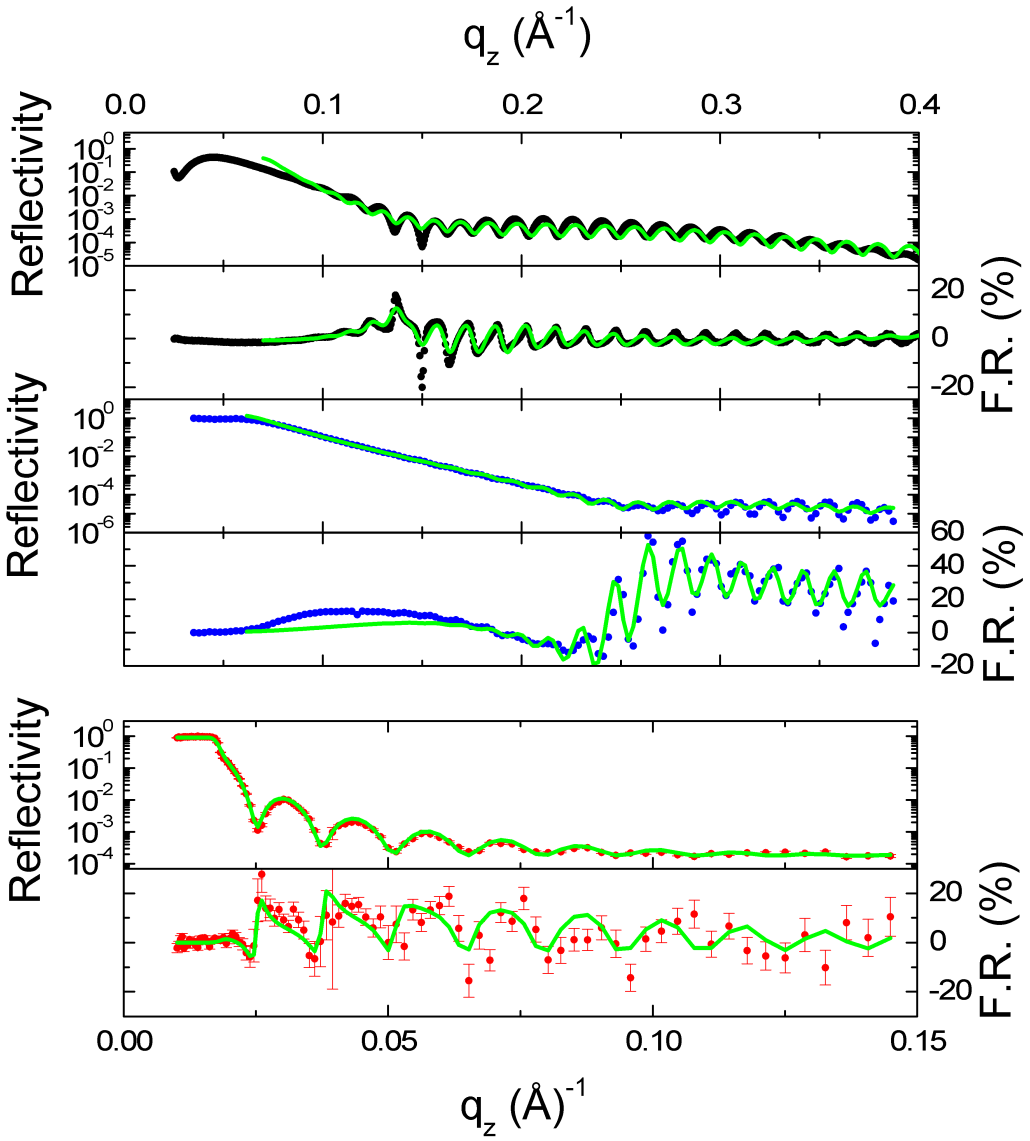

Figure 6.3: Upper panels show resonant x-ray reflectivity data, at the Pd (black) and Fe (blue) L_3 edges, from a 1.4 ML Fe δ-layer in Pd. Lower panels show polarised neutron reflectivity data (red) from the same sample. Data fitting performed using GenX (green) was used to extract the element specific magnetic profiles.

As each of these measurements was carried out at a different Central Facility, and the samples were stored and transported in air, some variation in surface oxidation between measurements is unavoidable. As such, though the data were all simultaneously fitted to a consistent sample structure, the surface oxidation (both thickness and roughness) was allowed to vary between fits. For each sample, the structural contribution to the total scattering at the Pd edge was fitted first to de-

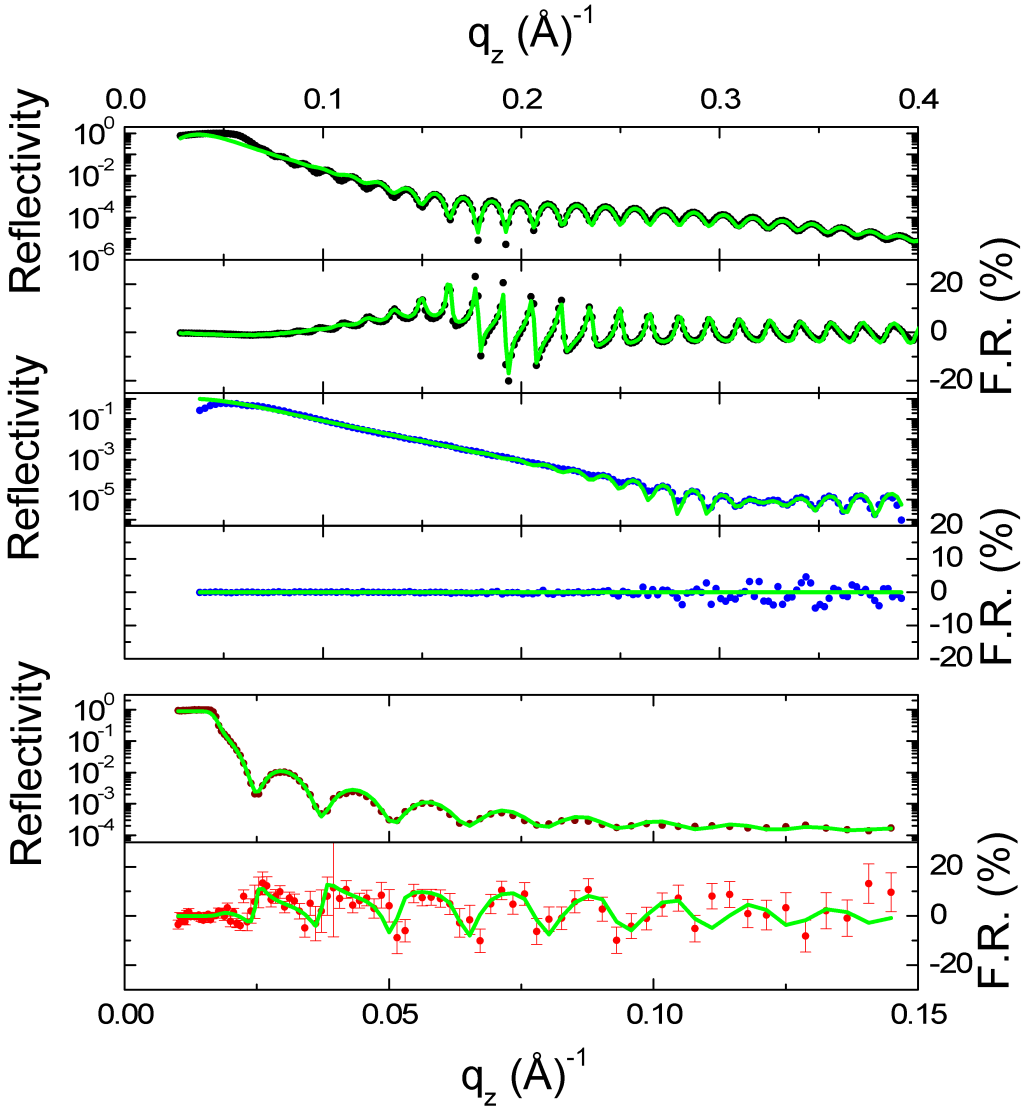

Figure 6.4: Upper panels show resonant x-ray reflectivity data, at the Pd (black) and Fe (blue) L_3 edges, from a 0.5 ML Fe δ-layer in Pd. Lower panels show polarised neutron reflectivity data (red) from the same sample. Data fitting performed using GenX (green) was used to extract the element specific magnetic profiles.

termine the sample structure. Subsequently, the magnetic contribution to the Pd edge scattering was introduced with additional parameters defining the magnetic profile shape. These terms defined the magnitude of the moment at the Pd-Fe interface, and a magnetic roughness terms which described the rate of falloff of the moment with increasing distance from the Fe layer. This defined the extent of the polarised region. Next, the Fe edge data were added. The structure was kept

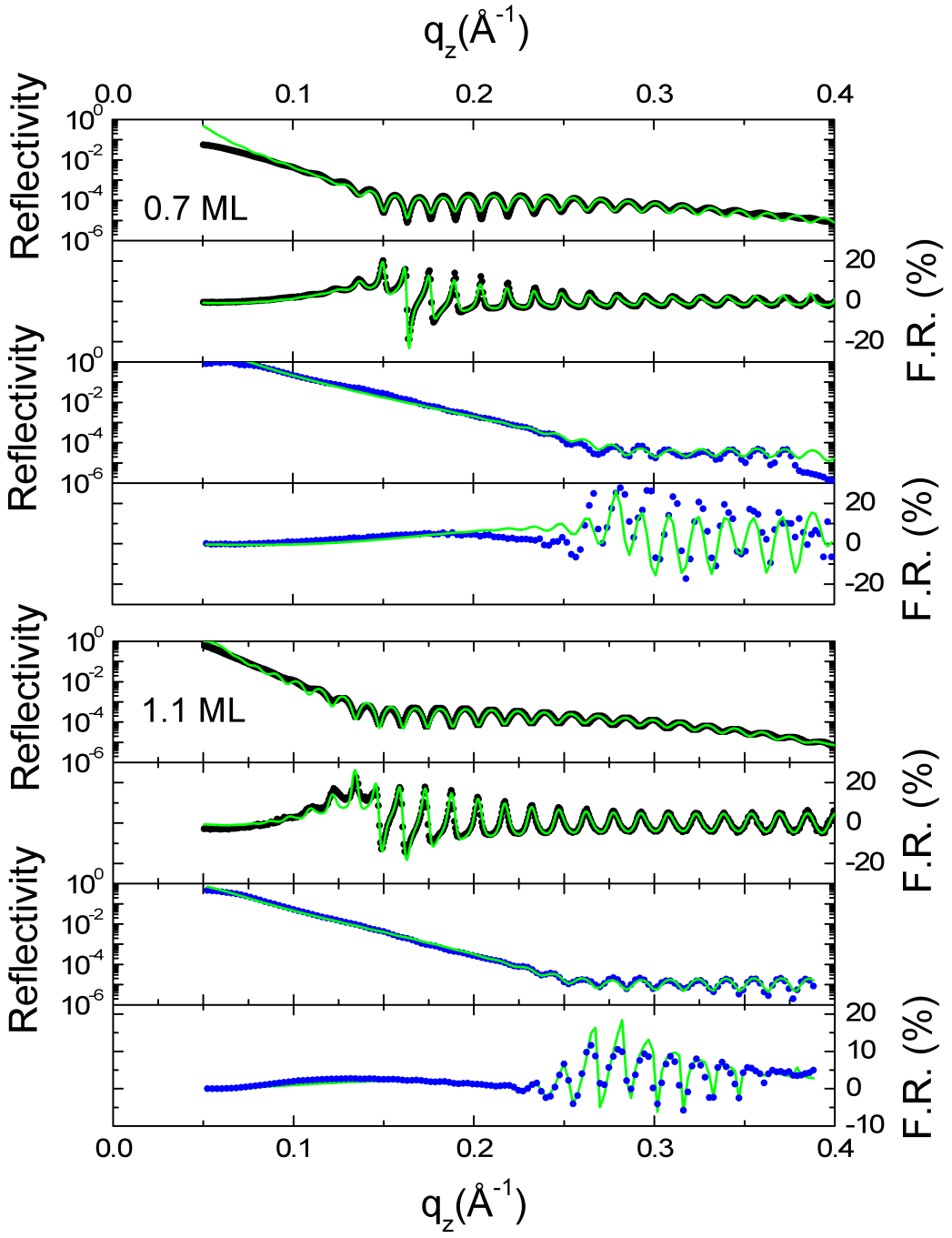

Figure 6.5: X-ray reflectivity data, at the Pd (black) and Fe (blue) L_3 edges, from 0.7 and 1.1 ML Fe δ-layers in Pd. Data fitting performed using GenX (green lines) was used to extract the element specific magnetic profiles.

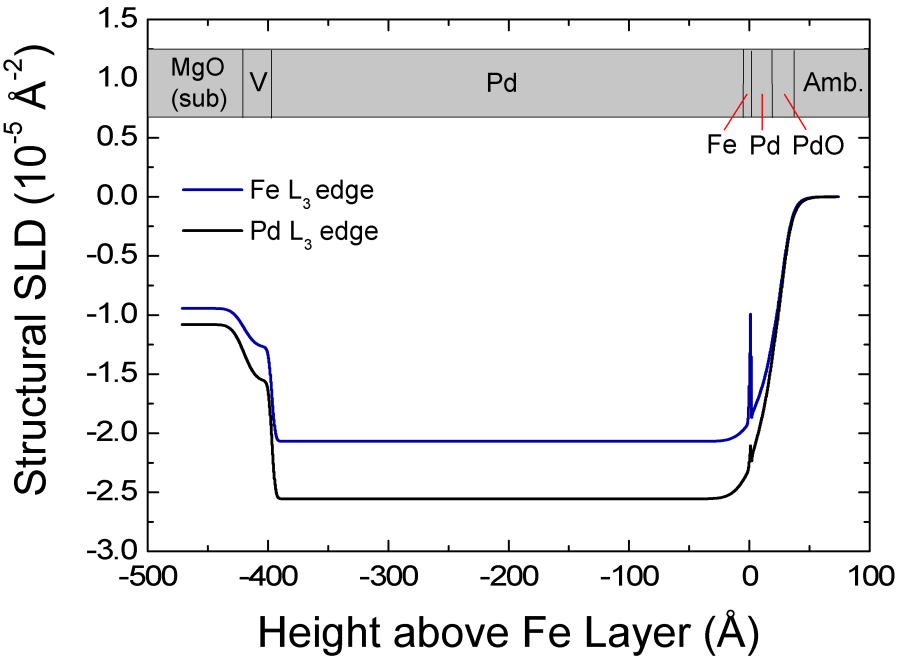

Figure 6.6: The scattering length density (SLD) as a function of depth showing the structural profile of the 1.1 ML trilayer at both the Fe and Pd L_3 edges. Differences between the profiles arise due to the energy dependence of the scattering factors. A corresponding schematic of the sample profile is included for clarity.

fixed while the structural and magnetic scattering terms were fitted along with instrument parameters (for example incident intensity). Finally the PNR data were added, where available, and the neutron instrument parameters fitted. At this point a final, global fit was performed with all available fitting simultaneously fitted to all available data set. Throughout the fitting process, individual fits to each data set showed some improvement in the quality of fit when compared to the simultaneous fit, highlighting possible differences in sample structure. This is likely due to the measurements being taken at different positions on the sample surface. The overall fit contains some structural compromises to give the overall best fit possible while ensuring consistency between simulations. Low angle data at the Pd edge were not included in the fit as the detector was saturated, adversely affected the data.

Immediately evident in figure 6.4 is the zero moment carried by the Fe atoms in the 0.5 ML film. As no magnetic signal was observed at any energy, or at any q_z, it was not possible to optimise the scattering conditions to maximise the observed F.R., as is usually the case. Instead, the data were collected under the same conditions

		MgO	V	Pd Lower	Fe	Pd Upper	PdO
1.4 ML	Thickness (Å)	-	13.0	397.7	2.6	21.2 (14.0)	26.3 (23.3)
	Roughness (Å)	8.4	3.0	1.2	1.5	15.0 (12.1)	8.2 (5.2)
1.1 ML	Thickness (Å)	-	23.1	397.6	0.7	10.8 (11.0)	13.9 (13.8)
	Roughness (Å)	7.9	2.3	1.0	0.0	14.7 (14.1)	6.3 (6.6)
0.7 ML	Thickness (Å)	-	19.1	389.4	0.7	9.0 (12.4)	14.0 (10.5)
	Roughness (Å)	1.3	2.1	0.1	0.1	15.27 (5.4)	10.1 (6.2)
0.5 ML	Thickness (Å)	-	19.0	392.3	0.7	9.6	12.4
	Roughness (Å)	3.0	3.3	0.1	0.0	14.9	5.5

Table 6.1: Structural parameters from the GenX fits, shown in figures 6.3, 6.4 and 6.5. Values in brackets indicate separate parameters used only in the Fe edge fits to accommodate changes in sample oxidisation between experiments.

as the 1.4 ML sample. This remarkable result will be discussed in more detail in section 6.3. The periodicities of the fringes in the magnetic data, i.e. the F.R.s, are controlled by the width of the magnetic profiles. As the periodicity fits well across all the data, the distribution of the magnetic moments can be confidently extracted. Similar XRMS data were recorded, and fits were produced, with Fe δ-layer thicknesses of 0.7 and 1.1 ML without the advantage of the additional PNR (see figure 6.5).

As discussed earlier, there are various examples in the literature of magnetic moments becoming enhanced or suppressed at material interfaces [97, 101, 121]. These studies highlight the need for careful consideration of the profile shape within the simulation procedure. As such a variety of profile shapes with enhanced or suppressed interfacial Fe moments were tested as possible improvements to a simple exponentially decaying moment. GenX conveniently includes fitting parameters to define a modification to the magnetic moment at a material interface. These additional modifications requires additional flexibility to be introduced. This is achieved by modeling the Fe layers closest to the interface as independent slabs of variable thickness. Using this extra freedom, a comparison between different profile shapes, shown in figure 6.7, was conducted using the Fe edge data from the 1.1 ML sample. The fitting in this comparison was performed without the influence of the Pd edge or neutron data to allow the greatest freedom possible and maximise the sensitivity to the Fe edge profile. All structural and Fe edge resonant parameters were tied to those of the initial fit shown in the lower panels of figure 6.5.

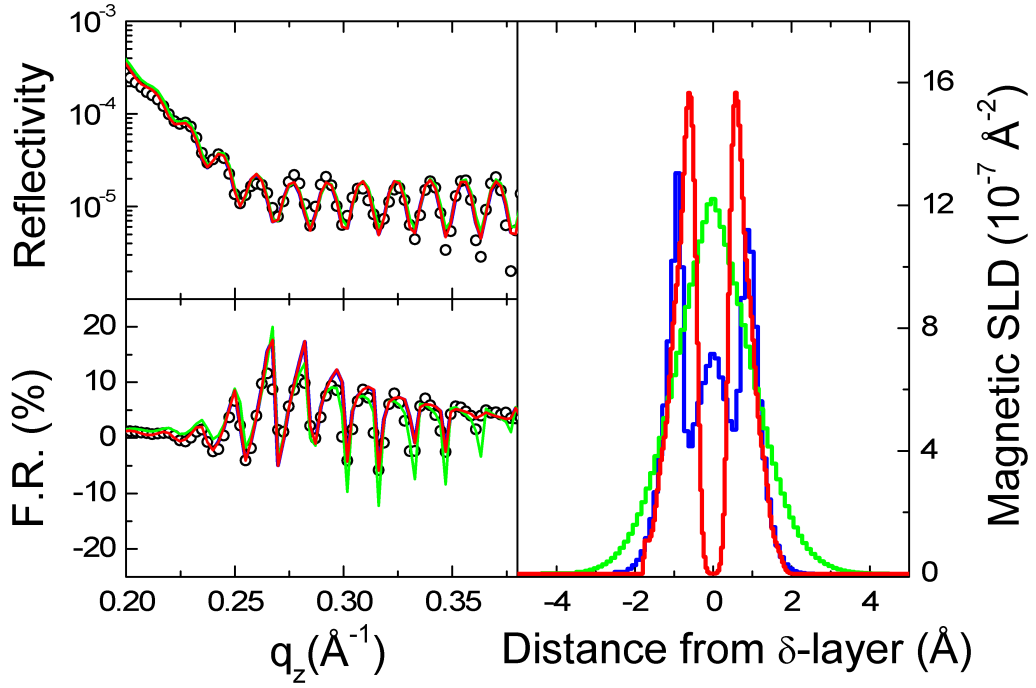

Figure 6.7: The effect of a changing magnetic magnetic profile shape (right panel) on the Fe edge magnetic reflectivity (left panels) from a 1.1 ML Fe δ-layer in Pd. Fits and profiles carry corresponding colours. No significant change to the quality of fitting is observed between profile shapes; the modification of interface moments can not be proven.

The three profiles showed no significant change in the overall quality of fit in the reflectivity data. The data are most sensitive to the profile width and integrated area which remain approximately constant. The slice depths used for the fits was substantially lower than the 1 ML suggested by Tonnerre as a limit beyond which improvements to the quality of fitting are unlikely [96]. This computationally intensive modification was made in an attempt to increase the sensitivity to the profile shape. However, due to the inverse nature of reciprocal space, features with a real space extent smaller than the profile width, i.e. those defining the modified interface moment, require reflectivity data extending to a significantly higher q_z range to be accurately resolved. This was not experimentally possible due to diffractometer limitations. Given the available data, it must be assumed that there is no modification to the interface moment; an assumption that subsequent experiments may disprove. The magnetic profiles, as a function of Fe thickness, from simulations without modifications to the interface moments, extracted from the reflectivity fitting in figures

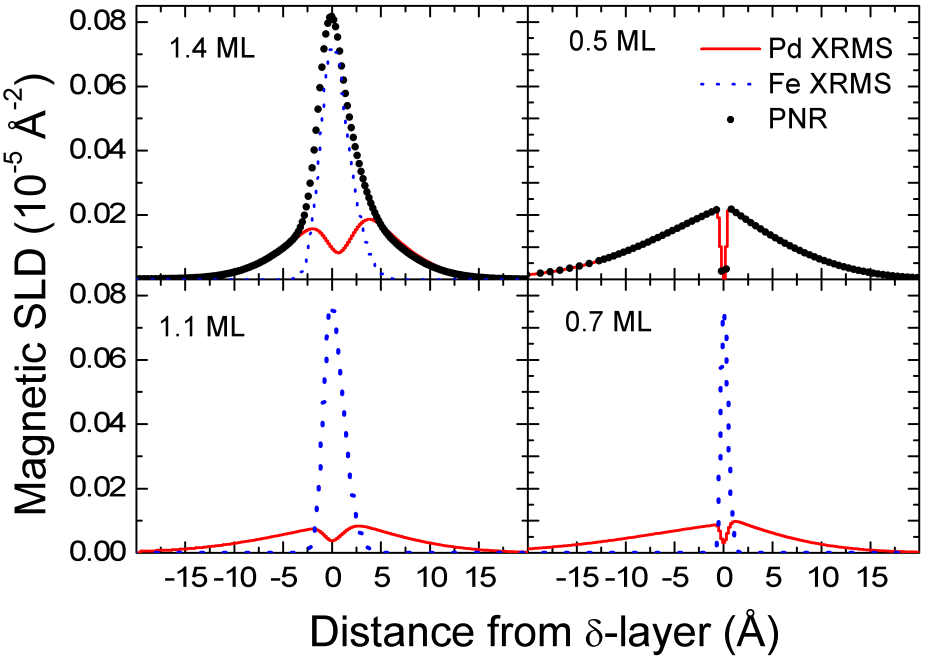

Figure 6.8: The magnetic scattering length density (SLD) as a function of depth showing the distribution of element specific magnetic moments for a varying Fe δ-layer thickness in a Pd/Fe/Pd trilayer at 10 K (Pd and PNR) or 30 K (Fe).

6.3, 6.4 and 6.5, are shown in figure 6.8.

The slight broadening of the Fe distributions above the layer thicknesses expected is likely due to interface roughness. The distribution is, however, still consistent with the Fe moments being confined within the Fe sub-lattice. The extent of the Fe moment diminishes as the thickness reduces, until the moment vanishes for the 0.5 ML case. The Pd moments have approximately equal extents from the δ-layer irrespective of the Fe thickness. The moments decay approximately exponentially in magnitude with increasing distance from the layer, however the limited resolution available due to the lack of data at higher q_z values makes the exact decay profile impossible to determine with greater accuracy.

The magnitude of the Pd moments falls into two regimes, a large moment in the 0.5 and 1.4 ML samples, and a reduced moment in the 0.7 and 1.1 ML samples. This can be rationalised by considering the Fe roughness. An ideal δ-layer with 1 ML thickness can be considered to have no roughness; it is atomically perfect. Below 1 ML, an incomplete layer is formed with a fractional occupancy described by the thickness of the layer. An illustration of different occupancies is

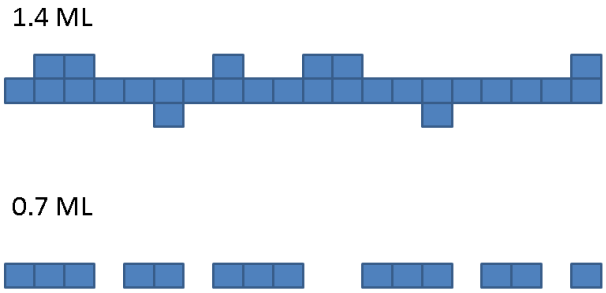

Figure 6.9: Incomplete layer coverage associated with fractional monolayers illustrated in the 1.4 and 0.7 ML regimes. Areas with greater and lesser concentrations of Fe have a discrepancy in T_C producing a broadening of the magnetic ordering response.

given in figure 6.9. Even in an ideal case, a non-integer monolayer regime clearly has structural roughness. With all other conditions being equal, the roughness of a layer is therefore minimised at 1 ML and maximised at 0.5 and 1.5 MLs. The roughness of the Fe layer in an FePd trilayer is proportional to the surface area of the interface. As this surface area increases, so too does the degree of hybridisation of the electron bands at the interface. This leads directly to an increase in the magnitude of the induced Pd moments.

6.2.1 Temperature Dependence

Though the extent of the induced moment profile does not change with Fe δ-layer thickness, it is likely to evolve with changing temperature. It is expected that, at a given temperature, the magnitude of the moment will decay exponentially in accordance with equation 6.1. Within this description, only the Stoner enhancement factor, S, is temperature dependent. S is defined as the ratio between the magnetic susceptibility and the Pauli susceptibility i.e $S = \chi/\chi_P$. χ_P is a material constant meaning S varies only with χ. The Pd susceptibility reduces linearly as a function of increasing temperature [122], causing S to reduce accordingly. The induced profile extent is therefore predicted to narrow as the temperature is increased. A lack of higher temperature reflectivity data from these samples prevents a direct examination of this expectation at this time, but an indirect confirmation can be procured from observations of the magnetic susceptibility of the polarised region.

The measured magnetic susceptibility peaks sharply at the ordering temperature of the material [24], as even a minute field is sufficient to realign the disordered

moments. In a system with a uniform magnetic profile, in which the whole sample volume undergoes the order-disorder transition at the same temperature, a uniform susceptibility as a function of temperature is expected until this sharp peak at T_C occurs. If, however, the polarised region narrows, the outermost regions (i.e. those furthest from the Fe layer) are effectively undergoing magnetic ordering at a lower temperature than those in the innermost regions, likely leading to a change in the susceptibility as a function of temperature. In order to isolate the effect of a changing profile shape on the magnetic susceptibility, a comparison to a material with a uniform magnetic profile is needed. The simplest geometry to use is an FePd alloy material with a uniform distribution of Fe atoms.

A FePd alloy sample, with an Fe concentration of 5% was used for this study. This alloy film was sputtered directly onto a naturally oxidised Si substrate with a target thickness of 500 Å. Layer thicknesses during growth are controlled by shutter timing and are expected to be within 10% of intended values. The alloy sample was stored and transported in air, and so an oxide thickness of several nm is expected. This thickness is included as a free parameter during the fitting process and was determined to be 2(1) nm.

Magnetic reflectivity data were collected at the Pd L_3 edge to verify the uniform magnetisation expected throughout the alloy sample. The data and resulting fits, generated using GenX [94], are shown in figure 6.10. The simulation, fitted assuming a uniform magnetic profile, shows excellent correlation with the data. The lower alloy interface (SiO/FePd) shows a sharp magnetic transition due to the low structural roughness ($\approx$ 1 Å). The upper interface (FePd/PdO) shows a slight broadening of the profile shape as the Pd atoms in closest proximity to the unoxidised alloy carry a residual moment. The uniform magnetisation shown throughout the full volume of alloy material makes this system an ideal comparator for the trilayer, as it allows a direct comparison of the alloy and trilayer susceptibilities in order to investigate the temperature dependence of the profile shape.

The magnetic susceptibility, χ, is defined as $\chi = dM/dH$, and so the magnetisation as a function of field must be measured. Hysteresis loops were therefore collected as a function of temperature, for both alloy and trilayer materials, and fitted using the methodology outlined in section 2.3.2. Examples of hysteresis loops from this process are shown in figure 6.11. The data shown are at corresponding fractions of T_C in each sample, and yet show considerable differences in shape. Between 0.8 and 0.95 T_C, the alloy displays a square loop with an invariant shape but a significant reduction in moment. This indicates a gradual reduction in moment as T_C is approached, with little change in the susceptibility. The trilayer system

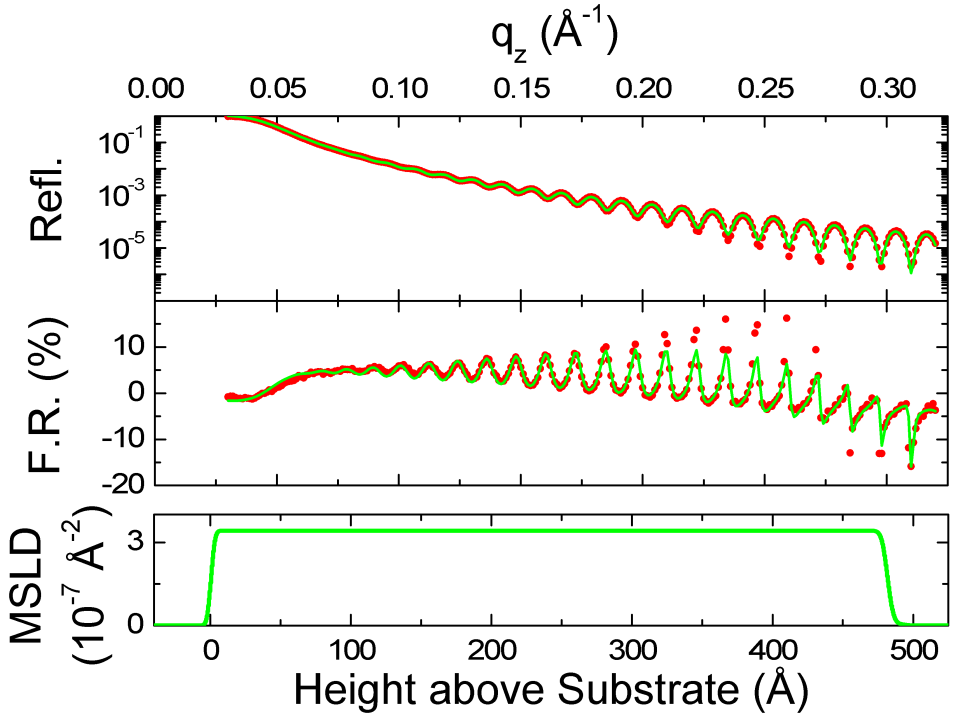

Figure 6.10: Upper panels show the structural (reflectivity) and magnetic (F.R.) contributions to the magnetic x-ray reflectivity (points) of a 5% FePd alloy. Data were collected at 10 K at the Pd L_3 edge with the incident photon polarisation reversed at each point. The GenX simulation (line), and resulting magnetic scattering length density profile (lower panel), shows uniform magnetisation throughout.

shows a more rounded loop shape even at 0.8 Tc. A large susceptibility is therefore expected well below T_C. The relatively small reduction in moment over this temperature range indicates a system with reduced spin dimensionality which will be studied in more detail in the following section.

The derivatives of the hysteresis loops at $H = 0$ were calculated analytically from their arctan fits, producing the results shown in figure 6.12. As the F.R. is a dimensionless quantity proportional to the sample magnetisation, the magnitudes of the calculated susceptibilities can not be meaningfully compared. For convenience, the susceptibilities presented in figure 6.12 have therefore been normalised so that the maximum recorded susceptibility is equal to 1.

The alloy susceptibility, at the Pd edge (black circles figure 6.12), shows no temperature dependence below T_C. This typifies a uniform FM regime; the increase in temperature gradually reducing the magnetisation uniformly throughout the sample. The breaking of the magnetic coupling at T_C leads to a sharp spike in the

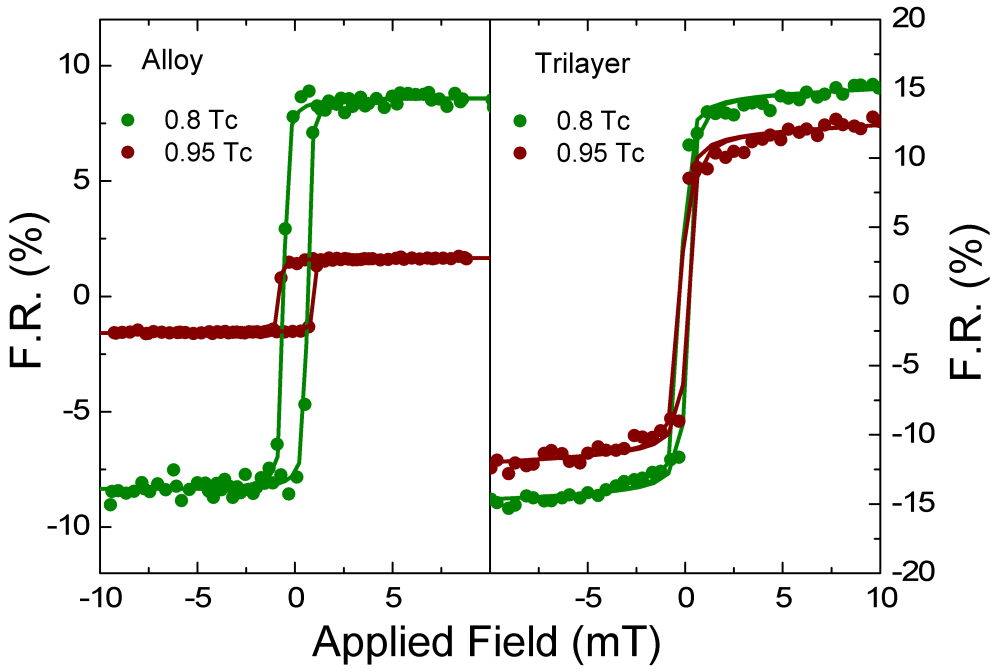

Figure 6.11: Left and right panels show Pd edge hysteresis loop data (points) fitted to pairs of arctan functions (lines) for 5% FePd alloy and 0.7 ML FePd trilayer films respectively. Temperatures are given as fractions of T_C, where T_C(Alloy) = 267.5 K and T_C(Trilayer) = 117 K.

susceptibility as the disordered moments realign to the externally applied field. If a comparison is made to the susceptibility of the Pd moments in the FePd trilayers (red circles figure 6.12), the behaviour is very different. As T_C is approached, a gradual increase in the susceptibility is observed, which peaks well below T_C. This is indicative of the predicted narrowing of the induced moment profile. As the outermost regions undergo magnetic ordering at temperatures well below T_C, the susceptibility is enhanced. Furthermore, as the susceptibility is always evolving, unlike the constant susceptibility as a function of temperature seen in the alloy, a continual evolution of the profile shape with temperature can be inferred.

These results are consistent with a description of a polarised magnetic region with an extent described by equation 6.1. The extent of the profile is independent of Fe δ-layer thickness, proving that a change in spatial extent of this region is not responsible for the observed crossover in spin dimensionality. To elucidate the origin of the crossover, the element specific magnetic ordering must be studied.

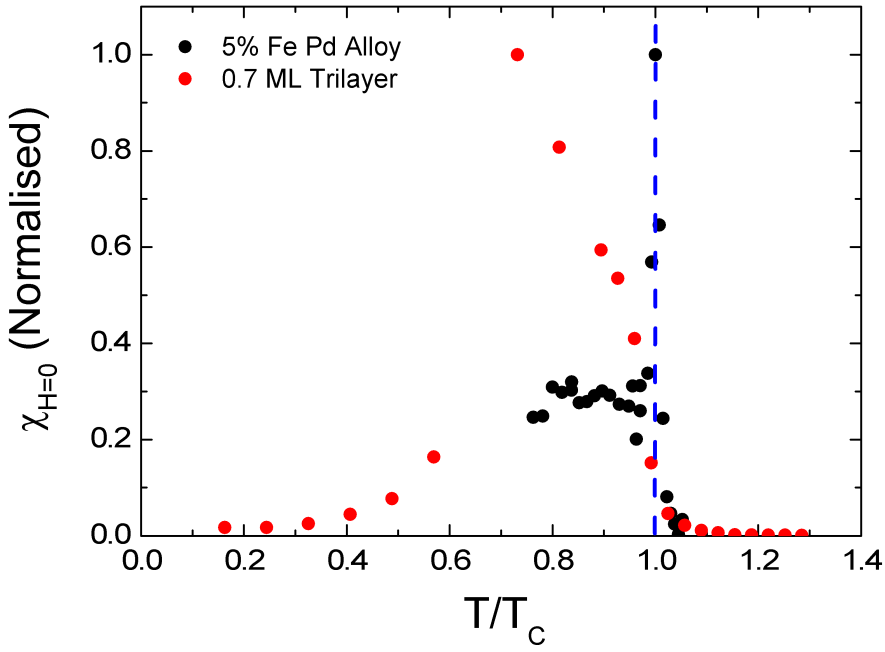

Figure 6.12: A comparison between the zero-field magnetic susceptibilities of a 5% FePd alloy and a 0.7 ML FePd trilayer. The alloy material displays a uniform susceptibility with a sharp peak at T_C (broken line) indicative of a uniform loss of the magnetic moment throughout the sample. The broad susceptibility peak displayed by the trilayer characterises a narrowing polarised region. Temperatures are given as fractions of T_C, where T_C(Alloy) = 267.5 K and T_C(Trilayer) = 117 K.

6.3 Magnetic Ordering

The dimensionality crossover observed in MOKE studies [119], is attributed to an observed linear increase in T_C with increasing Fe δ-layer thickness. The study further supposed that this increase in T_C, caused by the increase in the magnetic coupling strength on the two sub-lattices, allows shorter range, higher energy excitation modes to be accessed in the out-of-plane direction leading to an increase in the number of spin degrees of freedom available. It is expected that the direct coupling between these sub-lattices will be manifested in the element specific ordering as identical behaviour.

Pd/Fe/Pd trilayers, with Fe δ-layer thicknesses of 0.5, 0.7, 1.1 and 1.4 ML, were examined. Hysteresis loops as a function of temperature, examples of which are shown in figure 6.13, were collected using XRMS at the Fe and Pd L_3 edges from which the element specific magnetic ordering behaviour could be determined. The

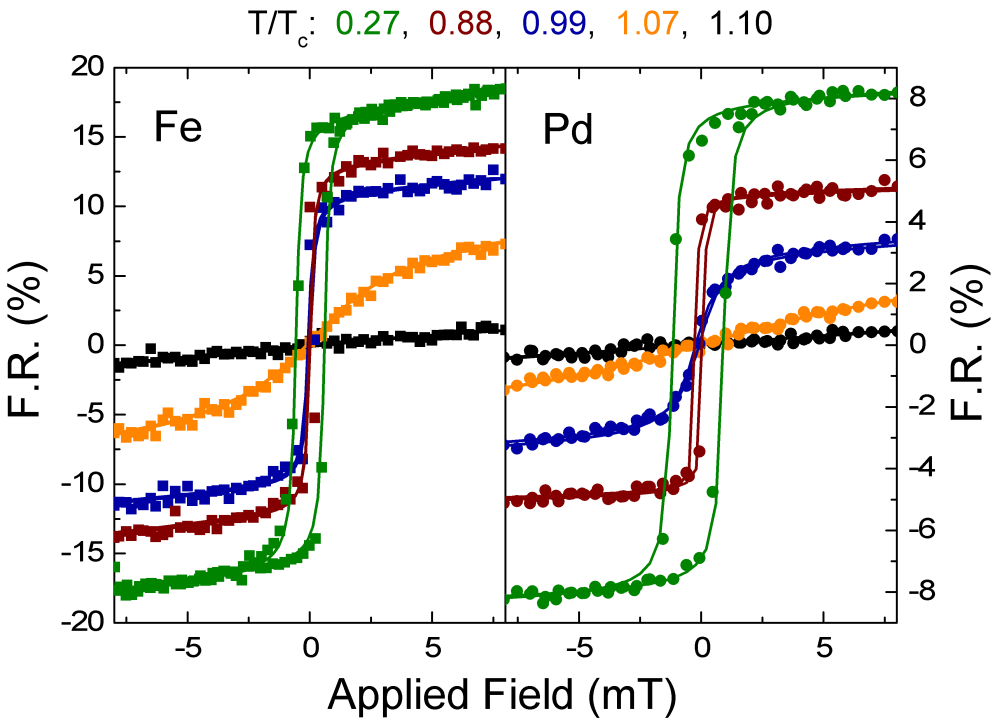

Figure 6.13: Left and right panels respectively show Fe and Pd edge hysteresis loops from a 1.4 ML Fe δ-layer in Pd. The clear differences in shape as T_C is approached are indicative of sub-lattices with differing dimensionalities.

Pd edge data were collected using the 4-ID-D beamline at the Advanced Photon Source, and the Fe edge data using the X13A beamline at the National Synchrotron Light Source. Each data set was collected at a fixed point in q_z chosen through iterative optimisation of the incident energy and angle to maximise the observed F.R. at base temperature (Pd $\approx$ 10 K, Fe $\approx$ 30 K). By maximising the F.R., the greatest signal to noise ratio was achieved. At the Pd edge, this process provided the further advantage of tuning the sensitivity to the point of maximum magnetisation in the sample i.e. the Pd layers closest to the Fe. Due to the non-zero coercivity in the applied magnetic field, the magnetisation, M, was extracted from the Hysteresis loops at a field value of 0.1mT. A typical example of the magnetisation as a function of temperature, as extracted from the hysteresis loops of the 0.5 ML sample, is shown in figure 6.14.

The data show a significant tail above T_C which is partially due to non-zero applied field inherent in the electromagnet. However, as an Fe layer with sub-monolayer thickness is a randomly distributed layer of incomplete coverage with a fractional occupancy defined by the "thickness" of the layer, a significant addi-

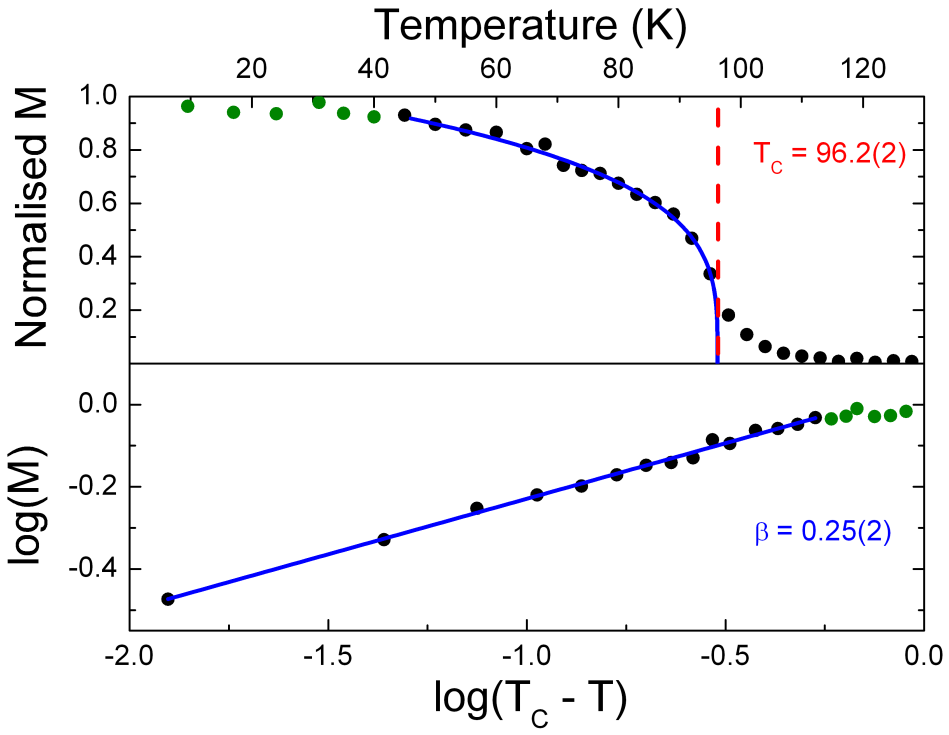

Figure 6.14: The magnetic ordering behaviour of Pd moments from a 0.5 ML Fe δ-layer in Pd. The blue line is a linear least squares fit to the log-log data (lower panel) additionally translated onto the linear scale (upper panel) for illustrative purposes. Lower temperature data are not included in the fit as the data deviate from critical behaviour.

tional contribution to the tail will arise. Inherent imperfections in the distribution of Fe atoms in such a sub-monolayer regime produce areas with increased separation and decreased coupling strength between adjacent moments (see figure 6.9). This leads to a broadening of the distribution of ordering temperatures in the Pd. These finite-size effects are an unavoidable complication. It is expected, however, that this deviation from the critical behaviour will only become significant above T_{C}, which was determined from log-log analysis (lower panel figure 6.14) by maximising the region over which the linear trend holds. The point of inflection between the regions dominated by the intrinsic moment and the field induced moment denotes a good approximation of T_{C}, confirming this hypothesis. The low temperature data, denoted in green, are not used to perform this analysis. The magnetic ordering exponent acquired, $\beta_{eff} = 0.25(2)$, correlates to that expected from a 2D-XY system, and is in agreement with previous MOKE studies [119]. This verifies the assumption that the giant Pd moment dominates the total moment and therefore that the MOKE

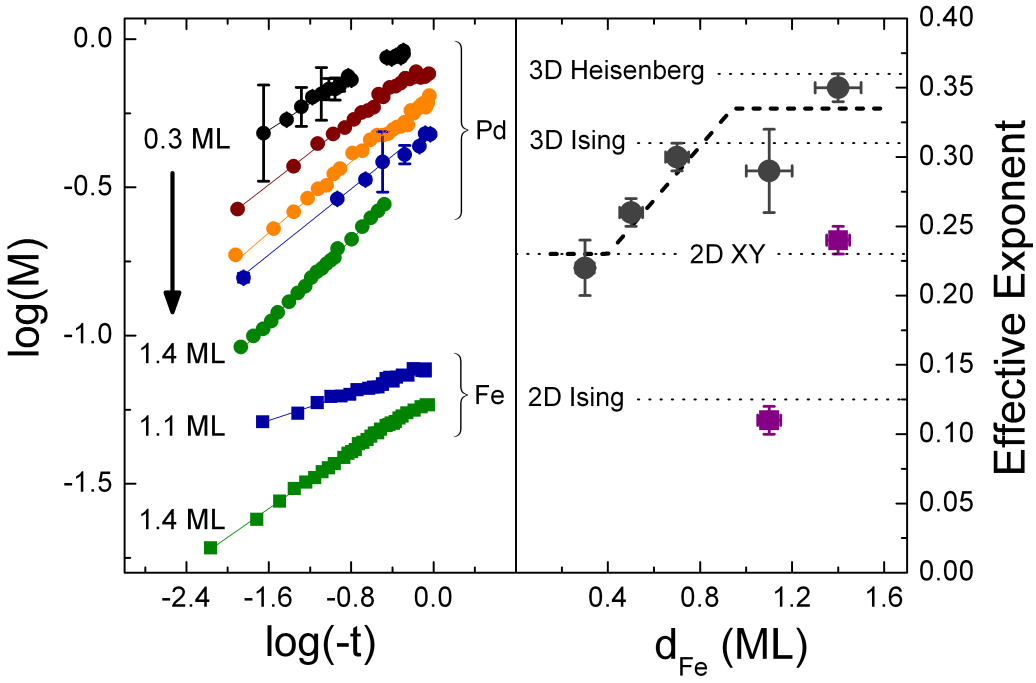

Figure 6.15: Power-law scaling behavior of the two magnetic sub-lattices as a function of reduced temperature (left) with data offset for clarity. Effective scaling exponents as a function of Fe thickness (right). The Pd exponents (black circles) closely follow the exponents determined using MOKE [119] (broken line). The Fe exponents (purple squares) could only be measured for samples with an Fe thickness $\geq$1 ML.

data follow the behaviour of the Pd sub-lattice. The results of similar magnetic ordering analysis, performed on the magnetisation as a function of temperature from both Fe and Pd sub-lattices, are displayed in the left panel of figure 6.15. The right panel of this figure shows the extracted scaling exponents as a function of δ-layer thickness.

Few usable loops were obtained for the 1.1 ML sample. The low point density available in the near T_C region makes an accurate assessment of T_C impossible. This uncertainty in T_C is amplified in the uncertainty of β_{eff}. However, if the right panel of figure 6.15 is examined, the difference in scaling behaviour between the Fe and Pd moments remains clear. The crossover in spin dimensionality observed in the MOKE data [119] is matched by the Pd moments: an apparent transition from 2D to 3D behaviour is observed as the Fe δ-layer thickness is increased from 0.5 to 1 ML. This behaviour meets the expectation that the giant moment carried by

the large polarised Pd region is sufficient to dominate the total moment measured using MOKE. The Fe moments show a different transition from 2D Ising to 2D XY behaviour between 1.1 and 1.4 ML. For an Fe thickness of 0.7 ML, although magnetic signal was measured, the coercivity remained zero over the entire range of accessible temperatures. The remanent moment is then zero at all temperatures, and no ordering exponent can be extracted. At an Fe thicknesses of 0.5 ML, no magnetic signal was carried by the Fe moments, which will be discussed in section 6.4. However, the pronounced difference in ordering behaviour between the Fe and Pd sub-lattices with larger Fe thicknesses suggests that the two sub-lattices are not directly coupled, i.e. the dimensionality of the Pd lattice is not tied to that of the Fe lattice. This implies that the strength and nature of the magnetic coupling within the sub-lattices are independent. This result addresses one of the primary aims of this work. The hypothesis proposed by Pärnaste in [119] suggested the dimensionality crossover was driven by a simple T_C driven change in the available spin degrees of freedom. This was proposed under the assumption that as the Fe thickness, and so coupling strength (T_C) in the Fe sub-lattice increased, so too did the coupling strength in the Pd sub-lattice. These element specific magnetic ordering data clearly contradict this hypothesis.

6.3.1 Origin of the Dimensionality Crossover

As proven in section 6.2, the range of the induced moments does not change with Fe layer thickness. A truncation of the magnetic lattice with reduced Fe layer thickness cannot then be responsible for the observed dimensionality crossover. The results of the element specific magnetic ordering studies showed that the alternative hypothesis of a T_C driven origin could also not be responsible for the observed crossover. Further analysis of the magnetic ordering data can, however, rationalise these unexpected observations.

The origin of the observed difference in apparent ordering dimensionality between the Fe and Pd moments can be accounted for by considering the origin of the Pd magnetisation. The 0.5 ML case provides a excellent opportunity to study the Pd moments in the absence of any apparent influence from the Fe magnetisation. Under these conditions, the Pd moments show 2D XY behaviour with an ordering temperature $\approx$ 100 K. As the Fe thickness is increased, the Fe moments become ordered. This provides an additional contribution to the Pd moment, analogous to collecting the magnetic ordering data in the presence of an external field. This paramagnetic contribution acts on the Pd through the Pd susceptibility, χ, in accordance with $M = \chi H$. In this case, H, the internal field, is proportional to the magnitude

of the Fe moment, $Fe(T)$. The measured Pd moment is therefore composed of the sum of the FM and PM contributions:

$$Pd_{meas}(T) = Pd_{FM}(T) + A\left(\chi_{Pd}\left(T\right).Fe(T)\right), \tag{6.2}$$

where A is a proportionality constant. Unfortunately, the relative magnitudes of the Fe and Pd moments are impossible to determine with this technique. The measured F.R. depends critically on the q_z position and beamline optimisation (e.g. photon polarisation). Conveniently, however, the 1.4 ML sample provides a system in which this dependence can be verified. The 2D-XY behaviour of the Fe moments, $Fe(T)$, is proportional to the 2D-XY behaviour of the FM contribution to the Pd moments, $Pd_{FM}(T)$. As such, dividing both sides of equation 6.2 by $Fe(T)$ yields

$$\frac{Pd_{meas}(T)}{Fe(T)} = B + A\left(\chi_{Pd}\left(T\right)\right), \tag{6.3}$$

where B is a constant defined by the relative magnitudes of the Fe and Pd moments. The ratio of the measured Fe and Pd moments should therefore have a temperature dependence which only varies with the temperature dependent susceptibility of the Pd, $\chi_{Pd}\left(T\right)$. Experimental determination of the susceptibility of Pd has shown it to decrease linearly with increasing temperature above $\approx 100\ K$ [122]. The normalised Fe and Pd moments as a function of temperature for the 1.4 ML sample are therefore compared in figure 6.16. The inset on the same figure shows the ratio of the two measured moments.

In the critical region, the ordering behaviour, determined from log-log analysis, is used to calculate the Pd/Fe ratio designated by the solid lines in both the main figure and correspondingly in the inset. In the $0.2 \leq T/T_{\mathrm{C}} \leq 0.7$, the critical behaviour no longer holds and so polynomial fits to the data were employed (broken lines). Below $T/T_{\mathrm{C}} \leq 0.2$ analysis was not performed as the magnitude of the moments depends strongly on the extrapolated $T = 0$ value. The Pd/Fe ratio displays a linear gradient over the temperature range $0.2 \leq T/T_{\mathrm{C}} \leq 0.8$, with the normalisation of the measured moments causing the ratio to arbitrarily intersect $T = 0$ at 1.

The linearly decreasing ratio between the measured Fe and Pd moments with increasing temperature correlates with the linear decrease of the Pd susceptibility [122], making this model of the Pd behaviour a plausable solution. The crossover in magnetic ordering dimensionality is therefore not indicative of a true change in the available spin degrees of freedom. Instead, it is an apparent change caused by a modification of the inherent 2D-XY behaviour of the Pd by the variable influence

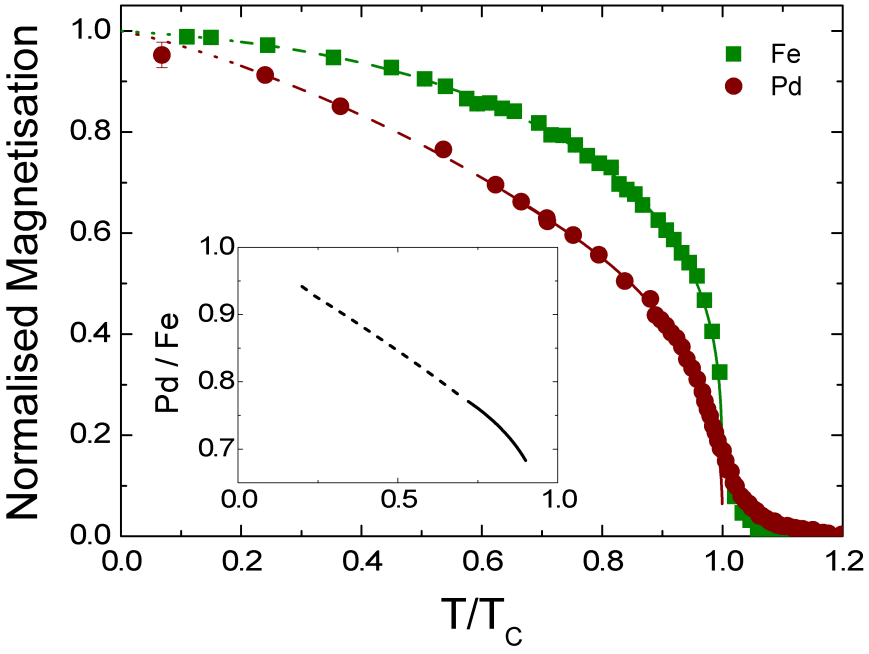

Figure 6.16: Normalised magnetisation of the Fe (squares) and Pd (circles) sub-lattices for the 1.4 ML Fe sample as a function of T/T_C. The best fit to an effective critical exponent is shown by solid lines with the low temperature behavior parameterised by a polynomial (broken line). Inset: Ratio of the two fitted curves shows a linear dependence with normalised temperature over the range $0.2 \leq T/T_C \leq 0.8$.

of the paramagnetic contribution from the Fe.

The dimensionality of the Fe showed a transition which was unexpected. Studies of Fe films on Au(100) [98] examined Fe thicknesses from 1-3 ML and showed 2D-XY behaviour independent of film thickness. The 2D-Ising behaviour observed at an Fe thickness of 1.1 ML, the smallest observed thickness at which spontaneous ferromagnetic order existed on the Fe sub-lattice, is close to the lower thickness limit examined in the former work. It is likely that, due to crystallographic differences, a similar transition may have occurred in Fe/Au outside of the examined range. Similarly, it is likely that the invariance of the dimensionality observed in the Fe/Au system would be observed in the FePd trilayers, if the Fe thickness was increased. The behaviour of both the Fe and the Pd sub-lattices is therefore likely to remain constant upon further significant increases to the Fe δ-layer thickness. The expected continuation of the observed linear increase in T_C creates a regime in which the order-disorder transition will be significantly above room temperature, making this

supposition difficult to confirm without a change to the experimental technique.

These complex interactions across a magnetic interface highlight our poor understanding of the fundamental interaction of atomic moments. The dimensionality of the induced moments is not influenced by the inducing dimensionality. Instead, the observed dimensionality crossover in the Pd sub-lattice is an artifact of the indirect coupling of the two sub-latices via the Pd susceptibility.

6.4 Ultrathin Fe Moment

Below an Fe δ-layer thickness of 1 ML, the spontaneous Fe moment in a Pd/Fe/Pd trilayer was seen to vanish. A similar effect has been observed in Ni films below a thickness of approximately 2 ML [123]. It was supposed that this phenomenon resulted from the overlap of the Ni conduction electron bands with bands from the non-magnetic substrate. The itinerant electrons from the substrate diffuse into the conduction band of the Ni film, the high electron density of states (DOS) within this band will then be sufficient to generate FM order. As the film thickness reduces, however, fewer Ni nuclei are acting upon the diffusing conduction band electrons and so their influence becomes weaker and the DOS is reduced. At some critical thickness, the DOS within the Ni is no longer sufficient to preferentially align the electron spins and the FM order is lost. In the FePd trilayer, the overlapping Fe and Pd bands, which lead to the spontaneous magnetisation in the Pd sub-lattice, are therefore seen as a likely cause for the observed lack of Fe moments within these trilayer systems as a depolarising effect is conversely induced in the Fe.

A band hybridisation model suggests the FM response should be progressively lost as the δ-layer thickness is reduced until a critical point is reached where the moment vanishes. The lack of remanent moment, but retention of a saturation moment, in the 0.7 ML regime, could represent a system at this critical point in which no nett moment is present but a strong paramagnetic response is still prevalent. The 0.5 ML case then represents a regime below this critical thickness. More detailed observations of the behaviour of the Fe moments in the 0.5 and 0.7 ML samples were made to investigate this hypothesis.

Figure 6.17 shows total electron yield data of the XMCD as a function of energy from the 0.5 and 0.7 ML samples, with the inset showing the magnetic response to an applied field as a function of temperature in the 0.7 ML sample. The customary optimisation technique of maximising the F.R. by successively altering q and E could not be employed for the 0.5 ML sample as no F.R. could be recorded. The 0.5 ML data were therefore collected at the same q position and at the same

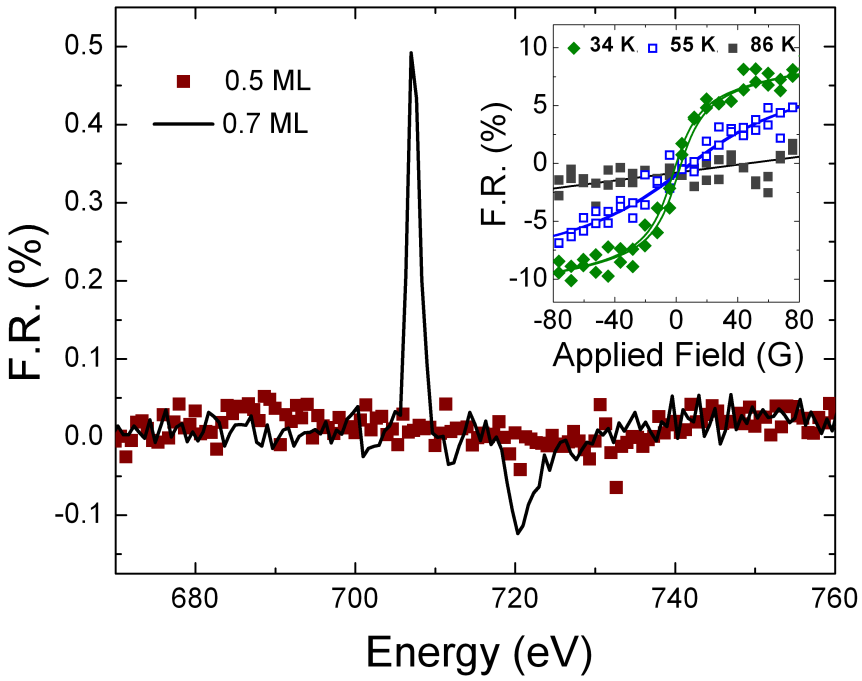

Figure 6.17: Fe XMCD as a function of energy in a field of 80 G. A clear magnetic signal with the expected shape and sign reversal is observed at the $L_{2,3}$ edges for the 0.7 ML sample (line). No detectable magnetic signal was seen for the 0.5 ML sample (squares). Inset: Field dependence of the XRMS (points) and Langevin fit (line) from the 0.7 ML sample as a function of temperature.

energy as the 0.7 ML data.

No magnetic response was apparent at the Fe edge, up to 8 mT, at any energy, in the 0.5 ML δ-layer sample. The total lack of Fe moment in the 0.5 ML regime, even under an applied field sufficient to saturate the 0.7 ML sample, is compatible with a band hybridisation theory in which the electron DOS within the Fe is sufficiently suppressed for no spontaneous moment to form. Although the Fe displayed no observable remanent magnetisation at any temperature accessible, the 0.7 ML δ-layer showed a paramagnetic response which evolved slowly over a wide temperature range, with M_{sat} reducing and H_{sat} increasing. This is consistent with superparamagnetic behaviour which is potentially suggestive of an onset of short-range magnetic order which occurs below the thickness at which long-range FM order first occurs.

To further test the supposition that electron band hybridisation leads to the observed loss of the Fe moment in this FePd system, a dilute alloy can be examined.

Dilute FePd alloys with Fe concentrations as low as 0.025 at. % have been shown to display ferromagnetic order [124] due to the large range of the induced Pd moments. A single ML of Fe polarises a Pd region extending approximately 10 ML from the Fe layer. This equates to an Fe concentration, within the polarised region, of approximately 5%. By dispersing the same concentration of Fe evenly throughout an alloy, the effect of the overlapping electron bands will be enhanced due to the increase in Pd nearest neighbours, and the Fe-Fe coupling strength will be reduced due to their increased separation. Such an alloy should therefore create conditions which are unfavourable for the formation of an Fe moment; no spontaneous FM order on the Fe sub-lattice would be expected.

The element specific magnetisation as a function of temperature was therefore collected for a 5% FePd alloy. The Pd edge data were collected in accordance with the methodology used to determine the trilayer moments described earlier. The Fe edge data were collected by maximising the F.R. at base temperature in the usual way and recording the magnetic response in an applied field of 4 mT as the temperature was ramped from 120 K to 320 K at a rate of 2 K/min. This was due to time constraints during the beamtime and has the disadvantage of not removing domain effects. The resulting element specific magnetic ordering behaviours are shown in the left panel of figure 6.18.

Clearly, the Fe moment is measurable. In fact, both the Fe and Pd moments show identical behaviour. Above T_{C}, which was determined to be 267.5 K from log-log fitting, the Fe signal displays an extended tail due to the applied field during data collection. Log-log analysis is therefore performed on the Pd moments (lower right panel), which display mean-field behaviour. The clear FM behaviour of the Fe moments in this alloy makes a description of the vanishing moment in the FePd trilayers which is solely dependent on the hybridisation of the conduction electron band improbable. This, coupled with the superparamagnetic response of the 0.7 ML sample, shows the geometry of the Fe distribution must play a crucial role.

The geometry of an ideal sub-monolayer regime is a randomly distributed layer of incomplete coverage with a fractional occupancy defined by the "thickness" of the layer. For a random distribution of particles, the *percolation limit* defines the fractional occupancy required to facilitate long-range nearest-neighbour interconnectivity. Below this limit, the layer will consist of islands that are locally interconnected but do not share connections to neighbouring islands. In the two-dimensional case, this theoretical limit for a hexagonal lattice is 0.5 [125]. It should be noted, however, that this is an imperfect model of a FM system. Though nearest-neighbour interactions will be mediated most strongly, more distant interactions with diminish-

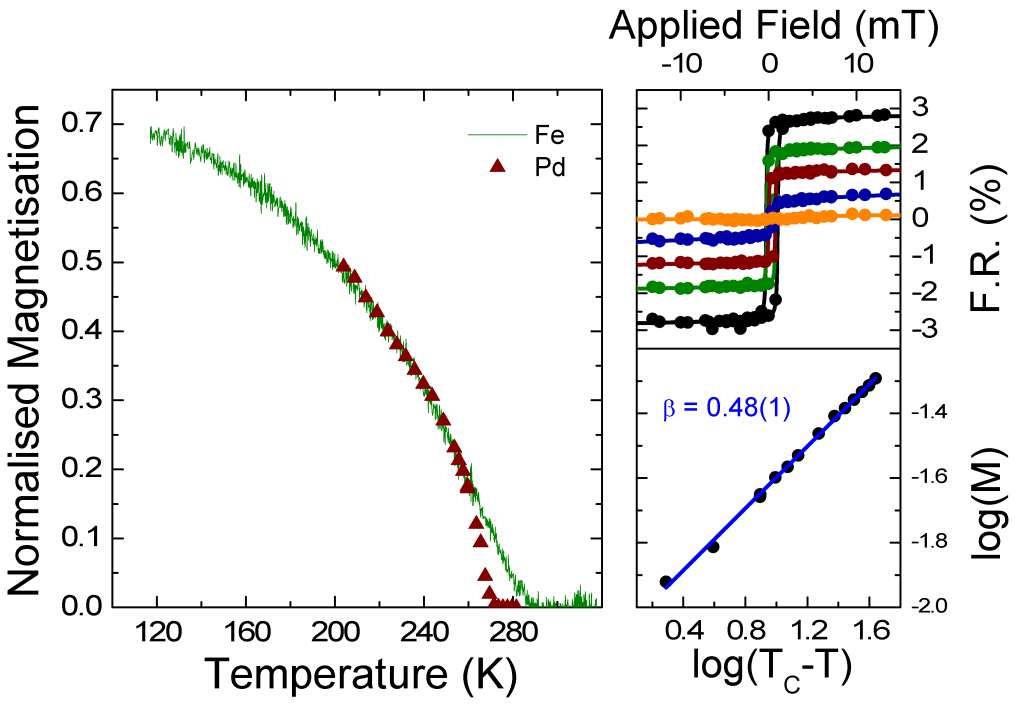

Figure 6.18: Element specific magnetic ordering data (left panel), from an Fe_5Pd_{95} alloy, show identical behaviour approaching T_C with prominent field induced tails in the Fe moments above T_C. Both show mean field behaviour extracted from the log-log data (lower right). Pd edge hysteresis loops (upper right) show no change in field response as the transition is approached.

ing strength are still present. The percolation limit therefore describes a lower limit above which FM order would be expected in a perfect crystallographic arrangement. Crystallographic imperfections will, however, lower the effective occupancy of any system making accurate quantitative analysis difficult.

The apparent superparamagnetic behaviour of the Fe moments in the 0.7 ML δ-layer suggests that the Fe concentration is below that required for the formation of long range order. Instead the moments have formed into locally ordered magnetic islands which readily align to a magnetic field; a superparamagnetic ensemble of ferromagnetic islands. Though a 0.7 ML layer is above the theoretical coverage required to form long range order, imperfection in the termination of the Pd layer upon which the Fe layer is grown has lead to an imperfect 2D layer. As such, an increase in the concentration of Fe atoms required to form long-range order is likely. The 0.5 ML layer has a fractional occupancy on the percolation limit and shows no nett moment; the Fe moments are sufficiently disconnected to suppress magnetic

alignment.

The alloy represents a 3D lattice of Fe and Pd moments; the percolation limit for an hcp structure is 0.20 [126]. This is much greater than the Fe fraction of 0.05 present in the alloy. The effect of longer range interactions will, however, be considerably higher in a 3D arrangement due to the significant increase in the number of next-nearest-neighbours. A more accurate analysis of the likelihood of a geometric origin for the lack of FM moment carried by the thinnest Fe films remains elusive and requires detailed calculations of Fe-Fe interactions and Fe-Pd-Fe mediated interactions. This description, however, remains plausible.

This result leaves an opportunity for further investigation, both theoretically and experimentally. A theoretical study of magnetic interactions at different length-scales could be supplemented by an experimental investigation of the Fe moments in FePd alloys with reduced concentrations of Fe. If a critical concentration of Fe was found below which the the moment was lost, which coincided with a theoretical description, the hypothesised geometric origin for the suppression of the Fe moments could be reinforced.

Another possibility which has not been discussed is the orientation of the moments. As described in chapter 3, both XRMS and PNR are only sensitive to the area averaged moment within the sample plane, parallel and perpendicular to the scattering plane respectively. Neither technique has sensitivity to antiferromagnetic alignment. Both investigative techniques also lack sensitivity to out-of-plane moments. If there was sufficient anisotropy to rotate the interface moments into the out-of-plane direction, the application of an applied field would begin to rotate the moments toward the applied field direction resulting in a measurable nett moment.

These alternative models can not be resolved using the techniques employed in this work. To help develop an understanding of the magnetic interactions across an interface, density functional theory calculations are ongoing.

6.5 Conclusions

In this chapter, the fundamental interactions between FM moments across a buried FM-FM interface were investigated in FePd trilayers. The spatial extents of the element specific moments were extracted from reflectivity data. The simultaneous fitting of resonant x-ray and polarised neutron reflectivity data, using the GenX code, provided a simulation with greater accuracy and with greater flexibility than previously achievable. The spatial extent of the induced moments within the polarised Pd region was found to be independent of Fe δ-layer thickness in accordance with

the theoretical description from the literature. The investigation into the element specific magnetic ordering showed differing behaviour between the two sub-lattices originating from an indirect interaction between the two element species mediated by the temperature dependent susceptibility of the Pd. This interaction mechanism had not previously been observed. The dimensionality crossover apparent in the Pd moments is an artifact of this interaction and does not signify a true change in spin dimensionality. The spontaneous Fe moment was seen to vanish for δ-layer thicknesses below 1 ML. It is tentatively suggested that this is driven by the percolation limit through the geometry of the system rather than solely through the interaction of itinerant electron bands as suggested for similar examples in the literature. These unexpected results highlight our poor understanding of these fundamental interface interactions and emphasise the need for extensive further research. This work has, however, established techniques that will allow future analysis to be performed with unprecedented precision.

Further Fe edge studies of similar trilayers are needed to more accurately establish the inducing profile shape. If these studies could include data at higher q-vectors, the spatial resolution of the profile could be greatly increased. This would allow the interaction between the moments at the interface to be assessed. Examples in the literature [97, 101, 121] suggest that both enhanced or suppressed moments are possible. Another avenue of necessary further research is investigations into the loss of the Fe moment in the sub-monolayer regime. Theoretical studies into the effect of length scales on the magnetic order are greatly desired, which would be complemented by Fe edge studies of dilute FePd alloys. If a critical concentration of Fe was found below which the the moment was lost, which coincided with a theoretical description, the hypothesised geometric origin for the suppression of the Fe moments could be reinforced.

Chapter 7

Patterned Arrays

7.1 Introduction

Patterned arrays of nanoscale magnetic islands have become an area of particular scientific interest in recent years [127], and through careful choice of array and island geometry, have lead to a wealth of interaction phenomena being observed [128, 129]. These arrays have the potential to be exploited in two distinct ways.

The first is in technological applications such as ultra-high density data storage devices [10]. The patterned structure can be exploited to allow individual islands to represent individual data bits. Current magnetic data storage media use continuous magnetic films containing locally magnetic/not magnetic regions. Patterning allows adjacent regions to be much closer together without loss of data as the islands are physically separated. The distinction between 1s and 0s within each island can be made by exploiting magnetic vortex structures. In these structures, each island contains a magnetic vortex, i.e. concentric closed magnetic loops, which can exist have one of two states with opposite chirality. These vortices have been observed in a number of studies of circular [130] and annular [131] islands. This arrangement has the additional advantage of removing stray fields from between the islands, reducing their interaction potential.

The technological advantage of vortex arrangements in patterned elements is their potential to store information within a densely packed array of islands. There is, however, the possibility that individually ferromagnetic island could align in approximately concentric rings to produce vortex states on a larger scale. The potential advantage for data storage is then clearly lost. Although it is possible to measure the magnetic state of an individual island [132], resolving these two possible states requires a technique which has the potential to be sensitive to both states.

This work will therefore concentrate on the development of a novel application of XRMS, through which the variation in the magnetic correlation lengths between the two states can be exploited to allow them to be resolved. These studies will be detailed in section 7.2.

The second use of patterned materials is as a means of studying complex, artificially induced, magnetic interactions. A simple example of the modification to the magnetic behaviour available via patterning was observed by Cowburn et. al. [133] studying an array of circular supermalloy islands on a rectangular grid. Increasing the grid spacing along one of the array directions lead directly to a reduction in T_{C}. This is because the patterned islands behave analogously to atomic moments in the Curie-Weiss model. Within the Curie-Weiss model, a ferromagnetic (FM) material is defined as a lattice of coupled moments, with coupling constant J. The Hamiltonian for such a system is described by equation 2.5. The thermal energy required to overcome the magnetic coupling within the lattice defines T_{C}. The increase in grid spacing decreases the coupling constant and reduces the energy required to realign the moments, reducing T_{C}. T_{C} can therefore be considered as a measure of the interaction energy between neighbouring islands. This interaction energy is a combination of several coupling phenomena, the most influential of which is the dipole interaction. The dipole interaction energy is defined as [24]:

$$E_{\mathrm{dip}} = \frac{\mu_0}{4\pi r^3}\left[\mathbf{m}_1 \cdot \mathbf{m}_2 - \frac{3}{r^2}(\mathbf{m}_1 \cdot \mathbf{r})(\mathbf{m}_2 \cdot \mathbf{r})\right]. \tag{7.1}$$

where $\mathbf{m}_1$ and $\mathbf{m}_2$ are the total moments carried by interacting islands separated by a distance r. It is clear, therefore, that the interaction potential between neighbouring islands is strongly governed by both element size, which is proportional to $\mathbf{m}$, and grid spacing. This allows modifications to the size, spacing and composition of the elements to provide novel ways in which to study magnetic interactions in a tightly controlled environment creating the prospect of new and exciting avenues of research.

These modifications to the shape and arrangement of the array elements allows direct control of the magnetic anisotropy present within the array [134]. As any artificial array will be manufactured to have a regular structure, anisotropy due to the arrangement of elements is unavoidable. This is analogous to the magnetocrystalline anisotropy in crystal structures. The shortest separation between neighbouring islands will define the orientation of moments which is energetically preferable. Reducing the array spacing along a particular direction leads to the preferential alignment of the element moments along that direction and so the easy

axis direction can be controlled. Modification to the shape of an element similarly produces shape anisotropy. A circular island has no shape anisotropy and so no easy or hard axes. An elliptical island has an easy axis along its major axis.

The array pitch and island size allow the strength and separation of the island moments to be tightly controlled and artificial magnetic interaction phenomena to be induced. Earlier work by Arnalds et al. [135] used MOKE to examine the remanent magnetic ordering displayed by the total moment from circular Pd/Fe/Pd islands on a square lattice. A phase transition from a superferromagnetic to a superparamagnetic arrangement of internally ferromagnetic islands was observed. These findings will be discussed in more detail in section 7.3. The temperature of the phase transition was seen to vary with island size (i.e. total island moment), but the dependence does not conform to the description given by equation 7.1. Within this chapter, the previous studies by Arnalds will be extended to include XRMS data. The primary advantage of XRMS is that is allows the diffuse scattering to be exploited to circumvent the dominant contribution to the scattered intensity from the substrate which is observed for widely spaced islands when in the specular condition. These more robust data can then allow the unexpected behaviour seen in the MOKE studies to be confirmed or denied. It is hoped that through these data, a greater understanding of the interaction mechanisms between the islands can be established, and the unexpected dependence of the phase transition on island size can be explained.

7.1.1 Samples

In this chapter, both the formation of magnetic vortices, and the interaction between ferromagnetic islands will be studied. The simplest geometry in which to study these phenomena is arrays of circular islands on square grids. This is because circular islands minimise the stray field if an internal vortex is formed. Furthermore, circular islands are magnetically isotropic. This means that if a ferromagnetic element is formed, the minimum energy is required to rotate the alignment direction. This ensures the maximum sensitivity to inter-element interactions is available. Arranging the element on a square grid is the simplest available interactive configuration, and has predictable preferential alignment directions.

To conduct these studies, a further, necessary simplification is required. Each island must be constrained to contain only one magnetic domain. Multi-domain islands will tend to form opposing domains with no nett island moment, nullifying their interaction potential to neighbouring islands. In magnetic islands, a competition exists between thickness and diameter which dictates the magnetic configuration

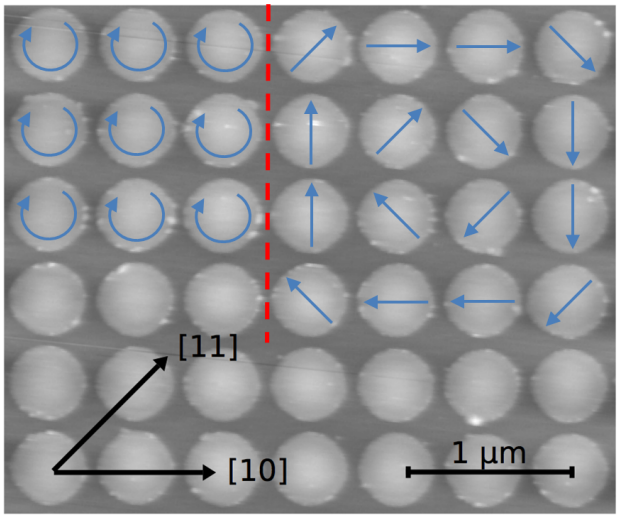

Figure 7.1: AFM image of circular FePd alloy islands on a square grid. Blue arrows indicate two possible magnetic vortex arrangements.

[136]. More specifically, as the thickness decreases, the diameter below which single domain structures are expected increases. In the intermediary phase between single and multi-domain islands, magnetic vortex states can form, discussed in more detail in section 7.2. The patterns studied in this work are composed either of ultra-thin layers, which can be considered single domain, or thicker layers in the vortex state. The effects of multi-domain formation will be ignored.

For the studies of vortex states, a continuous, 100 nm film of FePd alloy (20% Fe) was grown using MBE, and was patterned into 450 nm circular islands on a 500 nm square grid using EBL. Initial characterisation using MOKE (not shown) displayed hysteresis behaviour in accordance with that expected of magnetic vortex formation [137]. Within these alloy islands, a uniform magnetic distribution is expected in the out-of-plane direction in accordance with that observed in the continuous film (shown in chapter 6). An AFM image of the sample structure is shown in figure 7.1 with the two possible magnetisation arrangements indicated.

For the studies of the superferromagnetic to superparamagnetic phase transition, δ-doped Pd(Fe) films were grown, by collaborators at the University of Uppsala, onto MgO (100) substrates by dc magnetron sputtering [109]. The materials were deposited from sputtering targets of 99.99% purity at an Ar pressure of 4 mTorr. Initially a 10 ML V seeding layer was grown onto the MgO substrate in order to alleviate the large lattice mismatch between Pd and MgO and increase the wetting of Pd onto the substrate. Two films with approximate Fe layer thicknesses of 0.6 ML, embedded between 20 ML of Pd (1.95 nm) were grown (see Figure 7.2).

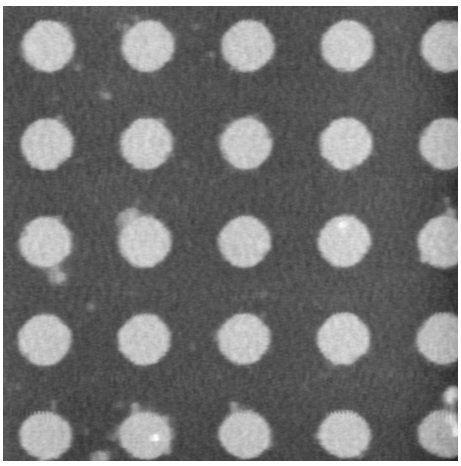

Figure 7.2: AFM image of an array of 400 nm Pd/$Fe_{0.6\ ML}$/Pd circular islands on an 800 nm square grid.

After growth, one film was patterned by electron beam lithography into 400 nm diameter circular islands, arranged on an 800 nm square lattice covering an area of 1×1 mm^2. The patterning was performed by writing circular holes into a positive resist layer deposited onto the films followed by growth of an Al etch mask and a lift-off process. The pattern was then transferred into the films by Ar-ion milling using the circular Al islands as an etch mask. Finally a 5 nm Al protective layer was grown onto the patterns to prevent degradation of the structures. MOKE studies (not shown) of the fabricated films showed ordering temperatures corresponding to Fe layer thicknesses of 0.6(1) ML in the patterned array and 0.7(1) ML in the continuous film. This minimal discrepancy is not likely to affect the experimental results. The uniformity of the patterning was verified using AFM, shown in figure 7.2.

7.1.2 Scattering From Patterned Materials

Investigations of patterned arrays can be achieved using scattering techniques [72]. As discussed in section 3.1, in-plane structures can be probed using rocking curves, which produce slices through reciprocal space in the q_x direction. A rocking curve, which is sensitive to both in-plane repeat distances and in-plane correlation lengths, has a shape which contains information about three different aspects of a patterned array. First, periodic "satellite" peaks which relate to the in-plane repeat distance (i.e. the island separation) in accordance with $\Delta d = 2\pi/\Delta q$. Second, an envelope function which describes the falloff in intensity of successive satellite peaks. This is determined by the in-plane extent of each island, i.e. the diameter of a circu-

lar island, and is therefore governed by the in-plane correlation lengths. The real space correlation lengths are inversely proportional to the reciprocal space extent in accordance with:

$$f/\Delta q = \xi \tag{7.2}$$

where Δq is the measured reciprocal space width, ξ is the real space correlation length, and f is a proportionality constant governed by the shape of the correlation function. Third, the width of the satellite peaks which is dictated by the length-scale over which the array remains homogeneous, which is again calculated using equation 7.2. Structurally, a patterned array is typically assumed to be homogeneous over the whole patterned area, and so the satellite peak widths are dictated by the instrument resolution, and in particular the x-ray coherence length. Using XRMS, both structural and magnetic contribution to the total scattering can be resolved. The shape of the magnetic contribution is again dictated by the same three contributions, the first two of which (determined by the island separation and size) are fixed to that of the structure. The third, however, is not. The prospect of exploiting this for investigating magnetic formations within the array will be explained in more detail in section 7.2.

To quantify correlation lengths within the array, it is therefore necessary to determine the widths of features within the data. A Pearson VII [138] is a versatile peak fitting function which will be used to perform this task. This function has two strengths: first the full width half maximum (FWHM) is a fitting parameter and is yielded directly, and second it contains a parameter which allows the shape of the function to change between extremes defining Gaussian and Lorentzian profile. This latter property is useful as the shape of the fitted peaks is not known. Fitting a Gaussian peak shape to a Lorentzian profile will fail to reasonably fit the peak amplitude, which will invariably detrimentally effect the FWHM. Using a Pearson VII ensures the most consistent and accurate fitting without prior knowledge of the peak shape.

Once the FWHM has been determined, the peak shape can be determined using the appropriate value of f. For a Lorentzian peak shape, $f = 2$, whereas a Gaussian peak shape has $f = 3.3$ [139]. The shape of the Pearson VII function will be allowed to freely move between Gaussian and Lorentzian extremes without being described ideally by either. As such, as a compromise, an f value of 3 will be used throughout. This simplification potentially introduces a 50% error in the resultant values. This error is, however, systematic and so comparative analysis can still conducted though quantitative analysis can not be considered reliable.

The large errors in the fitted widths due to data noise make this simplification a beneficial measure due to the fitting versatility gained. The numerical calculation to investigate the correlation lengths within the array therefore becomes:

$$\frac{3 * 4}{FWHM} = \xi. \tag{7.3}$$

where the factor of 4 arises due to the fact that Δq and ξ are the half-widths and half-extents in equation 7.2, and here ξ is the full extent.

To study these materials, a highly coherent probe is necessary so that the behaviour of a large area, containing many islands, can be investigated simultaneously. The larger the area studies, the smaller the effect of individual island behaviour on the data. Therefore, in this work x-ray magnetic scattering (XRMS) from square arrays of circular islands will be implemented to investigate both the vortex arrangement of moments within FePd alloy islands, and the interaction mechanisms between Pd/Fe/Pd trilayer islands. Using XRMS has the additional advantage of element selectivity. As our previous work has shown, FePd systems of the type in this study display behavioural differences between the Fe and Pd sub-lattices. By conducting these studies at the Pd L_3 edge, only the Pd sub-lattice is probed, and the potential effect of these differences is removed from the data. It is, however, important to note that only the nett magnetisation over all elements within the coherent beam footprint will be probed; the behaviour of any individual element will not be resolvable.

7.2 Magnetic Vortices

7.2.1 Introduction

The formation of magnetic vortices within an array element becomes energetically favourable when the energy gained through the removal of the stray field extending beyond the element outweighs the energy lost through the forced perpendicular (out-of-plane) orientation of the central moments; typically requiring the islands to be larger than 100 nm in diameter. Cowburn et al [137] demonstrated that a sufficient increase in the island thickness, which reduces the energy cost of arranging moments perpendicular to the sample plane, leads directly to the formation of magnetic vortices. These arrangements can exist in both single- and multi-domain [131] islands. An alternative arrangement of single-domain islands can form larger scale"supervortex" states comprised of an ensemble of reoriented ferromagnet islands. These states, demonstrated in circular arrays of magnetic islands [130],

benefit from a lack of perpendicularly orientated moments and can therefore be made substantially smaller. It is possible, however, that a similar state could form within a square grid of > 100 nm islands where single island vortices are desired. A method for resolving the inter- and intra-dot arrangements (henceforth referred to as magnetic vortex (MV) and magnetic supervortex (MSV)), which show an identical magnetic response to an applied field, is therefore crucial.

Measurements of the orientations of the magnetic moments within individual islands are possible [132]. However, the ferromagnetic (FM) arrangement of moments in the MSV state can not be distinguished from the saturation response of the MV state, making unambiguous determination of the former state impossible. A technique examining the global magnetic response, while sensitive to local magnetic behaviour, is therefore desirable.

As previously discussed, XRMS can yield information about the in-plane magnetic correlation lengths through the collection of rocking curves. The width of the structural satellite peaks within the rocking curve data are governed by the structural coherence of the islands across the array. In reality, the consistency between islands sizes across the array is sufficiently good that the satellite peak widths are resolution limited. The magnetic contribution is governed by the magnetic homogeneity throughout the array. For an array consisting of islands in an identical magnetic state, whether that is ferromagnetic or MV, the magnetic satellite peak width would be fixed to that of the structure. However, for the MSV state, a broadening of the magnetic satellite peak would be expected as only those islands within the local region of the MSV will show a correlated arrangement. An attempt to resolve the difference between the two states can therefore be made by examining the in-plane magnetic correlation lengths present within the array.

The high coherence length available at synchrotron x-ray sources should allow these two states to be resolved, however, exploiting XRMS to probe the magnetic behaviour of a patterned array is technologically challenging, with few examples available in the literature. Sanchez et al. first demonstrated the feasibility of the technique [140] by using linear polarised photons to initially examine structural diffraction peaks, yielding the size and spacing of the array, which was followed by element specific hysteresis loops along both the hard and easy axis. The work presented here is a novel application of the XRMS technique in an attempt to exploit changes in the globally averaged magnetic correlation length to elucidate changes to the magnetic structure on the island scale.

7.2.2 Magnetic Rocking Curves

Magnetic information was extracted from resonant magnetic x-ray scattering data collected at the Pd L_3 edge on beamline 4-ID-D at the APS. The sample, the structure of which is described in section 7.1.1, was orientated such that the collinear incident beam and applied field directions acted along the [01] direction of the array (see figure 7.1). This was achieved by rotating the sample in the plane (Phi rotation) until no splitting was observed in the specular rocking curve. A large slit (0.5 mm out-of-plane, 5 mm in-plane) was used for the initial rocking curve, maximising available flux but reducing the angular resolution. Magnetic reflectivity data along the +1 satellite peak, and F.R. data as a function of energy, across the L_3 edge, were iteratively collected in order to optimise the scattering condition through maximising the observed F.R.. The maximum F.R. was found to occur at $q_z = 0.0953$ Å^{-1}. The energy was reduced from the maximum F.R. value by 0.5 eV, in the customary way, to reduce absorption. Subsequent magnetic hysteresis and rocking curve data were recorded at this q_z position.

Measuring a magnetic response of a vortex state is challenging, as the closed loops prevent any nett moment forming, i.e. there is no remanent moment (see figure 7.3). The application of a small field allows a nett moment to be measured, due to a shifting of the closed loops. At a critical field value, however, the vortex formation will be overcome, and the islands will ferromagnetically align. To find the appropriate field value range over which the vortex state can be studied requires the collection of hysteresis loops. This must be performed at the satellite peak position, a region with low scattered intensity, as that location will be used for the rocking curve analysis. However, as the magnetic response in the specular condition will likely show the same result, loops in both locations were collected. The measurements were performed by recording the F.R. of the scattered intensity upon reversing the incident helicity of 3.174 keV photons, at a fixed q_z vector of 0.0953 Å^{-1} and q_x vectors of 0 and -1.2×10^{-3} Å^{-1} for the specular and -1 satellite peak respectively. The external field, applied in the in-plane [01] direction, was incremented in discrete steps starting at negative saturation. The results are displayed in figure 7.3.

Both loops show identical behaviour, with the shape of the magnetic hysteresis loop coinciding with that observed by Cowburn et al., [137], for a patterned material displaying vortex behaviour. The similarity between the two loops allows the superior signal to noise available in the specular condition to be exploited to define the field values require to reach each phase with greater accuracy.

As the magnitude of the applied field strength reduces from saturation, the

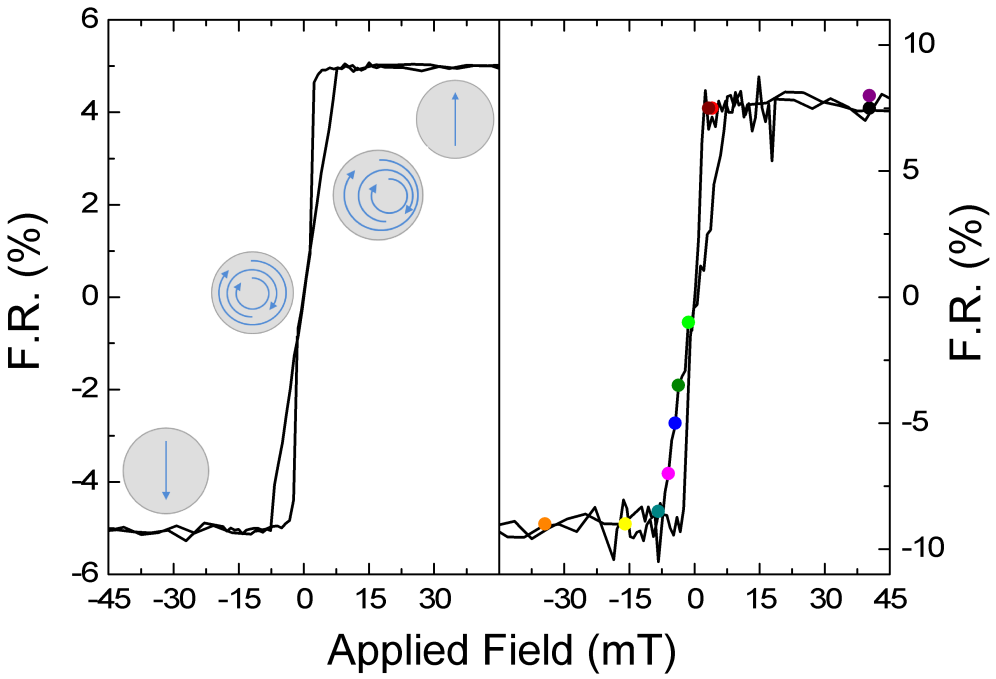

Figure 7.3: Pd edge magnetic hysteresis loops collected in the specular scattering condition (left panel) and −1 satellite peak position (right panel) from an array of 450 nm FePd alloy islands on a 500 nm square grid. Coloured dots indicate field values later used for rocking curves.

nett magnetic moment rapidly collapses, to approximately a fifth of the saturation moment, as the induced alignment of the moments is lost and closed magnetic loops are formed. The small remaining moment is maintained due to the asymmetry of the closed loops, which then reduces approximately linearly until H=0, M=0 is reached and the nett moment is lost due to the vortex formation. This linear trend is continued with increasing field values up to 8 mT. In this linear region, the increasing applied field strength causes the centre of the closed loops to drift perpendicularly to the applied field direction, expanding the region containing moments that are collinear with the applied field. Above 8 mT, the applied field strength is sufficient to overcome the formation of closed loops and ferromagnetic saturation occurs. The transition period, in which an evolution in the measured behaviour of the vortices is expected, therefore occurs between 0 and 8 mT. The coloured dots on figure 7.3 coincide with field values which will subsequently used for rocking curves which will be indicated through appropriate line colour.

To begin the categorisation of the vortex state, a wide rocking curve was then

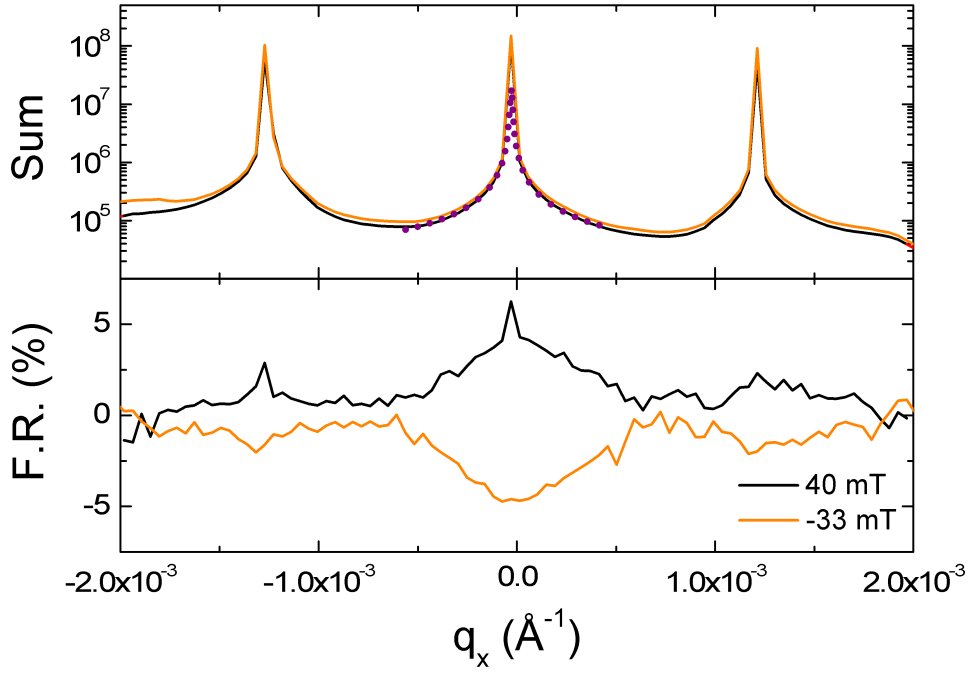

Figure 7.4: Upper and lower panels respectively show structural and magnetic contributions to the Pd edge rocking curves across the specular and ±1 satellite peaks, from an array of 400 nm FePd alloy islands on a 500 nm square grid, with a fixed q_z of 0.0953 Å^{-1}. Data were collected at saturating fields of ± 40 mT. The specular peak shows fitted Pearson VII function (dotted line), as discussed in the text.

collected. Upper and lower panels of figure 7.4 show the structural and magnetic contributions to the observed scattering. The specular reflection ($q_x = 0$) and ± 1 satellite peaks ($q_x = \pm 1.26 \times 10^{-3}$) are clearly visible, each with an approximate width of 1.7 ± 0.3 $\times 10^{-6}$ Å^{-1}. The spacing corresponds to lattice periodicity of 499 ± 1 nm, in agreement with expectation. The width indicates consistent patterning across ≈ 700 μm of the sample surface.

Broad, reversible magnetic features are observed across each of the satellite peaks with the data remaining non-zero over all observed space. This indicates that under saturating conditions, the structurally consistent lattice is displaying magnetic inhomogeneity. It is possible that magnetic coupling between the islands, which are in very close proximity to their neighbours, is preventing the ferromagnetic islands from fully and consistently aligning with the applied field.

Analysis of the width of the magnetic contribution across the satellite peaks is not possible due to the low point density and poor counting statistics. A more

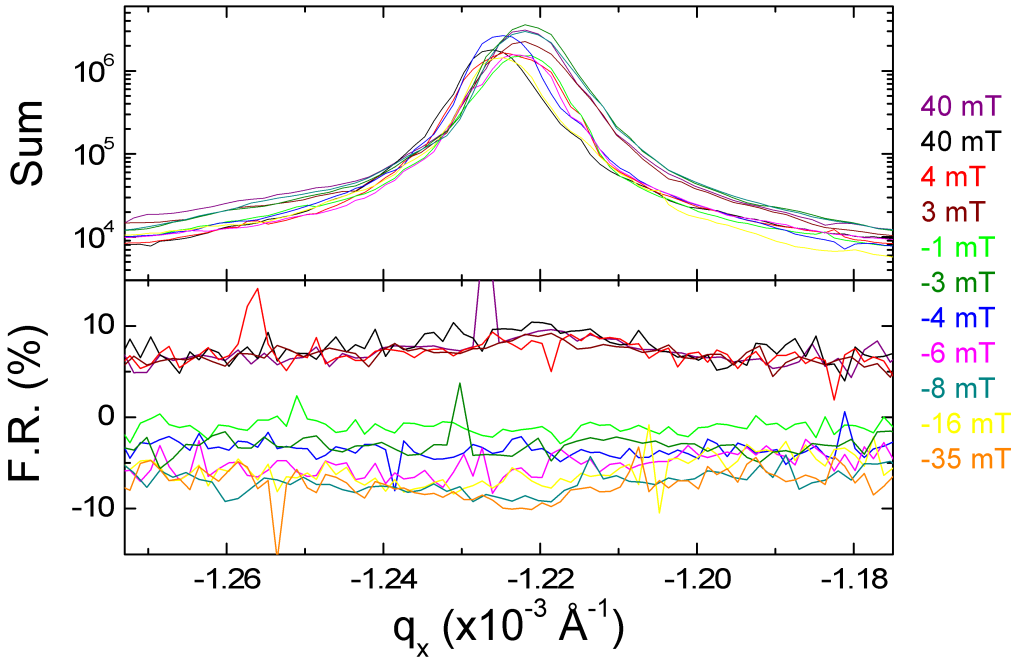

Figure 7.5: Upper and Lower panels respectively show the structural and magnetic contributions to the Pd edge rocking curves across the -1 satellite peak from an array of 450 nm FePd alloy islands on a 500 nm square grid.

detailed examination was therefore performed across the -1 satellite peak. Data were collected at applied field values indicated by the coloured points in figure 7.3. These field values include those necessary to form the vortex state. In order to maximise the available angular resolution, a pinhole slit of approximate dimensions 50×50 μm was used at the cost of incident flux. All other experimental conditions remained the same. The collected data are shown in figure 7.5.

A non-zero moment was again recorded across all measured space indicating an inhomogeneous magnetic structure across the array. At saturation, this could indicate magnetic coupling between adjacent islands, however, in the MV state the removal of the stray field removes this possibility. This non-zero moment, which exists in the data collected at field values necessary for a vortex state to form, suggests the MSV state could be present.

Quantitative analysis was performed through fitting of the data to Pearson VII functions, assuming a trend tending to zero at $\pm$ infinity. The small changes in the locations of the maxima of the scattered intensities are likely due to small discrepancies in the sample location caused by the changes in the applied field strength.

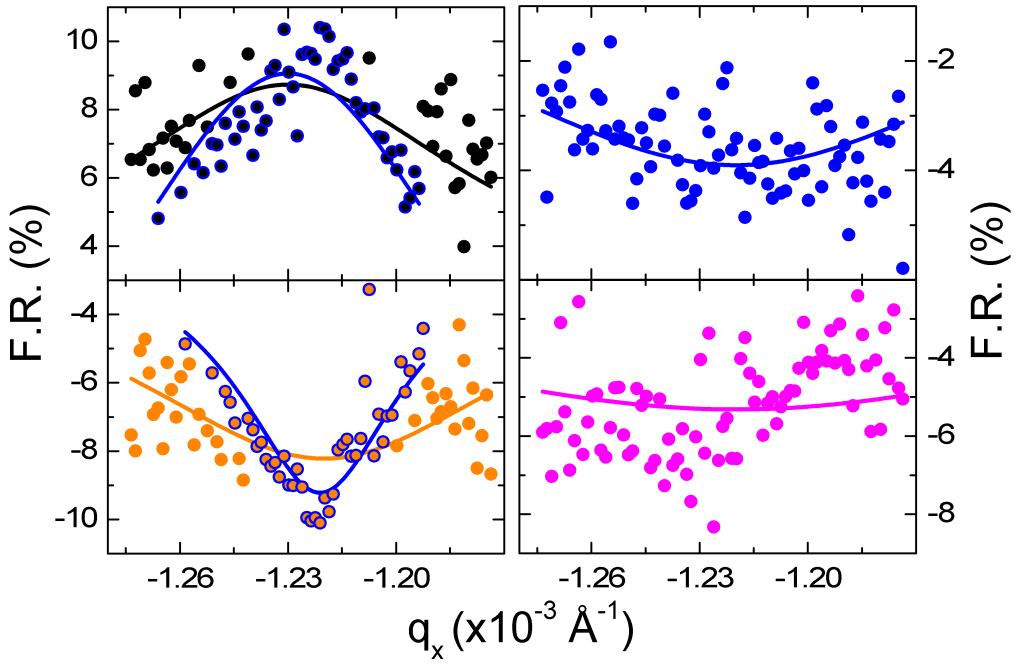

Figure 7.6: Magnetic contributions to the Pd edge rocking curves across the −1 satellite peak from an array of 450 nm FePd alloy islands on a 500 nm square grid. Field values correspond to the coloured dots indicated in figure 7.3.

For the purposes of data fitting, the centroids of the magnetic peaks were fixed to those of the structure; no detrimental effect on the results is expected. The structural peaks show an averaged width describing a real-space structural correlation length of 130 μm, consistent with the expected coherence of the incident x-rays.

Fits to data at select field values are demonstrated in figure 7.6. Upper and lower left panels show data from negative and positive saturation respectively. Both show a broad magnet response with a width corresponding, through application of equation 7.3, to a real-space feature with a 8 $\pm$ 4 μm correlation length. The shape of the data is, however, possibly suggestive of an underlying, narrower profile. These underlying shapes, indicated as blue open circles, were fitted independently to additional Pearson VII functions. The results, defining the narrowest possible profile within the data, suggest a maximum magnetic correlation length of 18 $\pm$ 2 μm, an order of magnitude less than that described by the structure. Right panels show data from two fields within the critical transition period. The upper right data, at 4.5 mT, show a different behaviour to that seen at saturation. The broad, noisy feature remains, but the underlying structure is gone. The fit to this data shows a

magnetic correlation length of 6 ± 4 μm; a reduction from saturation, but with an uncertainty that makes strong conclusions difficult to draw. The lower right data, at 6 mT, show an inconclusive magnetic correlation length of 4 ± 4 μm. However, the data tentatively suggest the formation of the underlying shape visible at saturation, possibly representing the onset of the saturation structure.

Though the noise in the data make any quantitative assessment difficult, the data suggest the formation of the MSV state. If the MV state was present a narrow rocking curve width would be expected, representing magnetic homogeneity across the array. Instead, the magnetic vortex state at 4.5 mT suggests a magnetic arrangement in which homogeneity extends over an area of 13 × 13 islands. A subsequent narrowing of the magnetic satellite peak as the field is increased to 6 mT suggests the expansion of the vortex area as saturation is approached.

The results, though limited by substantial uncertainties, suggest unusual behaviour warranting further investigation. Future work would be greatly enhanced by greater statistical significance, however, the competition between resolution and flux makes the desired improvements to data quality difficult without significant increases in counting times. Such improvements are often unattainable when reliant upon use of central facilities. These results nevertheless successfully demonstrate the viability of using global diffuse scattering to investigate the local magnetic arrangements within patterned structures.

7.3 Trilayer Array

Studies by Arnalds et al. [135] used MOKE to examine the remanent magnetic ordering displayed by the total moment from circular Pd/Fe/Pd islands on a square lattice. The Fe was confined to a δ-layer with an approximate thickness of 1 ML, the variation of which was exploited to modify the ordering temperature. An additional magnetic phase transition, varying as a function of island size, was observed when compared to an equivalent continuous film. This was attributed to the breaking of complex magnetic interactions between adjacent islands at temperatures well below the continuous film ordering temperature. Figure 7.7, taken with permission from [135], shows this superferromagnetic (SFM) to superparamagnetic (SPM) phase transition as a function of island size. As the island size decreases, a significant reduction in the temperature required to break the inter-island interactions is seen.

These studies by Arnalds et. al. can be complemented using x-rays. Resonant x-rays provide two advantages over MOKE for studying patterned materials. First, x-rays allow the out-of-plane structure to be resolved. More importantly, the

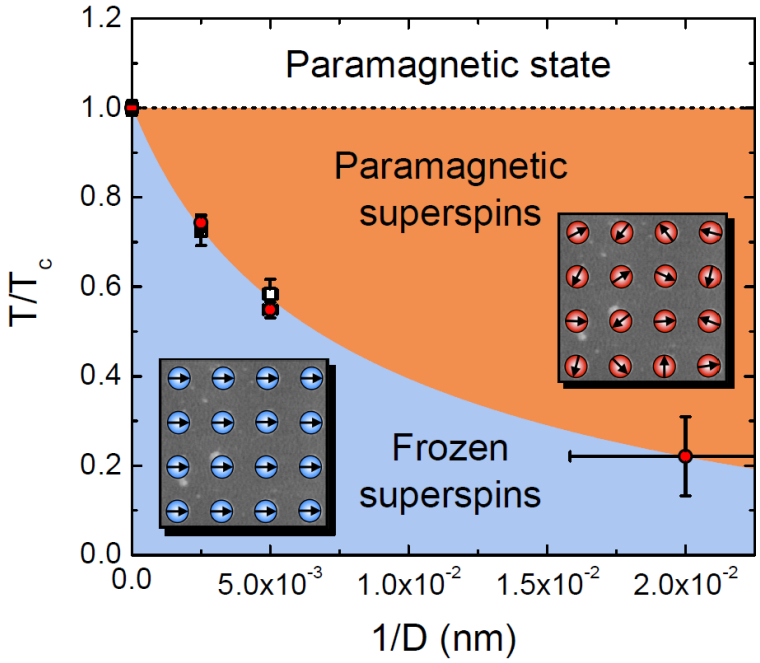

Figure 7.7: Squares and circles respectively show the inter-island ordering temperature, as a fraction of T_C, from a 1.2 ML and 0.6 ML Fe δ-layer in Pd, as a function of inverse island diameter. Taken with permission from [135].

high intensity and high coherence of synchrotron radiation allows the diffuse scattering to be exploited. MOKE, which measures the volume integrated total moment, becomes dominated by the non-magnetic contribution from the substrate as the array pitch is increased. Using the satellite peaks in the diffuse scattering eliminates this problem, as only those structures with in-plane periodicity (i.e. the patterned islands) contribute constructively in these positions.

A comparison of the Pd edge, field-dependent magnetic ordering between a continuous Pd/Fe/Pd trilayer film and a patterned array of circular islands on a square grid was therefore made using resonant x-ray scattering. A 0.6 ML Fe δ-layer thickness, with an island size of 400 nm, was chosen for this study allowing a direct comparison between resonant scattering and MOKE (Arnalds) data to be made in a region where the SFM to SPM phase transition is sufficiently distant from the FM to PM transition at T_C.

The structure of the samples is described in section 7.1.1. The expected patterned structure can be verified using a magnetic rocking curve which is sensitive to the in-plane structure. As such, Pd edge rocking curve data were collected across the specular, $\pm$ 1 and $\pm$ 2 satellite peaks. The structural and magnetic contributions

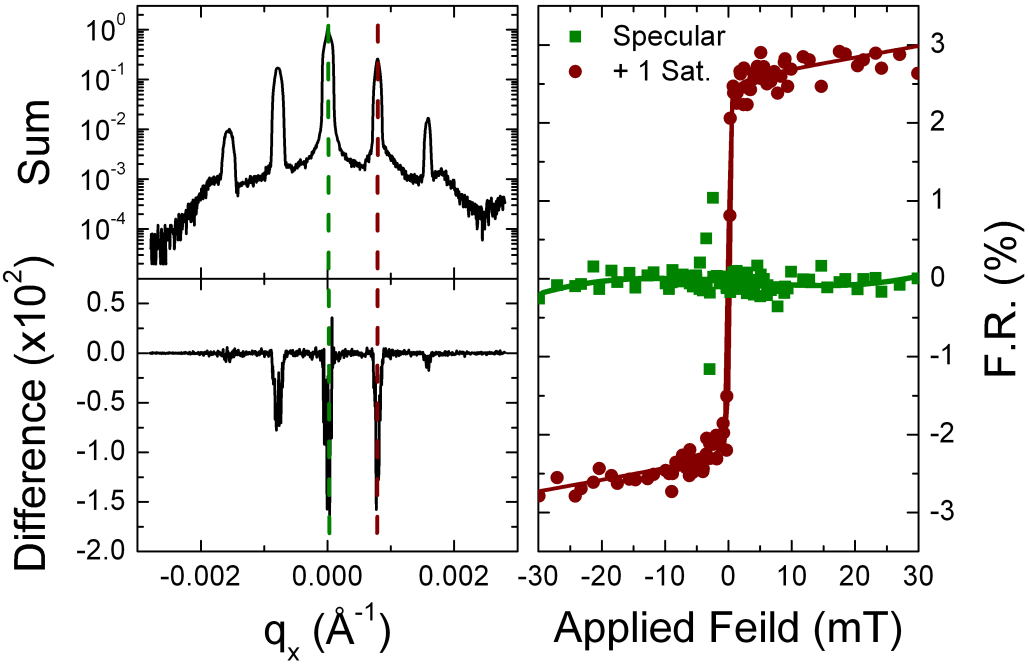

Figure 7.8: Left panels show structural (upper) and magnetic (lower) contributions to a Pd edge magnetic rocking curve, from 400 nm circular Pd/Fe/Pd islands on am 800 nm square grid, displaying periodicities governed by the in-plane structure. Right panel shows Pd edge hysteresis loops (points), collected at the indicated positions, fitted to pairs of arctan functions (lines). The dominance of the structural component of the total scattering suppresses the observed F.R. in the specular condition. The Sum is normalised to 1 for convenience.

to the scattering are shown in the upper and lower left panels of figure 7.8. The "Difference" corresponds to the difference in normalised intensity observed upon reversal of the incident helicity, and is equivalent to the F.R. multiplied by the sum of these normalised intensities (denoted "Sum").

To demonstrate the dominance of the structure in the specular condition, Pd edge hysteresis loops were collected in both the specular and +1 satellite peak positions, the results of which are displayed in the right panel of figure 7.8. Subsequent measurements must, therefore, be conducted at the +1 satellite position at the cost of a significant reduction in flux. The shape of the hysteresis loop observed at the +1 satellite position is consistent with that recorded from an array of single-domain, ferromagnetically ordered, islands [137] and is in agreement with those observed on similar samples, using MOKE, by Arnalds et al [135].

The specular, ±1 and ±2 satellite peaks have a uniform separation indicative

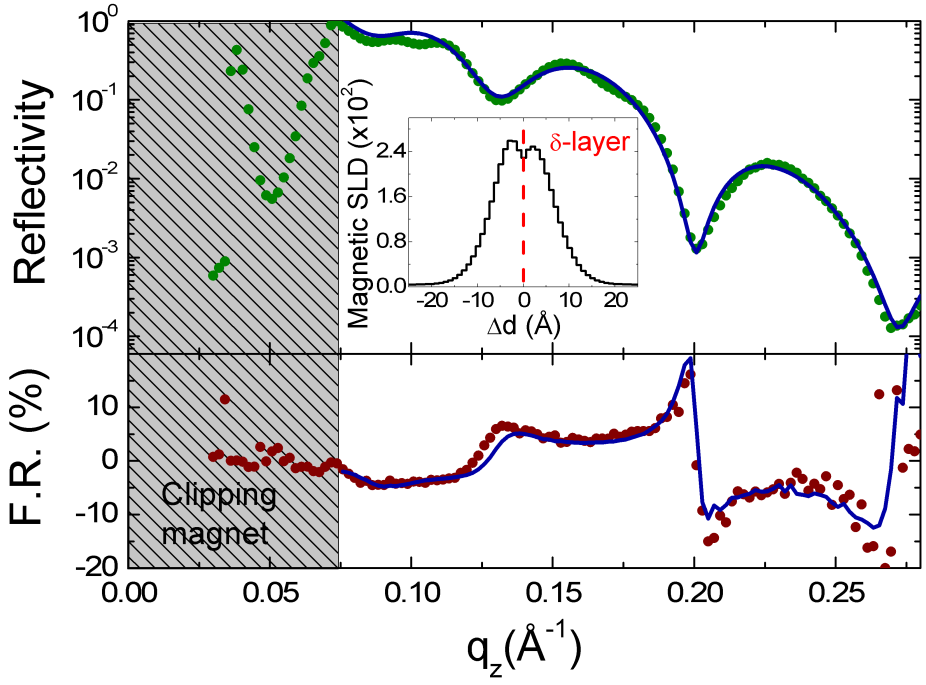

Figure 7.9: Upper and lower panels respectively show structural and magnetic contributions to the Pd edge magnetic reflectivity data (points) from 400 nm circular Pd/Fe/Pd islands on an 800 nm square grid. Fitting (line) using the GenX code [94] produced the magnetic profile shown (inset).

of a real space feature with a repeat distance of 800 nm. The gradual narrowing of the peaks with increasing q_x is a result of an increasing experimental resolution associated with the increasing incident angle. Saturation of the specular peak makes a meaningful estimate of the island size impossible. The consistent patterned structure seen in the SEM will be assumed to extend throughout the array.

To verify that the patterning process did not affect the composition of the islands, reflectivity data, containing the out-of-plane structural and magnetic profiles, were collected at the +1 satellite peak position, ensuring magnetic sensitivity. The results are displayed in figure 7.9 with the fitted profile produced using the GenX code [94]. Below $q_z = 0.075$ Å^{-1}, a rapid and unphysical drop in the specular intensity was observed, denoted by the shaded region of figure 7.9. Reflectivity data at low q-vectors are those collected at low incident angles. The data were collected in a sample environment described in figure 4.2. In order that the applied field direction remains consistent between reflectivity data points, the magnetic pole pieces move with the sample holder. There are no means to move the pole pieces independently

	MgO	V	Pd Lower	Fe	Pd Upper	Al	Al_2O_3
Thickness (Å)	-	27.2	27.7	1.8	37.4	(25.9)	(26.2)
Roughness (Å)	5.0	5.3	1.5	0.1	3.2	(21.6)	(7.8)

Table 7.1: Structural parameters from the GenX fit shown in figure 7.9. The unreliable data at low q-vectors prevented the two uppermost layers from being meaningfully quantified. They are included (in brackets) only for completeness.

to the sample holder. Once the sample is mounted, it surface is aligned parallel to the beam direction through movement of the sample holder. This invariably prevents the pole pieces from being exactly parallel to the beam. The effect on the applied field is negligible. However, if the sample is not mounted sufficiently proud of the pole pieces, the misalignment of the pole pieces and incident beam direction can lead to the upstream pole piece clipping the incident beam. It is this effect which causes the dramatic reduction in measured intensity at low q-vectors. The data in this region are clearly unreliable, and so are omitted from the fitting procedure. This makes near surface features, such as oxidation or roughness, impossible to resolve. At larger q_z values, the incidence and reflected angles are sufficiently increased to avoid signal loss. The depth of the buried Fe layer is, fortunately, sufficient to avoid loss of clarity in the fitting.

The structural contribution shows clearly defined dips coinciding with peaks in the F.R. The low scattered intensity in comparison to a continuous film, leads to an increase in data noise which is particularly prevalent in the F.R. data. The data are, however, still of sufficient quality to allow meaningful analysis to be performed. The magnetic profile obtained in the fitting, shown in the inset to figure 7.9, describes a polarised region extending approximately 10 Å from the δ-layer. This is in accordance with both the expected polarisation extent, and observations from continuous film materials studied in section 6.2.

The fitting, which assumes no structural variation in the in-plane direction, simulates the data with reasonable accuracy. The fitting yielded a layer structure which is described in table 7.1. The fitting quality is sufficient to assume that the patterning process has had no detrimental effect on the structural integrity of the film.

7.3.1 Field Dependent Ordering

To make an accurate comparison between these XRMS and previous MOKE studies [135], both the location and nature of the magnetic phase transitions must be probed. These properties can both be gleaned from analysis of the field dependent magnetic ordering behaviour through observations of the remanent magnetisation, M_{rem}, and magnetic susceptibility, χ, respectively.

Hysteresis loops as a function of temperature were therefore collected, for both continuous and patterned samples, at the Pd L_3 edge, measured by recording the F.R. as a function of applied field while maintaining the fixed scattering vector required to maximize the saturation F.R. at 10 K. Data were collected in the specular condition and at the +1 satellite peak position for the continuous and patterned film respectively; maximising the magnetic sensitivity in each case. The hysteresis loops were recorded at discrete temperature intervals, with several minutes allowed for the temperature to stabilise after each step before the measurements were taken. The exact waiting time varied with the size of the temperature step. The applied field strength was incremented in discrete steps to ensure the statistical significance could be maintained for each datum.

The remanent magnetisation and magnetic susceptibility both critically depend on the magnetic behaviour in the near zero-field region of the loops. An accurate measure of both the applied field strength and F.R. is therefore imperative. The former can be achieved through accurate calibration between field and current in the electromagnet, the latter through fitting of the hysteresis loops to reduce the influence of data noise.

Field calibration was accomplished using a Hall probe, mounted equidistant from each pole piece, which recorded the applied field strength at the sample position as the magnet current was swept $\pm$ 4 A (sufficient to saturate both samples). The data from increasing and decreasing field values were separately fitted to 4th order polynomials, allowing current to be accurately converted to field values to approximately $\pm$ 40 mT. This has the additional advantage of naturally removing the influence of the small coercive field present in the electromagnet. However, for continuous film studies presented, a sample location within the homogeneous field, directly between the electromagnet pole pieces, was inaccessible due to the scattering geometry. The sample was instead located just proud of the uppermost surface of the pole pieces where the field strength is unavoidably inhomogeneous. As such, a true zero-field value across the continuous film did not exist. A "zero-field" point was instead defined by removing a coercive field from those hysteresis loops closest to T_{C}. The point where the maximum coercivity was removed which did not lead

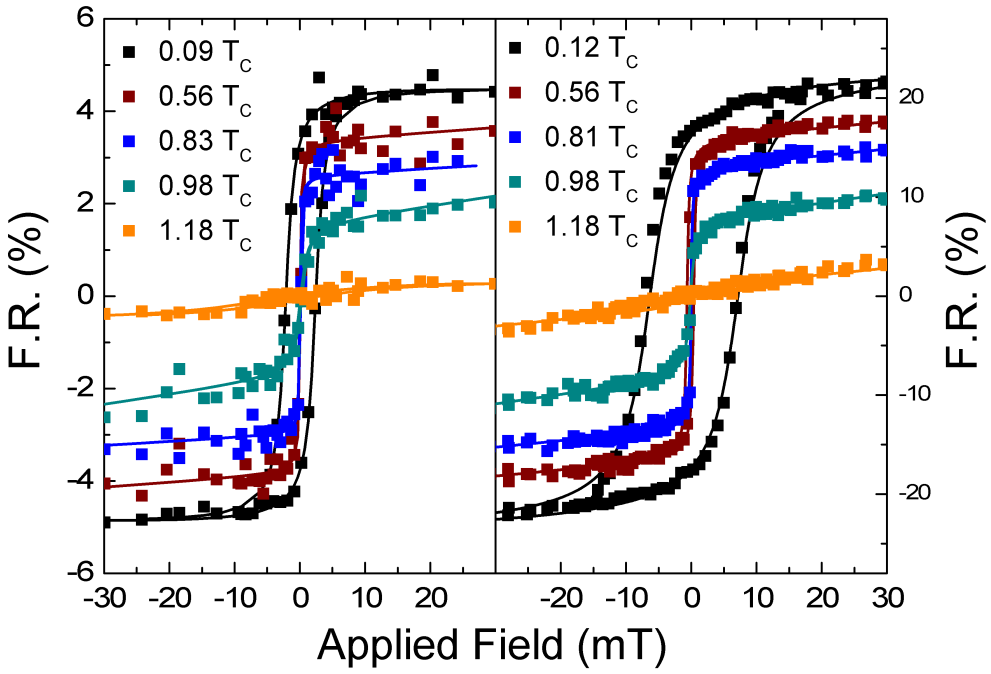

Figure 7.10: Comparison of loops from dots (left) and continuous film (right). Data (points) are fitted to arctan functions (lines) to enable the magnetic ordering behaviour to be reliably extracted. Temperatures are given as a fraction of T_C, where T_C= 117 and 124 K for the patterned and continuous films respectively.

to unphysical results, i.e. negative coercivity, was defined as "zero-field". A modification to the pole piece geometry was made before collection of the data from the patterned material which allowed these data to be collected in an homogeneous field position with a zero-field point naturally defined through the field calibration curve.

Hysteresis loop fitting was then performed to individual pairs of arctan functions following the methodology outline in section 4.2.3. This fitting was performed simultaneously across data at all temperatures. This additional, computationally intensive complication, enables logical constraints on the fitting parameters to be imposed. A, H_C, η and B were constrained to be greater than or equal to zero, and both H_C and A were compelled to reduce with increasing temperature. This reduction in the size of parameter space through the interplay of fitting parameters of different loops prevents unphysical magnetic behaviour, reducing uncertainty in the outputted values significantly.

Example hysteresis loops, with arctan fits, from the patterned and continuous films are shown in left and right panels of figure 7.10 respectively. At $T/T_C < 0.5$,

the hysteresis loops for both the patterned array and the continuous film show clear ferromagnetic behavior. The larger H_c observed in the continuous film is a result of the increase in volume of magnetic material aligning to the field. The previously discussed work by Arnalds et al. [135] predicts a superferromagnetic (SFM) to superparamagnetic (SPM) phase transition at approximately 0.6 T_{C} for circular islands of this diameter, followed by a second transition from SPM to PM coinciding with the FM to PM transition, at T_{C}, of the continuous film. It is therefore necessary to define a new parameter for the ordering temperature of the dots ($T_{\mathrm{C}}(D)$), which is distinct from that of the continuous film (T_{C}).

As the temperature is increased from base in the patterned array, a rapid collapse of both H_c and, crucially, H_{sat}, occurs which produces a square loop with no remanent magnetisation. This loop shape, maintained throughout the $0.6 < T/T_{\mathrm{C}} < 0.9$ region, is indicative of the lateral constraint of the magnet regions by the finite island size the onset of which coincides with the expected SFM to SPM transition temperature. Within the same temperature range, the continuous film also shows a collapse of H_c accompanied by a reduction in H_{sat} to ≈ 8 mT with a more rounded loop shape preserved throughout. Above $T/T_{\mathrm{C}} \approx 0.9$, the patterned array shows an increase in H_{sat} and broadening of the loop shape producing a hysteresis loop which shows identical behavior to the continuous film at all subsequent temperatures. This conforms with the second expected phase transition from SPM to PM. A more detailed comparison can be made by examining the field dependent magnetic ordering. This allows the subtle changes in the loop shapes to be more confidently resolved and was achieved by extracting the heights of the fitted hysteresis loops, at discrete field values, for both the patterned and continuous films. The resulting data are shown in figures 7.11 and 7.12.

In the continuous film, an increase in the strength of the applied field leads to an increase in T_{C}, and an increase in the observed moment at all temperatures. The large tails in the magnetisation above T_{C}, visible for fields above 0.5 mT, highlight a strong paramagnetic response in the critical region as expected. The magnetic response observed in the presence of an applied magnetic field of $\approx 2\ mT$ displays magnetic ordering behaviour consistent with that expected for a 2D-XY system. The deviation from a power-law response to the magnetisation, displayed for field values below ≈ 0.5 mT, is likely a remanent of the inhomogeneous applied field strength. It is probable that, at the determined "zero-field" value, areas of the film were experiencing magnetic reversal causing the observed magnetic response to be unduly reduced. Close to T_{C}, there is a broad region within which a strong response to applied field strength is observed. This behaviour is consistent with the magnetic

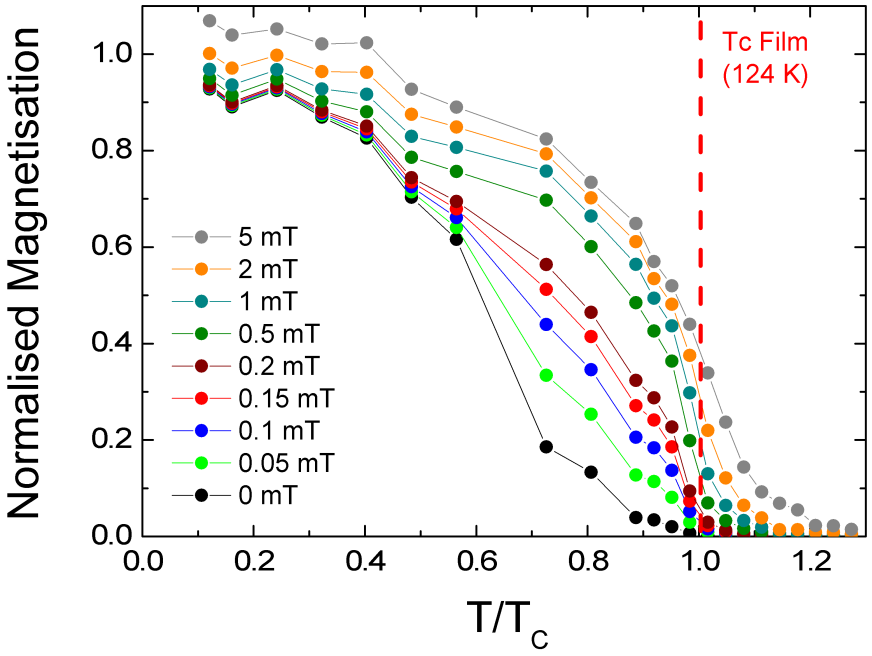

Figure 7.11: Field dependent magnetic ordering from a continuous Pd/Fe/Pd trilayer film, with an Fe δ-layer thickness of 0.7 ML. The data are normalised to H=2 mT at 15 K.

moments forming locally ordered macro-spins that re-orientate to reduce the total moment. The application of a small magnetic field allows the macro-spin regions, containing collinear moments, to grow and ultimately fully align across the sample.

The rapid collapse in H_c observed in the hysteresis loops of this patterned array is manifested in the ordering data as a collapse in the remanent magnetisation at approximately 75 K; well below the 117 K ordering temperature of the continuous film. This collapse represents the transition from a SFM into a SPM phase of locally ordered islands. In the $T_{\mathrm{C}}(D) < T < T_{\mathrm{C}}$ range, an applied field of 0.05 mT (a small fraction of the saturation magnetisation) is enough to partially align the globally disordered islands and create a nett magnetisation. The rapid increase in the magnetic response in this region is indicative of a large magnetic susceptibility. With the application of a 2 mT saturating field, the islands become fully aligned and show magnetic behaviour consistent with that expected of a continuous film. The finite size of the islands prevents the formation and expansion of locally ordered macro-spins as observed in the continuous film material. This serves to suppress the formation of magnetic order above T_{C}, reducing the tails in the magnetisation. The

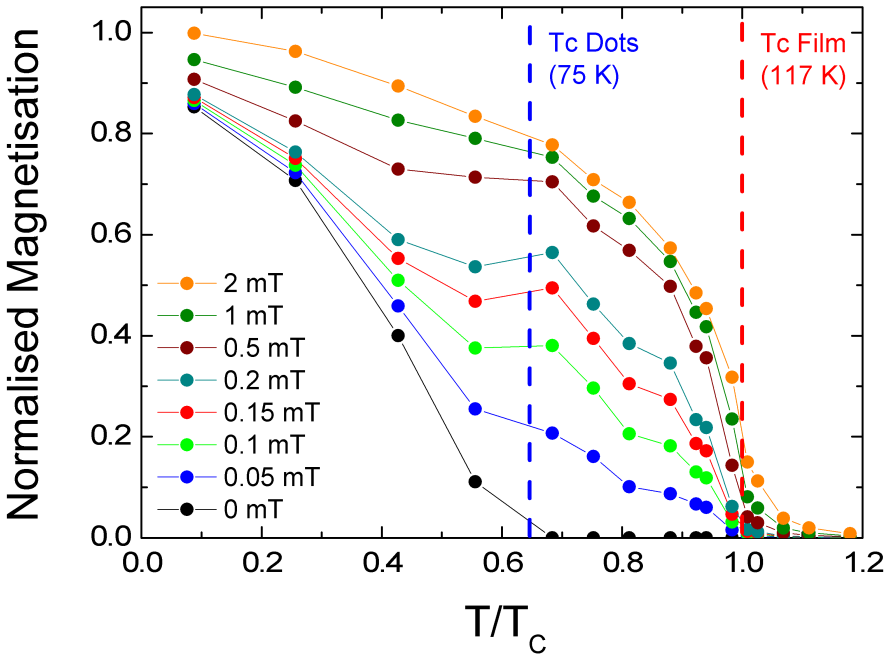

Figure 7.12: Field dependent magnetic ordering from 400 nm circular Pd/Fe/Pd dots on an 800 nm square grid with an Fe δ-layer thickness of 0.6 ML. The data are normalised to H=2.06 mT at 10 K

ordering temperature as the two phases correlate approximately with those found in the original MOKE study [135], though a precise measure of $T_C(D)$ is not possible with the point density available.

The susceptibility, $\chi \propto dM/dH$, was extracted analytically, at $H = 0$, from the results of the hysteresis loop fitting, for both the patterned and continuous films, using the relation:

$$\chi(H) = \frac{A}{\nu\left(1 + \left(\frac{(H \pm H_C)}{\nu}\right)^2\right)} + B, \tag{7.4}$$

where ν is the shape factor, A is the zero-field height of the unrounded loop and B is the gradient of the magnetisation approaching saturation. A comparison between the susceptibilities displayed by the patterned and continuous films is shown in figure 7.13.

The shape of the susceptibility peak observed from the continuous film peak, as discussed in section 6.2.1, is due to the narrowing of the polarised Pd region with

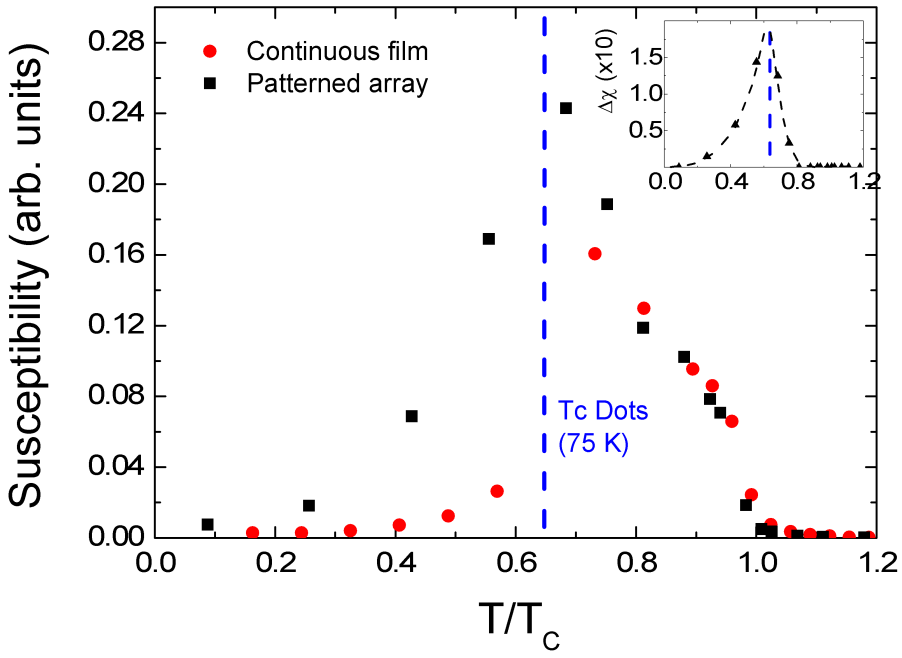

Figure 7.13: Zero-field magnetic susceptibility from FePd trilayer in both 0.6 ML 400 nm circular islands on an 800 nm square grid (blue squares) and 0.7 ML continuous film (red circles) geometries. T_C is defined as 117 K for the patterned film and 124 K for the continuous film. The inset shows the difference between the two data sets with an interpolated dotted line displaying the approximate trend.

increasing temperature. This leads to a gradual increase in the susceptibility as the outermost polarised layers become progressively magnetically disordered rather than the spike at T_C expected of a bulk material. The susceptibility of the patterned array displays a similar trend but with a significant increase at lower temperatures. Subtracting the continuous film behaviour from that of the patterned array allows the susceptibility within the array associated with the narrowing of the polarised Pd region to be removed, and only the contribution from the breaking of the inter-island coupling to be studied. The result, shown in the inset to figure 7.13, is a single peak coinciding with the SFM-SPM phase transition. The interpolated dashed line shows that the profile shape is consistent with a smoothly varying function.

It is assumed that this phase transition is driven by the thermal fluctuations overcoming the coupling between adjacent islands. The thermal energy required to overcome this magnetic potential and break the magnetic coupling between neighbouring islands then defines $T_C(D)$. The dipole interaction is likely to dominate

this coupling, which has an interaction energy, described earlier, which is defined as [24]:

$$E_{\text{dip}} = \frac{\mu_0}{4\pi r^3}\left[\mathbf{m}_1 \cdot \mathbf{m}_2 - \frac{3}{r^2}(\mathbf{m}_1 \cdot \mathbf{r})(\mathbf{m}_2 \cdot \mathbf{r})\right]. \tag{7.5}$$

For an array of identical ferromagnetically aligned circular islands, where each island is assumed to behave as a single moment acting at its centre, this equation simplifies to

$$E_{\text{dip}} \propto \frac{m^2}{r^3} \propto \frac{D^4}{D^3}, \tag{7.6}$$

as $\mathbf{m} \cdot \mathbf{r} = 0$ and all islands are assumed to have a total moment, m, which is dependent on the island diameter, D.

This dependence on D is not observed in the MOKE data [135]. Furthermore, the observed identical behaviour of $T_{\text{C}}(D)$, as a fraction of T_{C}, in islands with different ordering temperatures (i.e. different island moments) is not supported.

An alternative theory is therefore that the islands are sufficiently disconnected to not feel the influence of their neighbours. Within such a regime, the coercive field represent the energy required to rotate the magnetic orientation of an individual island. As the temperature increases, thermal excitations make this reorientation less energetically challenging, and so the coercive field of the array reduces. At a critical temperature, corresponding to $(T_{\text{C}}(D))$, the coercive field drops to zero and the remanent moment is lost. This description also explains the identical behaviour of $T_{\text{C}}(D)$ in islands with different T_{C}s: the reduction in the coercive field due to thermal excitations within the islands is proportional to the ordering temperature of the island material.

A logical extension to this work is then to increase the array pitch while maintaining the island size. If no change in $T_{\text{C}}(D)$ is observed, then the lack of interaction between islands can be verified. Conversely, if the array pitch was reduced, while the island size remained fixed, the separation at which $T_{\text{C}}(D)$ begins to increase will describe the maximum range of inter-island magnetic interactions. Though simple in principle, in practice collecting these data would take many months due to the requisite scheduled experimental time for both sample preparation and data collection.

The current data do, however, highlight the potential of patterned media for the investigation of complex magnetic interactions, and the suitability of resonant scattering to perform such investigations. It also highlights the difficulty in unambiguously determining the origin of observed behaviour. Even in a system with no

magnetic interactions, the ordering data present a non-trivial interpretation. The addition of magnetic interactions, possibly through various mechanisms operating on different length scales, will only increase the complexity of the features in the data. The unique investigative environments allowed through the use of patterned media make understanding such complexity in magnetic ordering data a key goal of future work. Further theoretical and experimental work is ongoing.

7.4 Conclusions

The aim of this chapter was to investigate magnetic interactions within patterned arrays of circular islands in two distinct configurations. First, closely spaced FePd alloy islands were examined to investigate the formation of magnetic vortex states. Second, a superferromagnetic to superparamagnetic phase transition was investigated in an arrangement of more widely spaced FePd trilayer islands. In both cases, the use of XRMS allowed analysis of the global magnetic response, averaged over the coherent beam footprint, to investigate the arrangement of magnetic moments within the array.

Analysis of rocking curves from the alloy islands attempted to resolve which of two possible magnetic vortex states had formed: vortices within each individual element, or "super-vortices" composed of interconnected chains of islands which form closed magnetic loops on a substantially larger scale. The data tentatively suggested that super-vortices had formed, extending over approximately 10×10 islands, growing with applied field strength. Substantial uncertainties exist in the data, making strong conclusions difficult to draw. However, the results highlight the potential of exploiting the global response of XRMS to probe the local magnetic structure within patterned materials.

Analysis of hysteresis loops collected from the trilayer array attempted to decipher the nature of an apparent superferromagnetic to superparamagnetic phase transition. The results appeared to showed a clear separation between the these two phases, and the additional, higher temperature paramagnetic phase associated with the loss of the island moments. However, more detailed analysis of the dipole interaction energy lead to the conclusion that individual islands are not interacting with their neighbours. Instead, the finite coercive field at low temperatures is lost as the temperature increases. The isolated ferromagnetic islands can rotate freely to align with an external field when the coercivity approaches zero, but are frozen to their initial alignment direction when the coercivity remains finite.

Both of these studies highlight the difficulty in unambiguously conducting

studies on patterned arrays. Though promising, both studies would benefit from further insight. The studies of magnetic vortex states would benefit significantly from better counting statistics. Without reducing the angular resolution, which is key to this work, better statistics would likely require significant increases to already considerable counting times. It may be possible that alternative geometries, such as a hexagonal array of circular islands, may be more conducive to the formation of regular super-vortices. Any increase in the magnetic correlation of the vortex arrangement within the array would provide a more prominent measurable signal. If the internal vortex state is present, a difference in array geometry would not be expected to have any effect as long as the separation between islands is maintained.

The study of magnetic interactions through the use of patterned materials has almost limitless scope for additional experimental studies though changing the arrangement and separation of islands, along with their size, shape and composition. The range of interactions between islands could be investigated by varying the array pitch, with all other parameters constant. As the islands begin to interact, and the energy required to break the inter-island coupling exceeds the minimum energy required to rotate the moments within the islands, an increase in the superferromagnetic to superparamagnetic phase transition temperature would be expected. If this behaviour was successfully observed, the dimensionality of the phase transition could then be examined for conformity to a typical universality class to potentially elucidate the nature of the interaction mechanisms present.

Chapter 8

Conclusions

The aim of this work was to investigate the coupling mechanisms present between adjacent magnetic lattices. Knowledge of these interactions is fundamental to the implementation of novel magnetic devices.

The work was split into two general categories, with distinct goals. The first was to map the induced moment profile across an interface. In the FeZr/CoZr system, the temperature and field dependence of the induced profile was mapped, and in the FePd systems, the element specific profiles were resolved. These profiles were successfully mapped with unprecedented resolution, through simultaneous fitting of resonant x-ray and polarised neutron reflectivity data using the GenX code. The shape and extent of the profiles was found to be invariant of the magnitude of the inducing moment. The magnitude of the induced moment profile was instead found to be critically determined by the roughness of the material interface; a product of the variation in surface area. Furthermore, the extent of the moment remained approximately constant as a function of both temperature and applied field, changing only in magnitude. Experimental limitations prevented the detailed investigation of the profile shape at the interface, which was particularly important in the Fe edge studies of the FePd systems. Variations in the profile shape on the smallest scale can only be resolved with access to reflectivity data at higher q values. In the Fe edge profiles of the FePd trilayer, the enhancement or suppression of the interface moments seen in the literature could not be resolved with the data available. The range of the induced moment in the FeZr was not sufficient to allow out-of-plane excitations in the FeZr/CoZr multilayer. It was proposed that as the FeZr lost its intrinsic moment, a transition into a 2d phase occurred which caused the total loss of magnetisation within the lattice. A further study to compare the multilayer behaviour to that of a trilayer film is needed to confirm this hypothesis.

The investigation of the interaction of the moments was further investigated in the second general investigation category: magnetic ordering. The dimensionalities of the two magnetic sub-lattices were resolved using resonant x-ray scattering. Atomically adjacent lattices, i.e. those across a material interface, were found not to be directly coupled. Instead, an indirect coupling mechanism was present which enabled the moments to interact through the magnetic susceptibility. In this way, the dimensionality of adjacent lattices remains distinct. As the interaction at an interface is only governed by the strength of the atomically adjacent moments, it is possible that this is a material independent phenomenon. A lack of Co edge data prevented a comparison being made in the FeZr/CoZr systems. This coupling mechanism has not previously been observed in the literature and, if proven to be a material independent phenomenon, could have significant impact on the interpretation of ordering data in both past and future low dimensional studies.

The magnetic ordering was additionally studied in patterned FePd films. This allowed the longer-range inter-island magnetic interactions to be investigated. These interactions were unexpectedly found to have little effect on the reorientation of the magnetic alignment. Instead, below a critical temperature, the energy required to reorientate the moments within each island dictates their coercive field. At a temperature sufficient to overcome this energy, though the islands remain magnetically ordered, they freely align to a residual applied field, and thus show no remanent moment. The strength of the magnetic interaction between the islands in this latter phase is not sufficient to affect their magnetic orientation. The range at which the interactions begin to affect the orientation of moments could be investigated by studying the magnetic ordering of the patterned array as a function of array pitch.

Though the results of these studies showed significant insight into the nature of magnetic interactions, one aspect succinctly highlights our poor understanding of these complex mechanisms: the Fe moment, in the thinnest Fe δ-layers studied, was seen to vanish. An unambiguous determination of the origin of this suppression remains elusive, with both an induced modification of the electronic structure and the percolation limit of long-range interaction providing plausible, if incomplete, explanations. To further our understanding of this phenomenon, additional data are required. Specifically, an Fe edge study of a dilute FePd alloy.

All of the work presented in this thesis provides insight into the equilibrium behaviour of the magnetic lattices. However, spintronic devices, rely on the the conduction of a spin-current across magnetic interfaces. This nett flow of electrons will fundamentally alter the diffusion of the electrons across the interface. As the

diffusion profile dictates the induced moment profile, this too will be fundamentally altered. In even this simple case, it is clear that electrical control of the fundamental magnetic properties should be possible. Though spin-injection, and subsequent control of magnetic orientation have already been achieved [141], the subtler effects of current flow on interface moments remains unexplored. This avenue of research could, therefore, not only provide a means to test the suitability of materials for producing spintronic components, but also provide a unique set of environments within which fundamental magnetic interactions can be studied. These studies would add another layer of complexity to the observed magnetic behaviour of low dimensional systems. The first step to make in this extension to the presented work would be to collect resonant x-ray reflectivity data as an out-of-plane current flow across a material interface was tightly controlled. As reflectivity data must, by their nature, be collected in reflection from a layered sample surface, the inclusion of electrodes to allow out-of-plane current flow would be a technological hurdle which would first need to be overcome.

Clearly, systems with reduced dimensionality will continue to provide challenging research possibilities through which novel future technologies can be developed and new insights into the complex nature of magnetic interactions can be gleaned.

Bibliography

[1] T. Nakayama, D.-H. Huang, and M. Aono, Microelectronic Engineering **32**, 191 (1996).

[2] J. Guzmán, N. Álvarez, H. Salva, M. V. Mansilla, J. Gómez, and A. Butera, Journal of Magnetism and Magnetic Materials **347**, 61 (2013).

[3] M. Salluzzo, S. Gariglio, D. Stornaiuolo, V. Sessi, S. Rusponi, C. Piamonteze, G. M. De Luca, M. Minola, D. Marré, A. Gadaleta, et al., Phys. Rev. Lett. **111**, 087204 (2013).

[4] A. J. Grutter, H. Yang, B. J. Kirby, M. R. Fitzsimmons, J. A. Aguiar, N. D. Browning, C. A. Jenkins, E. Arenholz, V. V. Mehta, U. S. Alaan, et al., Phys. Rev. Lett. **111**, 087202 (2013).

[5] N. Fujiwara, S. Tsutsumi, S. Iimura, S. Matsuishi, H. Hosono, Y. Yamakawa, and H. Kontani, Phys. Rev. Lett. **111**, 097002 (2013).

[6] R. Giri, S. Cronenberger, M. M. Glazov, K. V. Kavokin, A. Lemaitre, J. Bloch, M. Vladimirova, and D. Scalbert, Phys. Rev. Lett. **111**, 087603 (2013).

[7] V. S. Bhat, J. Sklenar, B. Farmer, J. Woods, J. T. Hastings, S. J. Lee, J. B. Ketterson, and L. E. De Long, Phys. Rev. Lett. **111**, 077201 (2013).

[8] M. H. Kryder, Thin Solid Films **216**, 174 (1992), papers presented at the International Workshop on Science and Technology of Thin Films for the 21st Century, Evanston,IL, USA, July 28-August 2, 1991.

[9] S. X. Wang and A. M. Taratorin, in *Magnetic Information Storage Technology* (AcademicPress, San Diego, 1999), pp. 81 – 122.

[10] J.-S. Noh, H. Kim, D. W. Chun, W. Y. Jeong, and W. Lee, Current Applied Physics **11**, S33 (2011), international Conference on Electronic Materials and Nanotechnology for Green Environment.

[11] A. Kikitsu, Journal of Magnetism and Magnetic Materials **321**, 526 (2009), current Perspectives: Perpendicular Recording.

[12] M. Tanaka, Journal of Crystal Growth **278**, 25 (2005), 13th International Conference on Molecular Beam Epitaxy.

[13] S. E. Thompson and S. Parthasarathy, Materials Today **9**, 20 (2006).

[14] G. E. Moore, Electronics **38** (1965).

[15] M. Fuechsle, J. Miwa, S. Mahapatra, H. Ryu, S. Lee, O. Warschkow, L. Hollenberg, G. Klimeck, and M. Simmons, Nature Nanotechnology **7** (2012).

[16] T. Kimura, K. Kuroki, and H. Aoki, Phys. Rev. B **53**, 9572 (1996).

[17] P. Chureemart, R. Cuadrado, I. D'Amico, and R. W. Chantrell, Phys. Rev. B **87**, 195310 (2013).

[18] A. Euverte, F. Hébert, S. Chiesa, R. T. Scalettar, and G. G. Batrouni, Phys. Rev. Lett. **108**, 246401 (2012).

[19] T. Ueno, M. Sawada, K. Furumoto, T. Tagashira, S. Tohoda, A. Kimura, S. Haraguchi, M. Tsujikawa, T. Oda, H. Namatame, et al., Phys. Rev. B **85**, 224406 (2012).

[20] J. Tersoff and L. M. Falicov, Phys. Rev. B **25**, 2959 (1982).

[21] D. Moore, O. Ozturk, F. Schumann, S. Morton, and G. Waddill, Surface Science **449**, 31 (2000).

[22] Y. C. Arango, E. Vavilova, M. Abdel-Hafiez, O. Janson, A. A. Tsirlin, H. Rosner, S.-L. Drechsler, M. Weil, G. Nénert, R. Klingeler, et al., Phys. Rev. B **84**, 134430 (2011).

[23] J. Stohr and H. C. Siegmann, *Magnetism: From Fundamentals to Nanoscale Dynamics*, vol. 152 of *Springer Series in Solid-State Physics* (Berlin: Springer, 2006).

[24] S. Blundell, *Magnetism in Condensed Matter (Oxford Master Series in Physics)* (Oxford University Press, USA, 2001), 1st ed.

[25] M. G. Mayer, Phys. Rev. **60**, 184 (1941).

[26] C. Zener, Phys. Rev. **81**, 440 (1951).

[27] P. Mohn, *Magnetism in the Solid State: An Introduction*, Springer Series in Solid-State Sciences (Springer, 2006).

[28] E. Purcell, *Electricity and Magnetism*, no. v. 2 in Berkeley Physics Course, Vol. 2 (McGraw Hill Book Company, 1985).

[29] R. Tilley, *Understanding Solids: The Science of Materials* (Wiley, 2013).

[30] M. F. Collins, *Magnetic critical scattering* (Oxford Univ. Press, New York, NY, 1989).

[31] W. Nolting and A. Ramakanth, *Quantum Theory of Magnetism* (Springer Berlin Heidelberg, 2009).

[32] E. C. Stoner, Proceedings of the Royal Society of London. Series A. Mathematical and Physical Sciences **165**, 372 (1938).

[33] A. P. Cracknell, J. Lorenc, and J. A. Przystawa, Journal of Physics C: Solid State Physics **9**, 1731 (1976).

[34] A. Patashinskii, V. Pokrovskii, and P. Shepherd, *Fluctuation theory of phase transitions*, International series in natural philosophy (Pergamon Press, 1979).

[35] D. S. Ritchie and M. E. Fisher, Phys. Rev. B **7**, 480 (1973).

[36] M. E. Fisher and M. N. Barber, Phys. Rev. Lett. **28**, 1516 (1972).

[37] E. Fermi, *Thermodynamics*, Dover books in physics and mathematical physics (Dover Publications, 1956).

[38] L. Onsager, Phys. Rev. **65**, 117 (1944).

[39] F. Bloch, Phys. Rev. **70**, 460 (1946).

[40] N. D. Mermin and H. Wagner, Phys. Rev. Lett. **17**, 1133 (1966).

[41] J. M. Kosterlitz and D. J. Thouless, Journal of Physics C: Solid State Physics **6**, 1181 (1973).

[42] B. Widom, The Journal of Chemical Physics **41**, 1633 (1964).

[43] C. L. Fu, A. J. Freeman, and T. Oguchi, Phys. Rev. Lett. **54**, 2700 (1985).

[44] I. Soroka, R. Bručas, V. Stanciu, P. Nordblad, and B. Hjörvarsson, Journal of Magnetism and Magnetic Materials **277**, 228 (2004).

[45] M. Björck, M. Pärnaste, M. Marcellini, G. Andersson, and B. Hjörvarsson, Journal of Magnetism and Magnetic Materials **313**, 230 (2007).

[46] A. Taroni and B. Hjörvarsson, The European Physical Journal B **77**, 367 (2010).

[47] R. Mortimer, *Physical Chemistry* (Elsevier Science, 2008).

[48] M. Zuckermann, Solid State Communications **12**, 745 (1973).

[49] D. A. van Leeuwen, J. van Ruitenbeek, G. Schmid, and L. de Jongh, Physica B: Condensed Matter **194-196, Part 1**, 263 (1994).

[50] O. Rader, E. Vescovo, J. Redinger, S. Blugel, C. Carbone, W. Eberhardt, and W. Gudat, Phys. Rev. Lett. **72**, 2247 (1994).

[51] S. V. Streltsov, Phys. Rev. B **88**, 024429 (2013).

[52] T. Herrmannsdörfer, S. Rehmann, W. Wendler, and F. Pobell, J. Low Temp. Phys. **104**, 49 (1996).

[53] M. A. Ruderman and C. Kittel, Phys. Rev. **96**, 99 (1954).

[54] T. Kasuya, Progress of Theoretical Physics **16**, 45 (1956).

[55] K. Yosida, Phys. Rev. **106**, 893 (1957).

[56] J. Kerr, Philosophical Magazine Series 5 **3**, 321 (1877).

[57] E. Hecht, *Optics (4th Edition)* (Addison Wesley, 2001), 4th ed.

[58] P. Langevin, J. Phys. Theor. Appl. **4**, 678 (1905).

[59] S. Schwarzl and H. Hoffmann, Physica B+C **86-88, Part 3**, 1406 (1977).

[60] A. Aspelmeier, F. Gerhardter, and K. Baberschke, Journal of Magnetism and Magnetic Materials **132**, 22 (1994).

[61] G. Bochi, H. J. Hug, D. I. Paul, B. Stiefel, A. Moser, I. Parashikov, H.-J. Güntherodt, and R. C. O'Handley, Phys. Rev. Lett. **75**, 1839 (1995).

[62] J. William Fuller Brown, Journal of Applied Physics **39**, 993 (1968).

[63] S. Bedanta and W. Kleemann, Journal of Physics D: Applied Physics **42**, 013001 (2009).

[64] S. E. Korshunov, Phys. Rev. B **85**, 134526 (2012).

[65] K. K. Kohli, A. L. Balk, J. Li, S. Zhang, I. Gilbert, P. E. Lammert, V. H. Crespi, P. Schiffer, and N. Samarth, Phys. Rev. B **84**, 180412 (2011).

[66] U. B. Arnalds, E. T. Papaioannou, T. P. A. Hase, H. Raanaei, G. Andersson, T. R. Charlton, S. Langridge, and B. Hjörvarsson, Phys. Rev. B **82**, 144434 (2010).

[67] A. Westphalen, A. Schumann, A. Remhof, H. Zabel, M. Karolak, B. Baxevanis, E. Y. Vedmedenko, T. Last, U. Kunze, and T. Eimüller, Phys. Rev. B **77**, 174407 (2008).

[68] G. Knoll, *Radiation Detection and Measurement* (John Wiley & Sons, 2010).

[69] H. Davies, Proceedings of the IEE - Part III: Radio and Communication Engineering **101**, 118 (1954).

[70] H. W. Edwards, Phys. Rev. **30**, 91 (1927).

[71] D. P. Woodruff, D. L. Seymour, C. F. McConville, C. E. Riley, M. D. Crapper, N. P. Prince, and R. G. Jones, Phys. Rev. Lett. **58**, 1460 (1987).

[72] U. B. Arnalds, T. P. A. Hase, E. T. Papaioannou, H. Raanaei, R. Abrudan, T. R. Charlton, S. Langridge, and B. Hjörvarsson, Phys. Rev. B **86**, 064426 (2012).

[73] W. H. Bragg and W. L. Bragg, Proceedings of the Royal Society of London. Series A **88**, 428 (1913).

[74] B. Henke, E. Gullikson, and J. Davis, Atomic Data and Nuclear Data Tables **54**, 181 (1993).

[75] G. Schütz, W. Wagner, W. Wilhelm, P. Kienle, R. Zeller, R. Frahm, and G. Materlik, Phys. Rev. Lett. **58**, 737 (1987).

[76] B. T. Thole, P. Carra, F. Sette, and G. van der Laan, Phys. Rev. Lett. **68**, 1943 (1992).

[77] P. Carra, B. T. Thole, M. Altarelli, and X. Wang, Phys. Rev. Lett. **70**, 694 (1993).

[78] J. Stöhr and H. König, Phys. Rev. Lett. **75**, 3748 (1995).

[79] C. Kao, J. B. Hastings, E. D. Johnson, D. P. Siddons, G. C. Smith, and G. A. Prinz, Phys. Rev. Lett. **65**, 373 (1990).

[80] J. R. Dunning, G. B. Pegram, G. A. Fink, and D. P. Mitchell, Phys. Rev. **48**, 265 (1935).

[81] J. Penfold and R. K. Thomas, J. Phys.: Condens. Matter **2**, 1369 (1990).

[82] V. F. Sears, Neutron News **3**, 26 (1992).

[83] O. Halpern and M. H. Johnson, Phys. Rev. **51**, 992 (1937).

[84] O. Halpern and M. H. Johnson, Phys. Rev. **52**, 52 (1937).

[85] O. Halpern and M. H. Johnson, Phys. Rev. **55**, 898 (1939).

[86] T. Chatterji, *Neutron Scattering from Magnetic Materials* (Elsevier Science, Amsterdam, 2006).

[87] P. A. M. Dirac, Proceedings of the Royal Society of London. Series A **114**, 243 (1927).

[88] J. Ankner and G. Felcher, Journal of Magnetism and Magnetic Materials **200**, 741 (1999).

[89] A. Hofmann, *The Physics of Synchrotron Radiation* (Cambridge University Press, 2004).

[90] L. Bouchenoire, S. D. Brown, P. Thompson, J. A. Duffy, J. W. Taylor, and M. J. Cooper, Journal of Synchrotron Radiation **10**, 172 (2003).

[91] C. Sánchez-Hanke, C.-C. Kao, and S. Hulbert, Nuclear Instruments and Methods in Physics Research Section A: Accelerators, Spectrometers, Detectors and Associated Equipment **608**, 351 (2009).

[92] G. Bauer, Nuclear Instruments and Methods in Physics Research Section A: Accelerators, Spectrometers, Detectors and Associated Equipment **463**, 505 (2001), accelerator driven systems.

[93] V. Nunez, A. Boothroyd, J. Reynolds, J. Penfold, S. Langridge, D. Bucknall, P. Böni, D. Clemens, and M. Kumar, Physica B: Condensed Matter **241-243**, 148 (1997), proceedings of the International Conference on Neutron Scattering.

[94] M. Björck and G. Andersson, Journal of Applied Crystallography **40**, 1174 (2007).

[95] L. G. Parratt, Phys. Rev. **95**, 359 (1954).

[96] J. Tonnerre, E. Jal, E. Bontempi, N. Jaouen, M. Elzo, S. Grenier, H. Meyerheim, and M. Przybylski, The European Physical Journal - Special Topics **208**, 177 (2012).

[97] M. Björck, G. Andersson, B. Lindgren, R. Wäppling, V. Stanciu, and P. Nordblad, Journal of Magnetism and Magnetic Materials **284**, 273 (2004).

[98] W. Dürr, M. Taborelli, O. Paul, R. Germar, W. Gudat, D. Pescia, and M. Landolt, Phys. Rev. Lett. **62**, 206 (1989).

[99] S. C. Hong, T. Rho, and J. I. Lee, Journal of Magnetism and Magnetic Materials **140-144, Part 1**, 697 (1995), international Conference on Magnetism.

[100] G. Panaccione, F. Sirotti, and G. Rossi, Journal of Magnetism and Magnetic Materials **198-199**, 677 (1999).

[101] G. Wiatrowski, D. Baldomir, K. Warda, M. Pereiro, L. Wojtczak, and J. Arias, Journal of Magnetism and Magnetic Materials **277**, 285 (2004).

[102] F. Huang, M. T. Kief, G. J. Mankey, and R. F. Willis, Phys. Rev. B **49**, 3962 (1994).

[103] S. Kaul, Curr. Sci. **88** (2005).

[104] D. H. Ryan, J. M. D. Coey, E. Batalla, Z. Altounian, and J. O. Ström-Olsen, Phys. Rev. B **35**, 8630 (1987).

[105] A. Tago, C. Nishimura, and K. Yanagisawa, IEEE Transactions on Magnetics **21**, 2032 (1985).

[106] M. Ahlberg, P. Korelis, G. Andersson, and B. Hjörvarsson, Phys. Rev. B **85**, 224425 (2012).

[107] M. Ahlberg, G. Andersson, and B. Hjörvarsson, Phys. Rev. B **83**, 224404 (2011).

[108] I. Soroka, J. Vegelius, P. Korelis, A. Fallberg, S. Butorin, and B. Hjörvarsson, Journal of Nuclear Materials **401**, 38 (2010).

[109] M. Pärnaste, M. Marcellini, E. Holmström, N. Bock, J. Fransson, O. Eriksson, and B. Hjörvarsson, J. Phys. Condens. Matter **19**, 246213 (2007).

[110] Y. Li and K. Baberschke, Phys. Rev. Lett. **68**, 1208 (1992).

[111] P. V. Jasen, E. A. Gonzalez, N. J. Castellani, and A. Juan, Phys. Rev. B **71**, 235422 (2005).

[112] R. V. Chepulskii, S. V. Barabash, and A. Zunger, Phys. Rev. B **85**, 144201 (2012).

[113] A. Boufelfel, R. M. Emrick, and C. M. Falco, Phys. Rev. B **43**, 13152 (1991).

[114] L. Szunyogh, J. Zabloudil, A. Vernes, P. Weinberger, B. Újfalussy, and C. Sommers, Phys. Rev. B **63**, 184408 (2001).

[115] M. Li, X. D. Ma, C. B. Peng, J. G. Zhao, L. M. Mei, Y. S. Gu, W. P. Chai, Z. H. Mai, B. G. Shen, Y. H. Liu, et al., Phys. Rev. B **50**, 10323 (1994).

[116] A. Oswald, R. Zeller, and P. H. Dederichs, Phys. Rev. Lett. **56**, 1419 (1986).

[117] L. Cheng, Z. Altounian, D. H. Ryan, J. O. Ström-Olsen, M. Sutton, and Z. Tun, Phys. Rev. B **69**, 144403 (2004).

[118] Z. Celinski, B. Heinrich, J. F. Cochran, W. B. Muir, A. S. Arrott, and J. Kirschner, Phys. Rev. Lett. **65**, 1156 (1990).

[119] M. Pärnaste, M. Marcellini, E. Holmström, N. Bock, J. Fransson, O. Eriksson, and B. Hjörvarsson, J. Phys-Condens. Matter **19** (2007).

[120] F. Huang, M. T. Kief, G. J. Mankey, and R. F. Willis, Phys. Rev. B **49**, 3962 (1994).

[121] S. Singh, M. R. Fitzsimmons, T. Lookman, J. D. Thompson, H. Jeen, A. Biswas, M. A. Roldan, and M. Varela, Phys. Rev. Lett. **108**, 077207 (2012).

[122] G. Nieuwenhuys, Advances in Physics **24**, 515 (1975).

[123] G. Bergmann, Phys. Rev. Lett. **41**, 264 (1978).

[124] R. Medina and R. E. Parra, Journal of Applied Physics **53**, 2201 (1982).

[125] M. F. Sykes and J. W. Essam, Journal of Mathematical Physics **5**, 1117 (1964).

[126] C. D. Lorenz, R. May, and R. M. Ziff, Journal of Statistical Physics **98**, 961 (2000).

[127] S. Piramanayagam and K. Srinivasan, Journal of Magnetism and Magnetic Materials **321**, 485 (2009), current Perspectives: Perpendicular Recording.

[128] R. Singh, Journal of Magnetism and Magnetic Materials **346**, 58 (2013).

[129] M. El-Hilo, Journal of Magnetism and Magnetic Materials **322**, 1279 (2010), proceedings of the Joint European Magnetic Symposia.

[130] J. Mejia-Lopez, D. Altbir, P. Landeros, J. Escrig, A. H. Romero, I. V. Roshchin, C.-P. Li, M. R. Fitzsimmons, X. Batlle, and I. K. Schuller, Phys. Rev. B **81**, 184417 (2010).

[131] O. Kazakova, M. Hanson, A. Blixt, and B. Hjörvarsson, Journal of Magnetism and Magnetic Materials **258-259**, 348 (2003), second Moscow International Symposium on Magnetism.

[132] R. P. Cowburn, D. K. Koltsov, A. O. Adeyeye, and M. E. Welland, Applied Physics Letters **73**, 3947 (1998).

[133] R. P. Cowburn, A. O. Adeyeye, and M. E. Welland, Ne Journal of Physics **1** (1999).

[134] G. Carlotti, G. Gazzadi, G. Gubbiotti, M. Madami, S. Tacchi, and P. Vavassori, Thin Solid Films **515**, 739 (2006).

[135] U. Arnalds, M. Ahlberg, M. Brewer, V. Kapaklis, E. Papaioannou, M. Karimipour, P. Korelis, A. Stein, S. Olafsson, T. Hase, et al., Submitted (2014).

[136] R. Cowburn, Journal of Magnetism and Magnetic Materials **242-245, Part 1**, 505 (2002), proceedings of the Joint European Magnetic Symposia.

[137] R. Cowburn, D. Koltsov, A. Adeyeye, M. Welland, and D. Tricker, Physical Review Letters **83**, 1042 (1999).

[138] K. Pearson, Royal Society of London Philosophical Transactions Series A **216**, 429 (1916).

[139] R. Bracewell, *The Fourier Transform and Its Applications*, McGraw-Hill international editions (McGraw-Hill Education, 2000).

[140] C. Sánchez-Hanke, F. J. Castano, Y. Hao, S. L. Hulbert, C. Ross, H. I. Smith, and C.-C. Kao, IEEE Transactions on Magnetics **39**, 3450 (2003).

[141] A. Fert, A. Barthélémy, J. Youssef, J.-P. Contour, V. Cros, J. D. Teresa, A. Hamzic, J. George, G. Faini, J. Grollier, et al., Materials Science and Engineering: B **84**, 1 (2001).